Development of an Ionospheric Map for Africa

A thesis submitted in fulfilment of the
requirements for the degree of

DOCTOR OF PHILOSOPHY

of

RHODES UNIVERSITY

by

NICHOLAS SSESSANGA

January 2014

Abstract

This thesis presents research pertaining to the development of an African Ionospheric Map (AIM). An ionospheric map is a computer program that is able to display spatial and temporal representations of ionospheric parameters such as, electron density and critical plasma frequencies, for every geographical location on the map. The purpose of this development was to make the most optimum use of all available data sources, namely ionosondes, satellites and models, and to implement error minimisation techniques in order to obtain the best result at any given location on the African continent. The focus was placed on the accurate estimation of three upper atmosphere parameters which are important for radio communications: critical frequency of the F2 layer (foF2), Total Electron Content (TEC) and the maximum usable frequency over a distance of 3000 km (M3000F2). The results show that AIM provided a more accurate estimation of the three parameters than the internationally recognised and recommended ionosphere model (IRI-2012) when used on its own. Therefore, the AIM is a more accurate solution than single independent data sources for applications requiring ionospheric mapping over the African continent.

Contents

List of Figures

List of Tables

Publications from this thesis

One paper has been accepted for publication out of this study.

Nicholas Ssessanga, Lee-Anne McKinnell, John Bosco Habarulema (2014): Estimation of foF2 from GPS TEC over the South African region. Journal of Atmospheric and Solar-Terrestrial Physics 112, 20-30. This paper describes a pioneering statistical method (TEC2F2) of estimating the critical frequency (foF2) values from Global Positioning System (GPS) Vertical Total Electron Content (VTEC). The method was first developed over the South African region using the available ionosondes stations and GPS receiver stations. The results from this method were more accurate at estimating the foF2 parameter over the South African region than the mostly used International Reference Ionospheric (IRI-2012) model. The details of this method form most of chapter 5.

Acknowledgements

It is my wish to extend my sincere gratitude and high appreciation to my supervisors Dr. Lee-Anne McKinnell in her guidance towards the success of this study.

Thanks to the staff of SANSA for their hospitality, logistical, technical and work support during my study.

Special thanks go to SANSA for my PhD degree scholarship.

Thanks to my family for the continuous support since I joined the academic field especially my sister Halima Namakula, aunt Beat Mugenyi (RIP), aunt Macrine Namaganda, aunt Yvonne Nakalo Nsubuga and Uncle Gerald Ssonko.

Thanks to John Bosco Habarulema and other colleagues who assisted me in many ways to finish up this thesis. Your help is greatly appreciated.

Chapter 1

Introduction

This thesis presents research pertaining to the development of an African Ionospheric Map (AIM). An ionospheric map is essentially a computer program that produces spatial and temporal representations of ionospheric parameters like electron density, critical plasma frequencies, etc. for every geographical location on the map (Okoh et al., 2010). The purpose was to create a ionospheric representation of a desired location and time stamp by making use of all available resources. The design of the AIM is based on work by Okoh (2009) on the South African region.

1.1 Problem Statement

The African continent is the second largest land mass in the world. However, the continent is faced with a paucity of ionospheric data as compared to the rest of the world. This paucity has contributed to inaccuracies in space weather forecasting throughout the continent, leading to problems in the communication sector in particular for which a reasonably accurate ionospheric representation is essential. The AIM uses

the available ionospheric data sources, namely ionosondes, satellites and models, and error minimisation techniques to obtain the best result at any given location on the continent.

1.2 Requirements and Resources

The International Reference Ionosphere (IRI) model is a globally recognised model for predicting plasma parameters in the Earth's ionosphere (Bilitza et al., 2011). However, the IRI model does not perform well over the African sector due to the paucity of ionospheric data for the region during the early stages of development of the model. Different groups identified these inaccuracies over the South African region. For example, McKinnell and Poole (2004), and Okoh et al. (2010) developed ionospheric models to overcome the deficiencies of the IRI. These models, the South African Bottomside Model (SABIM) and South African Ionospheric Map (SAIM) were developed to improve the prediction of ionospheric parameter values over South Africa. Currently, these two models are used within Direction Finding (DF) systems, that are deployed by industry on behalf of the defence sector.

Since the current models are limited to the South African region, the motivation for development of the AIM was to design a more accurate tool that can be used by the communications and defence industries in DF for the whole of Africa. The map may also be used by aviation industries in their positioning and navigation systems, for correction of ionospheric effects.

1.3 Purpose of the Project

The purpose of this project was to develop a map for the whole of Africa showcasing the ionospheric parameters (to be described in chapter 2) most often used by communication industries.

The map purposes to:

- be user friendly, making sensible use of all available ionospheric resources for determining the best representation at any location,
- show the temporal and spatial variation of the parameters in real time as well as historically, and
- detail the expected ionospheric physics at any geographical location.

1.4 Overview of the Project

This section outlines the structure of the thesis.

Chapter 2 discusses the background theory pertaining to the Earth's ionosphere, and the different techniques used to measure the parameters that define it.

Chapter 3 discusses the improvements to the South African Ionospheric Map (SAIM) and validates the results.

Chapter 4 describes the initial attempt at developing the African Ionospheric Map (AIM).

Chapter 5 discusses a method (TEC2F2) of deriving foF2 values from the Global Positioning System (GPS) Vertical Total Electron Content (VTEC) values.

Chapter 6 discusses the use of GPS occultation data in AIM to enhance the program's performance.

Chapter 7 discusses AIM's operation and interface.

Chapter 8 validates the results produced by AIM.

Chapter 9 gives concluding remarks and suggests future work.

Chapter 2

Background Theory

2.1 Introduction

This chapter discusses the basic background theory pertaining to the Earth's ionosphere as applicable to the work presented in this thesis. The theory describes the mechanisms that lead to the creation of the ionosphere and its variability. The different ionospheric measurement techniques and models that are used as data sources in the AIM are the ground-based High Frequency (HF) radio sounders (ionosondes), satellites, the International Reference Ionospheric (IRI) model and the South African Bottomside Ionospheric Model (SABIM).

2.2 The Ionosphere

The ionosphere is that region of the upper atmosphere ranging from 50 to about 2000 km in altitude. This region is composed of ionised gas (plasma) which is created when the Ultra-Violet (UV) radiation, cosmic rays, solar wind particles and X-rays from the Sun strip electrons off the gas molecules in the upper atmosphere to become ions through the

process of ionisation. The created plasma maintains its state of dynamic equilibrium throughout the recombination process.

2.2.1 Ionisation and Recombination

Ionisation: On the day-side of the Earth, the sun emits a beam of energy which decreases in intensity with increasing distance towards the Earth. The reduction in intensity is due to photoionisation, as rays are incident on the neutral atmosphere that increases exponentially in density with decreasing altitude. The process of photoionisation is can be described as:

$$X + hv \longrightarrow X^+ + e^- \tag{2.1a}$$

$$XY + hv \rightarrow XY^+ + e^- \tag{2.1b}$$

where X and XY represent a neutral atom and molecule in the atmosphere, hv is the energy of the incident photon, $X^+$and XY^+ represent the produced ions and e^- is the free electron produced in the process.

Recombination is the rate at which ions and electrons combine to form a neutral molecule or atom. This process is predominant at night and it occurs when a free electron moves close enough to the ion to be captured. It also accelerates with decreasing altitude since the gas molecules and ions draw closer together.

There are two types of recombination as indicated in equations 2.2a and 2.2b. The *slow* recombination is a radiative process which involves an electron combining with an ion to form a neutral atom, while the $fast$ recombination is dissociative and involves the splitting of a positi-

vely charged molecule into two neutral atoms (Schunk and Nagy, 2009; Ratcliffe, 1972).

$$X^+ + e^- \rightarrow X + hv(slow) \tag{2.2a}$$

$$XY^+ + e^- \rightarrow X + Y(fast) \tag{2.2b}$$

2.2.2 Vertical Structure of the Ionosphere

A combination of ionisation, recombination and an exponential increase in density of the neutral atmosphere with decreasing altitude leads to the formation of the vertical profile of the ionosphere. The profile is divided into three regions; the plasmasphere, the topside ionosphere and the bottomside ionosphere, as illustrated in figure 2.1.

The plasmasphere is the extension of the ionosphere into the magnetosphere with a relatively dense and cool plasma, which is mainly composed of hydrogen ions (H^+) (Prölss, 2004). At a height of approximately 1500 km (known as the Upper Transition Height (UTH)) the composition of H^+ is approximately equal to that of oxygen ions (O^+).

The topside ionosphere is that region below the UTH that extends above the peak electron density point, and the bottomside ionosphere is the region below the peak electron density. The bottomside ionosphere is subdivided into three regions (D, E and F).

The F-region ranges from approximately 200 to 15000 km in altitude and during the day it splits into two layers, F2 and F1.

The F2 layer is the region from about 200 km up to the peak electron density (NmF2). This layer is the most dynamic and dense (almost $10^6 cm^{-3}$) in the ionosphere with predominant ions being O^+. The height

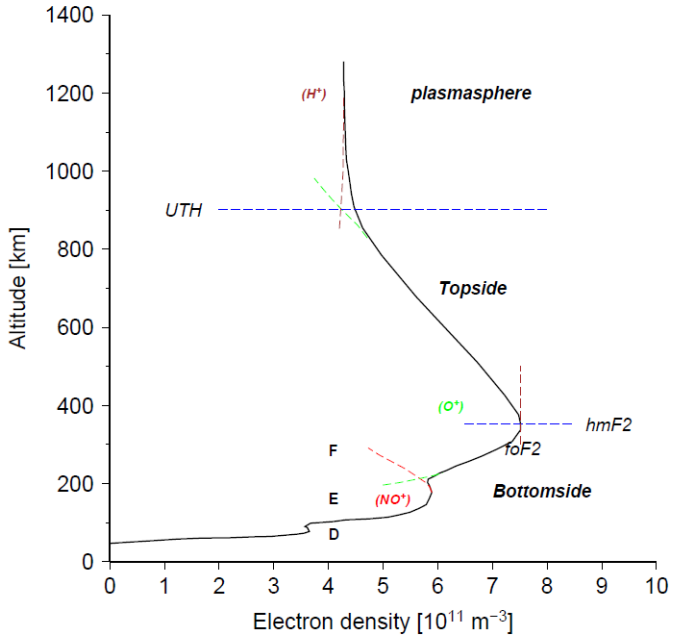

Figure 2.1: Typical vertical distribution of electron density in the ionosphere divided into three regions: plasmasphere, topside and bottomside (Sibanda, 2010).

of the peak density (hmF2) in the F2 layer depends on geophysical conditions and varies between 250 and 400 km. The variability and high electron concentration in the F2 layer determines the propagation of the decametric radio waves and is the main contributor to all errors of radio navigation systems (Pulinets and Boyarchuk, 2004).

The F1 layer results from the degree of ionisation and recombination falling off during the day. It ranges from about 130 to 200 km in altitude and the predominant ions are NO^+_2 and O^+_2 (Schunk and Nagy, 2009). The maximum electron density is labelled as NmF1 and occurs at a height hmF1 ($\approx$ 180 km). During the night the F1 layer decays considerably leaving the E-F valley which separates the E and F2 layers.

The E-region ranges from 90 to 130 km and has the second highest electron concentration ($10^5 cm^{-3}$) after the F-region. The primary ions

in this region are $NO^+{}_2$, $O^+{}_2$ and O^+. The maximum electron density in this layer is labelled as NmE and occurs at a height hmE. At night the E-region is weakly ionised, but it does not completely disappear (Hunsucker and Hargreaves, 2002). The weakly ionised E-layer is sometimes due to the sporadic E-layer. Sporadic E-layers are ionisation enhancements in the E region at altitudes between 90 and 120 km. The layers tend to occur sporadically and can be seen at all latitudes. At mid-latitudes sporadic E-layers are primarily a result of wind shears, but they can also be created by diurnal and semi-diurnal tides as well as by gravity waves (Schunk and Nagy, 2009).

The D-region covers altitudes 60 to 90 km and has the least amount of ionisation compared to the F and E regions. The main ionisation is due to Lyman series-alpha hydrogen radiation ionising Nitric Oxide (NO). The D-region attains a maximum electron concentration of about $10^3 \mathrm{c}m^{-3}$ and disappears at the night with recombination playing the greatest role (Kelley, 2009).

2.3 Variations of the Ionosphere

Since the Sun is the primary source of ionisation in the ionosphere, any changes in the amount of radiation or the relative geometry between the Sun and Earth cause diurnal, seasonal, solar cyclical and geographical (mainly latitudinal) variations in the ionosphere.

2.3.1 Diurnal Variation

Diurnal variation is a result of the Earth's 24-hour rotation on its own axis, creating night and day. During the night the F1-region disappears

and the lower regions, E and D, reduce considerably since photochemistry dominates at these altitudes. During the day their occurrence depends entirely on the zenith angle of the Sun, which is approximately 0° at noon and around 90° both at sunrise and sunset (McNamara, 1991).

On the other hand, the F2-region does not entirely show a strong solar zenith angle dependence. It is influenced mainly by plasma transport mechanisms with maximum ionisation occurring at local noon. The F2-region exists throughout the night, but with a reduced electron density (concentration) due to the recombination process.

2.3.2 Seasonal Variation

The seasonal variations of the ionosphere are related to the changes in the solar zenith angle. In winter the zenith angle at noon is greater than the corresponding angle in summer. As a result, the electron density concentration in the F1, E and D regions is greater in summer than in winter. In the F2-region at the mid-latitudes, the opposite occurs and the critical electron density is higher in winter than in summer. This phenomenon is known as the mid-latitude Seasonal Anomaly and occurs due to the seasonal changes in the neutral atmosphere (McNamara, 1991).

2.3.3 Solar Cycle Variation

The largest temporal scale of the ionosphere variability is connected to the solar cycle. The solar cycle is a period of 11 years and is monitored by observing the 11-year sunspot cycle. During an 11-year sunspot cycle

a time of solar maximum and a time of solar minimum is observed. During solar maximum the solar radiation is greater than during solar minimum. As a consequence, the ionospheric ionisation is greater during solar maximum than during solar minimum.

2.3.4 Latitudinal Variations

Latitudinal ionospheric variations are more pronounced in the low latitude regions. At geomagnetic latitudes of approximately $\pm$ 20° a high electron concentration occurs due to the Fountain Effect: an uplifting of the equatorial F2-layer due to the combined effect of the electric and magnetic fields on the electrons, causing them to drift upwards. As they rise, they encounter the horizontal lines of force of the Earth's magnetic field. The electrons travel along these field lines and re-enter the main body of the ionosphere where the field lines cut through the F-region (McNamara, 1991).

At the mid-latitudes the ionospheric variations are lower and the higher latitudes (between 60° and 70°) are characterised by short-term variations.

2.4 Ionospheric Measurement Techniques

The use of different ionospheric measurement techniques has led to a better understanding of the ionosphere in terms of its vertical, temporal and spatial variations. These techniques can be either ground- or space-based. This subsection examines the use of ground-based High Frequency (HF) radio sounders (ionosondes) and satellite (space-based) systems to measure the ionospheric parameters required by the AIM.

2.4.1 High Frequency (HF) Radio Sounding (ionosondes)

Ionospheric variability is commonly studied by using measurements from ground-based ionosondes. This technique is currently the most accurate available method for measuring ionospheric parameters.

Ionosonde operation is based on the fact that the ionospheric plasma is a dispersive medium of which the refractive index (μ) can be expressed in terms of the density of free electrons (N_e) and the sounding frequency (f), as shown in equation 2.3 (Reinisch, 2009). During operation the sounder transmits radio pulses, vertically scanning a large frequency band from approximately 1 MHz to 30 MHz in order to cover the ionisation structure from the E-region to the F-region (Reinisch, 1986).

$$\mu^2 = 1\text{-k}(N_e/f^2) \tag{2.3}$$

When the critical frequency of the radio waves (f_c) equals the plasma frequency (f_p), the waves are reflected. At this point $\mu \approx 0$, hence equation 2.3 becomes

$$f_p^2 = \text{k}(N_e), \;\; \text{k} = (e^2/4\pi\varepsilon_0 m) \approx 80.5, \tag{2.4}$$

where e is the charge of an electron, ε_o is the permittivity of free space and m is the mass of an electron (Davies, 1990).

At the receiver the time delay (τ), i.e. the time that it takes for the radio signal to be reflected back, is recorded.

Using equation 2.4 and τ, the peak electron density and altitude ($\frac{c\tau}{2}$, c is speed of light) of reflection of the different layers of the ionosphere can

Table 2.1: Ionospheric peak parameters in the F, E and D regions

Layer	Critical frequency	Peak altitude
F2	foF2	hmF2
F1	foF1	hmF1
E	foE	hmE
D	foD	hmD

be deduced. It is from these two parameters that the electron density profile is generated.

In the AIM only parameters that are important for radio communications are represented. Table 2.1 summarises some of those parameters for which measurements can be obtained by using ground-based radio sounding.

2.4.1.1 Maximum Usable Frequency (MUF) and M(3000)F2

MUF is another parameter of significant importance in radio communication for which values can be obtained by using ground-based radio sounding. MUF is defined as the maximum frequency a radio transmitter would require if the radiation angle (I) of the transmitted wave is changed from being vertical to nearer horizontal.

To a good approximation, the MUF is given by the formula (McNamara, 1991)

$$\mathrm{MUF} = \frac{\mathrm{f}_c}{\cos(I)} \tag{2.5}$$

If the transmitted radio waves cover a distance of 3000 km on the ground to reach the receiver, the MUF is defined as MUF(3000). If the propagation is done through the F2 layer, the MUF(3000) and foF2 are then related by a parameter defined as (Bradley and Dudeney, 1973)

$$\mathrm{M(3000)F2} = \frac{\mathrm{MUF(3000)}}{\mathrm{foF2}} \tag{2.6}$$

The M(3000)F2 parameter is of importance as it is used to derive hmF2, as illustrated in equation 2.7. $\triangle M(X)$ is a correction factor that accounts for the effects of the E-layer and can be expressed in terms of the critical frequencies foF2 and foE (Rishbeth et al., 2000).

$$\mathrm{hmF2} = \frac{1490}{(\mathrm{M(3000)F2} + \triangle M(X))} - 179, \;\; X = \frac{\mathrm{foF2}}{\mathrm{foE}} \tag{2.7}$$

2.4.2 Spaceborne Ionospheric Measurement (satellites)

The use of ground-based instruments such as ionosondes has always been limited to limited spatial coverage and to the bottomside ionosphere. The introduction of spaceborne instruments onboard satellites made possible column density measurement of the terrestrial ionosphere over a very wide geographic area. At present there are two Global Navigation Satellite Systems (GNSSs) in operation, the Global Positioning System (GPS) and the Global Orbiting Navigation Satellite System (GLONASS). Table 2.2 summarises the characteristics of both systems. This subsection emphases the GPS system, which is most widely used. It also describes how the observables are used to obtain the Total Electron Content (TEC) parameter (described later in subsection 2.4.3).

2.4.2.1 GPS Signals

The accuracy of the GPS system lies in the fact that all signal components are controlled precisely by atomic clocks. The atomic clocks

Table 2.2: Summary of characteristics of the Global Navigation Satellite Systems (GNSSs), GPS and GLONASS

Characteristic	GPS	GLONASS
Owner	United States Department of Defense (USDoD)	Russian Republic
Number of satellites	32	24
Distribution	6 orbital distributions	3 uniform orbital distributions
Orbital plane inclination relative to the equator	55°	64.8°
Orbital separation	60° right ascension	120° right ascension
Orbit Radii from centre of the Earth	26,560 km	25,510 km
Orbital period	one-half sidereal day	$\frac{8}{17}$ of a sidereal day
L-Band carrier frequencies	L_1 = 1575.42 MHz, L_2= 1227.6 MHz	L_1 = 1597–1617 MHz, L_2 = 1240–1260 MHz

produce a fundamental L-Band frequency of 10.23 MHz from which two carrier waves (L_1 and L_2, listed in table 2.2) are generated. The motive behind using the dual frequencies is to eliminate the major sources of errors (to be discussed in sub-subsection 2.4.2.3). During operation the L_1 carrier is modulated with two codes (also known as pseudo Random Noise, PRN), the C/A code (Coarse/Acquisition-code) and P-code (Precision-code), while L_2 is modulated only with the P-code. The C/A code is available for civilian use and the P-code is mainly for the United States Military (Hofmann Wellenhof et al., 2007).

2.4.2.2 GPS Observables

GPS observables are obtained by correlating the received and the receiver-generated signals, and the difference in time or phase is used to

determine the pseudoranges. They are called pseudoranges because they are biased by the satellite and receiver clock errors (Hofmann-Wellenhof et al., 1994). If the pseudoranges are obtained using the PRN C/A or P-code they are termed as "code pseudoranges", otherwise, the use of phase differences gives the "phase pseudoranges". The code (P_i) and phase (Φ_i) pseudoranges can be expressed mathematically as shown in equations 2.8a and 2.8b. Table 2.3 defines the symbols used.

$$P_i = \rho + c(dt_{sat} - dT_{rec}) + d\rho + d_{Tro} + I_i + b^s_{p_i} - b^r_{p_i} + \varepsilon(P_i) \quad (2.8a)$$

$$\Phi_i = \rho + c(dt_{sat} - dT_{rec}) + d\rho + d_{Tro} + \lambda_i N_i - I_i + b^s_{\Phi_i} - b^r_{\Phi_i} + \varepsilon(\Phi_i) \quad (2.8b)$$

2.4.2.3 Data Combinations

Equations 2.8a and 2.8b shows that both P_i and Φ_i pseudoranges are affected by different external factors which induce errors. To reduce the errors different data combinations are made. This subsection gives a brief description of the different types of combinations and their use.

The geometric free combination: Obtained by differencing the observables as shown in equations 2.9a and 2.9b.

$$P_2 - P_1 = PI \quad (2.9a)$$

$$L_2 - L_1 = LI \quad (2.9b)$$

Table 2.3: Definition of symbols used to express/describe pseudoranges

Symbol	Definition	Symbol	Definition
i	Index indicating modulation carrier frequency (L_i), $i = 1, 2$	I_i	Pseudorange ionospheric delays
P_i	Code pseudoranges	$\mathrm{b}^s_{p_i}$	Pseudorange satellite delays
Φ_i	Phase pseudoranges	$\mathrm{b}^r_{p_i}$	Pseudorange receiver delays
c	Speed of light (3.0×10^8m/s)	$b^s_{\Phi_i}$	Carrier phase satellite delays
ϱ	True geometric range between the satellite and the receiver	$\mathrm{b}^r_{\Phi_i}$	Carrier phase receiver delays
$\mathrm{d}\varrho$	Orbital error	λ_i	Carrier signal wavelengths
dt_{sat}	Satellite clock error with respect to GPS time	N_i	Carrier phase integer ambiguities
dT_{rec}	Receiver clock error with respect to GPS time	$\varepsilon(P_i)$	Pseudorange measurement noises which include multipath errors
d_{Tro}	Tropospheric error	$\varepsilon(\Phi_i)$	Carrier phase measurement noises with multipath errors included

Since the non-frequency dependent errors on the L_1 and L_2 signals are the same, this linear combination eliminates orbital errors, geometric range errors, clock errors and tropospheric delay factors, leaving only factors that depend on frequency (García, 2004).

The ionospheric free combination: Relies on the first order approximation of the ionospheric delay (I_i) which is inversely proportional to the square of the frequency (L_i),

$$I_i = \frac{A}{L_i^2} \tag{2.10}$$

where A is the constant of proportionality and i is either 1 or 2 (defined in table 2.3).

Solving for A gives $I_1 L_1 = I_2 L_2$ and a combination of the observables, as in equation 2.11a and 2.11b, removes the ionospheric contribution (Guochang, 2003).

$$\frac{L_1^2 P_1 - L_2^2 P_2}{(L_1^2 - L_2^2)} = PC \tag{2.11a}$$

$$\frac{L_1^2 L_1 - L_2^2 L_2}{(L_1^2 - L_2^2)} = LC \tag{2.11b}$$

The narrow (Pδ) and wide (Pδ) lane combinations: Obtain their names from the definition of wavelength (λ),

$$\lambda = \frac{c}{f} \tag{2.12}$$

where f is the frequency of the wave.

Noticeable from equation 2.12 is that $f = (L_1 + L_2)$ narrows λ, while $f = (L_1 - L_2)$ widens it. Thus, equations 2.13a and 2.13b are termed as narrow and wide lane combinations.

$$\frac{L_1.P_1 + L_2.P_2}{L_1 + L_2} = P\delta \tag{2.13a}$$

$$\frac{L_1.L_1 - L_2.L_2}{L_1 - L_2} = L\delta \tag{2.13b}$$

The wide lane combination is used in cycle-slip detection, since it provides a wide wavelength which is vital for this purpose.

2.4.3 Determination of Total Electron Content (TEC) from GPS Observables

TEC is defined as the total number of electrons integrated along the path of the signal from the transmitter (T_x) on the GPS satellite to the receiver (R_x) on the ground. TEC is measured in units of 10^{16} electrons per square meter, where 10^{16} electrons/m^2 = 1 TEC unit (TECU) (Davies and Hartmann, 1997). TEC is determined at a slant angle from the vertical (STEC) and then mapped to the vertical to provide VTEC. To generalize,

$$\text{TEC} = \int_{T_x}^{R_x} N_e ds_o \tag{2.14}$$

where ds_o is the element of geometric range.

To express TEC in terms of the observables, the geometric free combination (explained in sub-subsection 2.4.2.3) is used. This combination

can be expressed in code or phase pseudoranges as shown in equation 2.15a and 2.15b.

$$PI = P_2 - P_1 = I + b_p^s + b_p^r \tag{2.15a}$$

$$\Phi I = \Phi_2 - \Phi_1 = I + \lambda N + b_\Phi^s + b_\Phi^r \tag{2.15b}$$

where

$$I = I_2 - I_1 = A\left(\frac{1}{L_2^2} - \frac{1}{L_1^2}\right)$$

$$b_p^s = b_{p_2}^s - b_{p_1}^s,$$

$$b_p^r = b_{p_2}^r - b_{p_1}^r,$$

$$b_\Phi^s = b_{\Phi_2}^s - b_{\Phi_1}^s,$$

$$b_\Phi^r = b_{\Phi_2}^r - b_{\Phi_1}^r,$$

$$\lambda N = \lambda_2 N_2 - \lambda_1 N_1$$

and the thermal noise and multipath errors have been ignored.

Substituting for I in both equations 2.15a and 2.15b we obtain:

$$P_2 - P_1 = A\left(\frac{1}{L_2^2} - \frac{1}{L_1^2}\right) + b_p^s + b_p^r \tag{2.15a}$$

$$\Phi_2 - \Phi_1 = A\left(\frac{1}{L_2^2} - \frac{1}{L_1^2}\right) + \lambda N + b_\Phi^s + b_\Phi^r \tag{2.15b}$$

The value of the constant A depends on electron density and is expressed in terms of TEC as, A = 40.3 TEC (Seeber, 2003).

Substituting for A and solving for TEC in both cases we obtain

$$\text{TEC}_P = \frac{1}{40.3}\left(\frac{L_1^2 L_2^2}{L_1^2 - L_2^2}\right)\left\{(P_2 - P_1) - \left(b_p^s + b_p^r\right)\right\} \tag{2.16a}$$

or

$$\text{TEC}_\Phi = \frac{1}{40.3}\left(\frac{L_1^2 L_2^2}{L_1^2 - L_2^2}\right)\left\{(\Phi_2 - \Phi_1) - \lambda N - (b_\Phi^s + b_\Phi^r)\right\} \tag{2.16b}$$

A look at equation 2.16a and 2.16b indicates that the use of code pseudorange measurements provides an unambiguous but imprecise observable due to the presence of noise, while the use of phase pseudorange measurements provides a precise but ambiguous measurement due to the presence of the integer ambiguities (Carrano and Groves, 2009). If, however, the biases and the carrier phase integer ambiguities are considered to be negligible, substituting for the frequencies L_1 and L_2 gives

$$\text{TEC}_P = 9.524\ (P_2 - P_1)\ \text{TECU} \tag{2.17a}$$

or

$$\text{TEC}_\Phi = 9.524\ (\Phi_1 - \Phi_2)\ \text{TECU} \tag{2.17b}$$

The two equations can further be used to calculate the relative STEC and the biases. For more information refer to Burrell et al. (2009).

2.5 Models

This subsection gives a brief insight into the two ionospheric models that were used in this study, namely the International Reference Ionospheric (IRI) model and the South African Bottomside Ionosphere Model (SABIM).

2.5.1 International Reference Ionospheric (IRI) Model

The IRI model is a climatological model that is internationally recognised and recommended for prediction of plasma parameters values in the Earth's ionosphere (Bilitza et al., 2011). It was established in 1960 as a joint model of the URSI (Union Radio Scientifique International) and COSPAR (Committee On Space Research) task groups. The first version was produced with the intention of creating a standalone model that could predict the global and temporal mean behaviour of the undisturbed ionospheric parameters (Bilitza, 1986). The development of the IRI was based on the available worldwide ground-based data as well as data from satellite observations. Being a data-based model, its accuracy in a specific region or time period depended on the availability of reliable data for the specific region and time. Therefore, the IRI model is being continually improved with new data and improved modelling techniques by a group of experts spanning the globe (Bilitza and Reinisch, 2008). These improvements have resulted in several versions of IRI, the latest being IRI-2012, which was used in this study.

2.5.1.1 IRI Inputs and Output

The IRI model can either be run online (`http://omniweb.gsfc.nasa.gov/vitmo/iri2012_vitmo.html`) or downloaded in FORTRAN code (`irimodel.org/`). The model's inputs can be classified as either "required inputs" or "optional inputs", depending on the required output. In this study the required output is the electron density profile at every geographical location on the map. Thus, the required inputs include: geographical latitude, geographical longitude, year, day number (day of the year), hour, the solar indices, ionospheric index and magnetic index.

Solar Indices: These include the F10.7 and R12 indices. The F10.7 index indicates the power flux of the radio solar noise measured at a wavelength of 10.7cm. The R12 index provides an indication of the solar cycle in terms of an index. It is calculated as a running mean of the sunspot number over the 12-month period (Perrone and De Franceschi, 1998).

Ionospheric Index: Labelled as "IG12" and calculated using both solar and ionospheric information over a 12-month running mean. The index offers a better estimation of the foF2 parameter than the R12 index (Liu and Smith, 1983).

Magnetic Index: Indicates the relationship between magnetic perturbations and magnetospheric phenomena. The perturbations are regarded as regular, or irregular depending on the scale (Kp-index) developed by Bartels et al. (1939). The Kp-indices from observatories around the globe are averaged on a 3-hour or daily interval and used to determine the global index (ap), which is used in the IRI model.

For more information on the scaling of the indices, refer to a paper by Bartels (1957).

2.5.1.2 IRI Limitations

Although the IRI model is continually being improved, the model has its limitations:

- The model is based on monthly averages and the averaging process smoothes out some of the small variations (Bilitza et al., 2011). For example, McNamara et al. (2010) found that the four maxima structures in the longitudinal variation of F-peak electron density that were observed by IMAGE/EUV, were reproduced by IRI, but with reduced amplitudes due to the averaging process.
- IRI is an empirical model of which the accuracy depends on the underlying database. The use of the model in regions that are not well covered by the database produces inaccurate results, such as in the prediction of the global F-peak density. The model performs best at continental northern mid-latitudes because that is the region with the highest density of ionosondes stations and many of these stations have been operating over a long time period (Bilitza et al., 2011).

2.5.2 South African Bottomside Ionospheric Model (SABIM)

SABIM is a South African regionally based bottomside ionosphere model. The model was developed with the primary aim of addressing

the inaccuracies of ionospheric modelling over the South African region (McKinnell and Poole, 2004).

The first version of the SABIM model was called the LAM model and was developed using data from one station (Grahamstown (33.3° S, 26.5° E)). This station at that time had the largest database, covering over 30 years of ionospheric observation. The large database influenced the decision to use the Neural Network (NN) technique, which requires a large archived database describing the history of the relationship between the input and the required output parameters. A NN is a computer program that is trained by presenting any number of multidimensional input vectors that correspond to a known measured parameter. An NN then learns to identify the relationship between the input vectors and the known output (McKinnell, 2003). In the case of the LAM model the inputs included: the day number (DN), hour (HR), a measure of solar activity (R) and a measure of magnetic activity (A). The outputs were the values of the parameters required for constructing the bottomside ionosphere profile. The results of the LAM model were more successful at predicting the electron density profile for a particular set of inputs than the IRI (McKinnell, 2003).

With time the ionosonde network was expanded to include two more ionosondes that were installed at Louisvale (28.5° S, 21.2° E) and Madimbo (22.4° S, 30.9° E). This led to the expansion of the LAM model to cover the available South African region. The model was renamed SABIM and the input parameters were modified to include geographic latitude and longitude. Figure 2.2 shows the input parameters and the

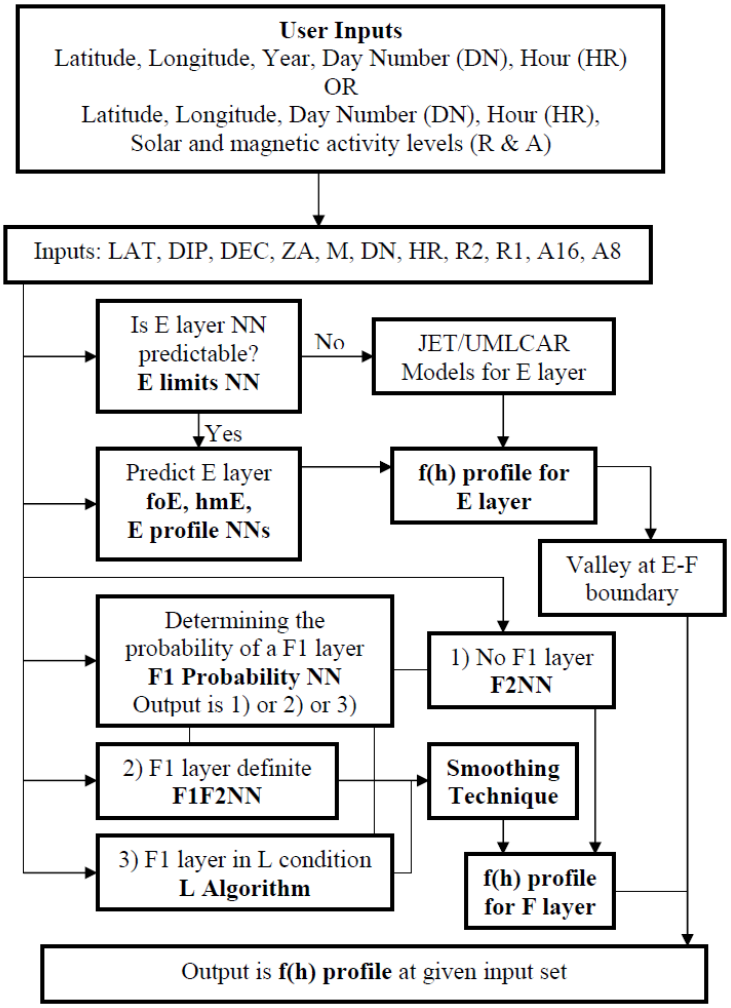

Figure 2.2: A flow diagram depicting the process followed by the SABIM model in determining the bottomside ionosphere profile (McKinnell, 2008a).

process followed by the SABIM model to generate the required bottom-side ionosphere profile.

2.5.2.1 SABIM Limitations

Since SABIM is an NN-based model its limitation lies in the availability of data to train the NNs. To overcome this problem the model is being continually updated every 2 years with new ionosonde data. Since inception, different versions (version 1 to version 4) have been produced, the latest covering 1996 - 2010. In chapter 3 a validation of the prediction of the foF2 parameter over the South African region by the most recent version of SABIM, will be discussed.

2.6 Summary

This chapter covered the basic background theory pertaining to the ionosphere and the parameters that define it. Two ionospheric measurement techniques were described, as well as the use of ground-based ionosondes and the GPS system. A brief description of two ionospheric models (IRI and SABIM) which were used as data sources for the AIM was given. The improvement and validation of the South African Ionospheric Map (SAIM) will be discussed in the next chapter.

Chapter 3

SAIM Improvement and Validation

3.1 Introduction

The South African Ionospheric Map (SAIM) was developed to show the variation of the ionosphere over the South African region (ranging 12^o - 40^o S, 10^o - 40^o E) using the available ionospheric data sources, namely the South African ionosonde network, the IRI-2007 model and SABIM. The objective of the SAIM project was to develop a tool that could help radio communication companies in South Africa to correct for ionospheric effects and also improve direction finding in HF radio sounding. SAIM was developed using MATLAB and produces maps of TEC, foF2 and the electron density profiles for a given set of input parameters. This chapter focuses on the upgrade of the SAIM (with the new IRI-2012 model and the latest version of the SABIM model) and the validation of the results. The new version of the SABIM model is also validated before use in SAIM.

3.2 South African Ionosonde Network

Ionospheric sounding over South Africa dates back more than 30 years. Grahamstown (33.3^o S, 26.5^o E) is the oldest ionospheric station and started sounding in 1973 using a Barry Research chirp sounder (McKinnell, 2008b). In 2000, the network was expanded to three ionosondes (Model DPS-4, where DPS stands for Digital Portable Sounder) which were purchased from the University of Massachusetts, Lowell Center for Atmospheric Research (UMLCAR) and installed at three locations, namely Grahamstown (33.3 ^{o} S, 26.5^o E), Louisvale (28.5^o S, 21.2^o E) and Madimbo (22.4^o S, 30.9^o E). The main aim of these installations was to provide real-time scaled ionospheric parameters which could be used in frequency channel selection for HF communication. Further, in 2008, the South African Department of Communications donated an ionosonde to expand the network to a fourth location, namely at Hermanus (34.2^o S, 19.2^o E). The Hermanus ionosonde is a DPS-4D model (where the D stand for digital transmitters and receivers) and the first of its kind to be installed in the world. This ionosonde has better capabilities than the DPS-4: it can perform drift measurements to look at ionospheric tilt, angle of arrival and phase measurements of the incoming signal, Doppler velocity and oblique soundings (Reinisch, 2009). In 2011 the other three stations were upgraded to the DPS-4D model.

Figure 3.1 shows the map of South Africa indicating the location of the 4 ionosondes, a picture of the DPS-4D and an example of a data

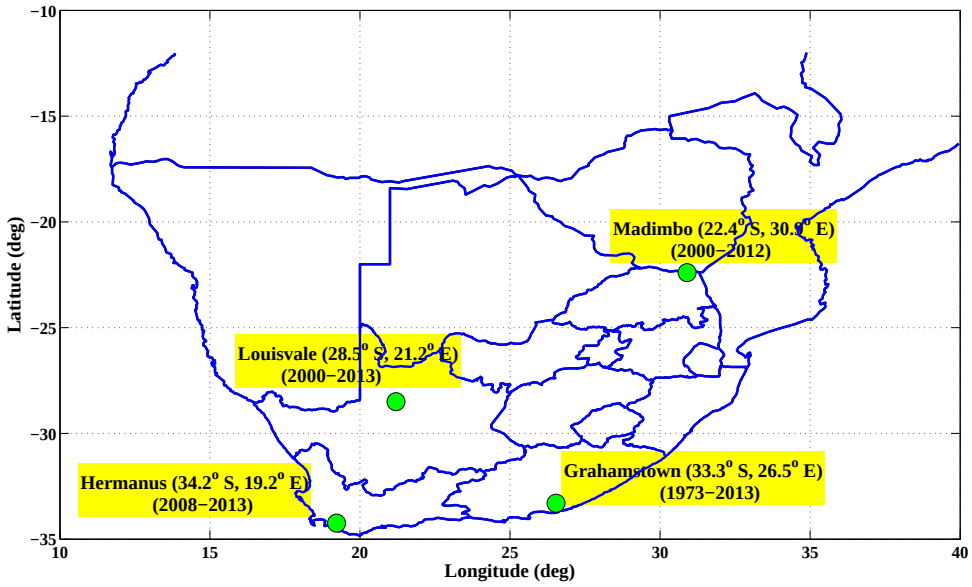

(a)

(b)

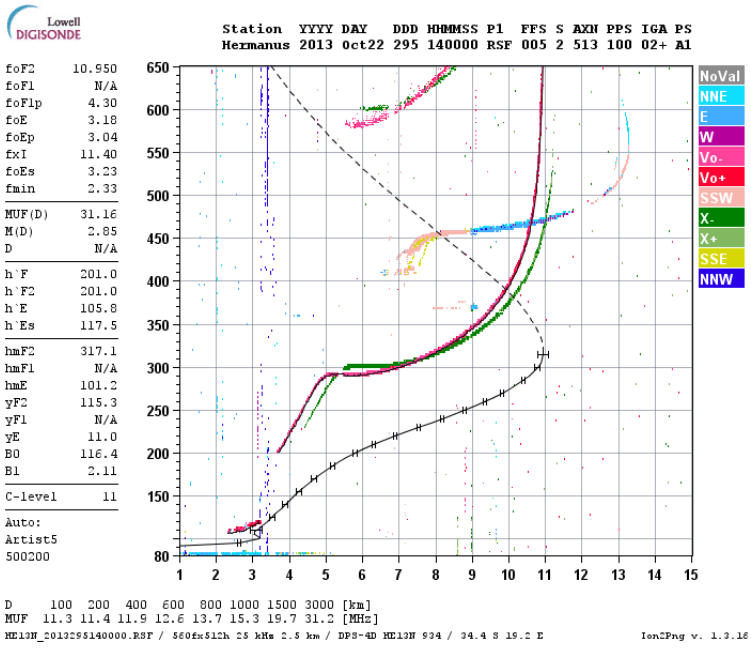

(c)

Figure 3.1: (a) a map showing the South African ionosonde network, (b) DPS-4D and (c) an ionogram recorded at the Hermanus ionosonde station.

product: a typical ionogram (the ionosphere profile) recorded at the Hermanus station.

The collected data from the South African ionosonde network is sent in real time to a central archiving centre at the South African National Space Agency (SANSA) in Hermanus. The information is published on the web and made available to the global community, via various websites, including the Space Physics and Interactive Data Resource (SPIDR) and the Digital Ionogram Database (DIDBASE) (McKinnell, 2008b).

In SAIM the ionosonde data is recorded in the SAO.XML file format (which is a physical data format for the ionogram-derived data). SAO stands for Standard Archival Output and XML for eXtensible Markup Language. Once SAO.XML is generated, the document holds a single element SAORecordList that may have multiple sub-elements, each corresponding to one set of ionogram-derived data obtained for one ionogram (Reinisch et al., 2012).

During the development of the first version of SAIM, the SAO.XML data from Louisvale and Madimbo stations had a resolution of 30 minutes while Grahamstown and Hermanus stations had a 15 minute resolution, and so the SAIM was set to a temporal resolution of 30 minutes. Currently, all the ionosondes are set to a 15 minute resolution and so is the current version of SAIM.

3.3 SABIM Improvement and Validation

Since its inception most versions of the SABIM model were trained with data from only three ionosondes locations: Grahamstown, Louis-

vale and Madimbo (see sub-section 2.5.2). The ionosonde network has now grown to include data from Hermanus which was a previously unrepresented area. The new version of SABIM was updated with this additional data and refined. In this sub-section the new SABIM model is validated for the critical frequency (foF2) of the F2 layer by comparing the model's output with the measured ionosonde data and the IRI-2012 model during diurnal, seasonal and solar cycle variations. The data set used in the analysis covers the period 2000 to 2010.

3.3.1 Diurnal Variation

Figure 3.2 shows the diurnal variation of the foF2 values from the SABIM model, the IRI-2012 model and the four ionosondes stations (Grahamstown, Louisvale, Madimbo and Hermanus). During equinox (figure 3.2a) in March and solstice (figure 3.2b) in June of 2010, the SABIM model shows an improved prediction of the foF2 values over the IRI-2012 model between 06:00 UT and 15:00 UT (South African Standard Time, SAST = UT + 2). This is very evident at the Hermanus station where the IRI-2012 model is seen to underestimate and overestimate the foF2 values during equinox and solstice respectively.

3.3.2 Seasonal Variations

Figure 3.3 shows a plot of annual foF2 values from the SABIM model, the IRI-2012 model and the four ionosonde stations, before local sunrise (02:00 UT), noon (10:00 UT) and after sunset (18:00 UT) in 2010.

At local sunrise (figure 3.3a) the IRI-2012 model shows an underestimation of the foF2 values throughout the year, whereas the SABIM

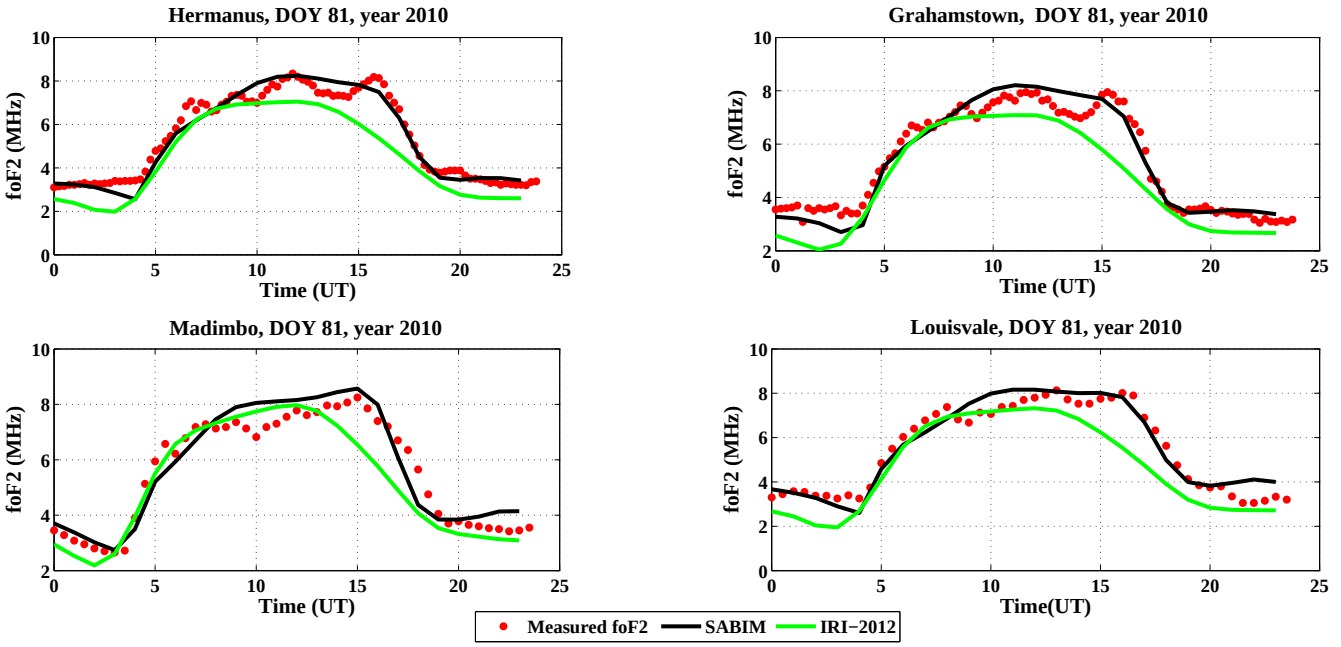

(a)

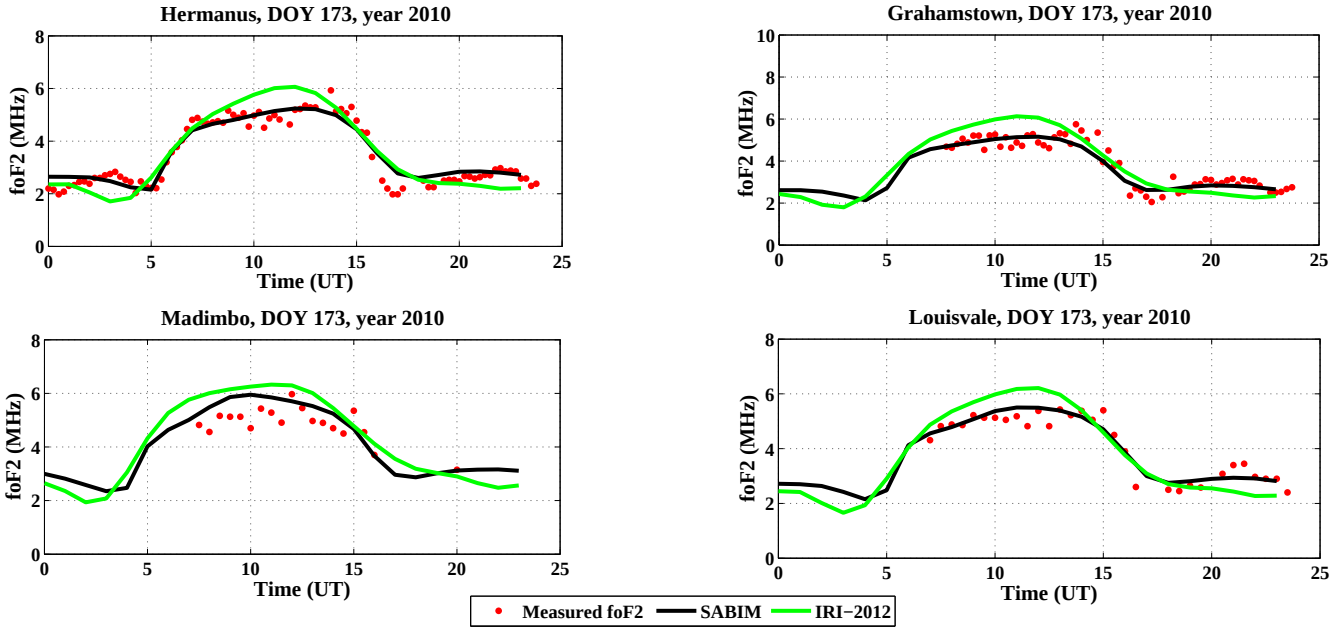

(b)

Figure 3.2: A comparison of diurnal foF2 values from the SABIM model, the IRI-2012 model and the ionosondes (Hermanus, Grahamstown, Louisvale and Madimbo). (a) equinox in March (Day of Year (DOY) 81) 2010, and (b) solstice in June (DOY 173) 2010.

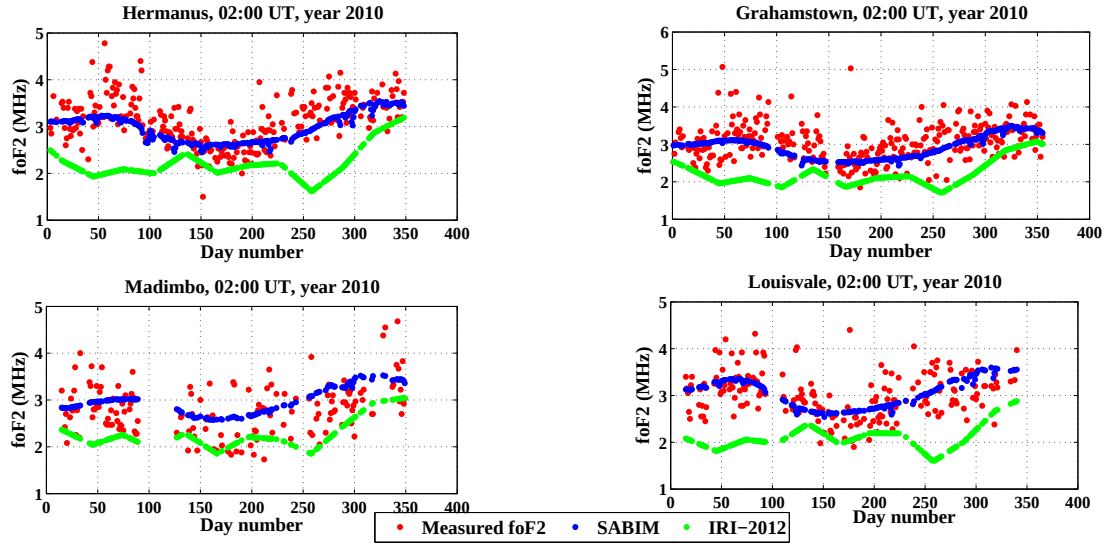

(a)

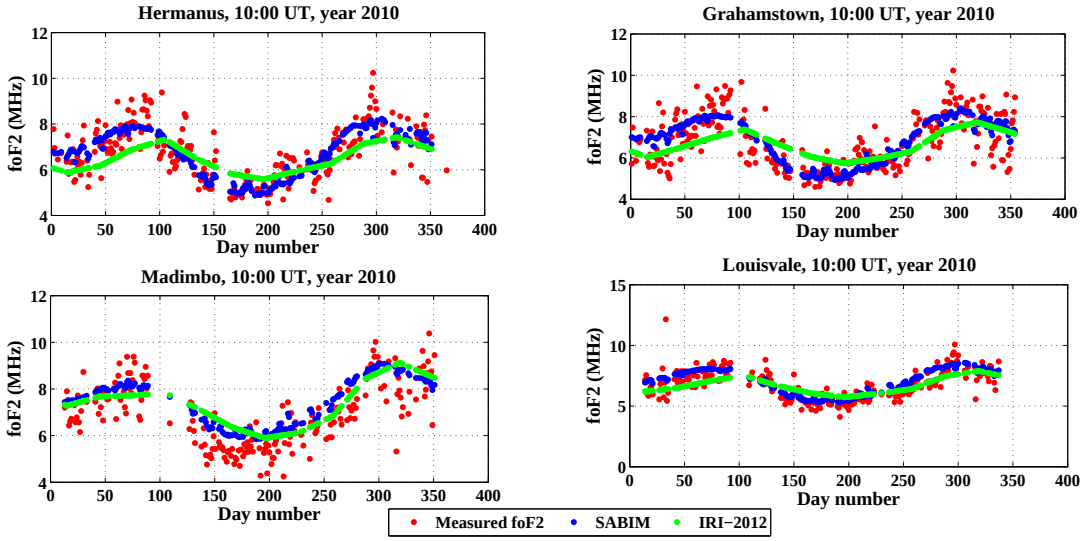

(b)

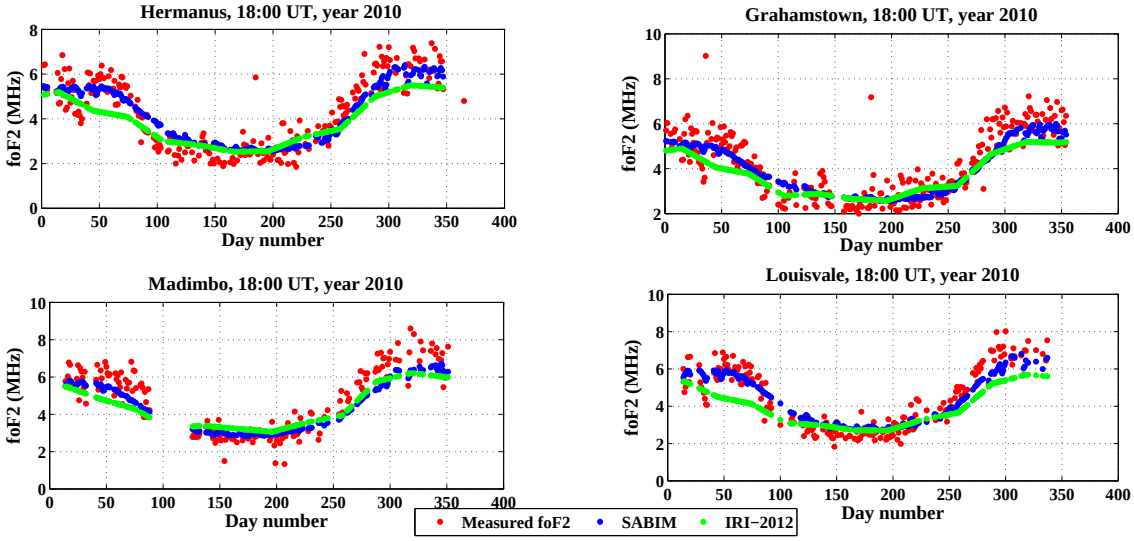

(c)

Figure 3.3: Annual variation of foF2 values from the ionosondes (Hermanus, Grahamstown, Louisvale and Madimbo), the SABIM model and the IRI-2012 model. (a) before sunrise 02:00 UT (04:00, SAST), (b) local noon 10:00 UT (12:00, SAST) and (c) after sunset 18:00 UT (20:00, SAST).

model produces a more accurate estimation. This is observed at all four ionosonde stations.

At local noon (figure 3.3b) and sunset (figure 3.3c) both models, SABIM and IRI-2012, show a good estimation of the foF2 values. However, at local noon the seasonal changes are well-defined and so a further analysis of these results was performed.

Residues of the measured foF2 values and the output from each of the models were determined for the local noon time at all four stations as shown in figure 3.4. The results were then binned according to the days of the year, 0 - 100, 101 - 250 and 251 - 365. The data in each bin for every station was averaged and the overall mean for the four stations also determined. The results are given in table 3.1.

The results show that the SABIM model performs better than the IRI-2012 model both during summer (DOY, 0 - 100) and winter (DOY, 101 - 250). This is most visible at the Grahamstown and Hermanus stations. The overall average values indicate that the SABIM model performs better during winter than during summer.

The Root Mean Square Error (RMSE) was determined from the residues at each ionosonde location and the overall average determined. The SABIM model performed better than the IRI-2012 model, with an RMSE of 0.78 MHz compared to 0.93 MHz of the IRI-2012 model.

3.3.3 Solar Cycle Variation

For this validation, data from the years 2000 and 2006 were chosen to represent solar maximum and solar minimum respectively and the 10:00 UT foF2 values were chosen for analysis.

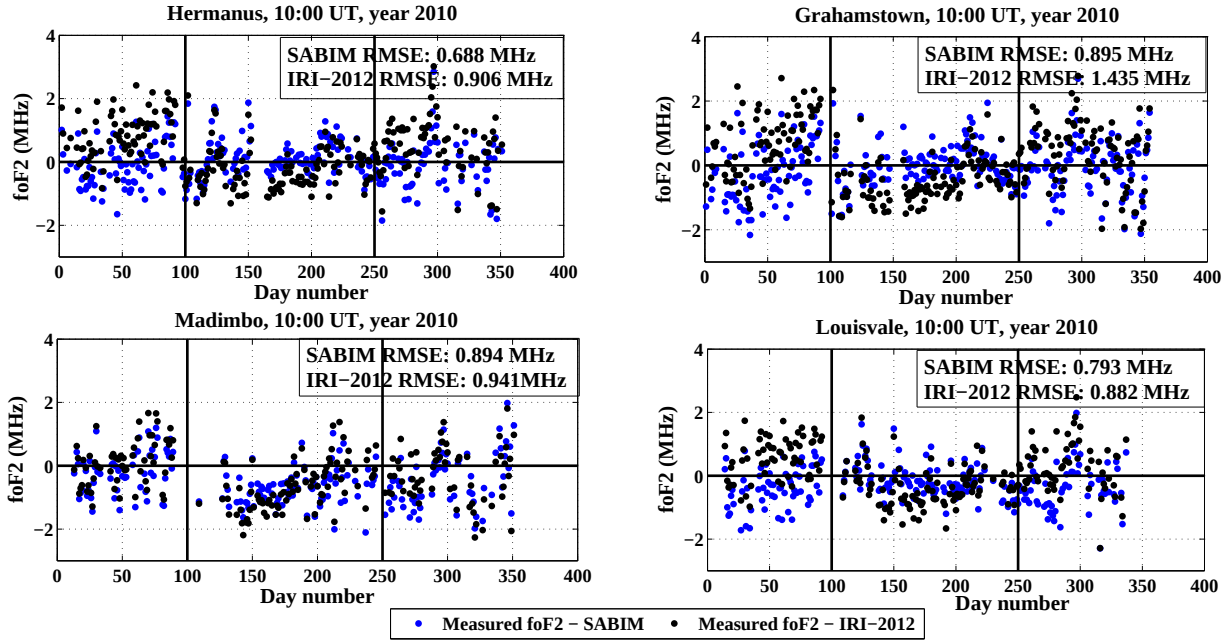

Figure 3.4: Annual variation of residues between the measured local noon (10:00 UT) foF2 values and the output from the models (SABIM and IRI-2012) for all 4 ionosonde stations.

Table 3.1: Mean difference between measured foF2 values and results from models, SABIM and IRI-2012, based on the DOY in 2010

	DOY	Grahamstown (MHz)	Hermanus (MHz)	Madimbo (MHz)	Louisvale (MHz)	Average (MHz)
SABIM	0 - 100	-0.093	-0.218	-0.185	-0.291	-0.197
	101 - 250	0.114	0.015	-0.667	-0.158	-0.174
	251 - 365	-0.119	-0.070	-0.505	-0.372	-0.266
IRI	0 - 100	0.808	0.700	0.108	0.108	0.431
	101 - 250	-0.228	-0.423	-0.669	-0.377	0.424
	251 - 365	0.483	0.348	-0.352	0.275	0.188

Figure 3.5 shows a plot of the 10:00 UT foF2 values from the three ionosonde stations (Grahamstown, Madimbo and Louisvale), and the SABIM and IRI-2012 models during solar maximum (figure 3.5a) and during solar minimum (figure 3.5b). The Hermanus ionosonde was omitted in this analysis since the station did not exist during that period. The output from both models was down-sampled to match the measured foF2 data. Therefore, the gaps seen in the plots are a result of missing ionosonde values.

The RMSE values were determined during solar maximum and during solar minimum at the three ionosonde stations. The results (see table 3.2) show that both models (SABIM and IRI-2012) perform better during solar minimum than during solar maximum. Furthermore, the SABIM model performed 27 % better than the IRI-2012 model during solar maximum (using only the Grahamstown station with the most continuous data) and better 14.7 % during solar minimum (using data from three stations, Grahamstown, Madimbo and Louisvale).

Scatter plots were drawn for the measured foF2 values and the output from each of the two models during solar maximum (figure 3.6a) and during solar minimum (figure 3.6b). A line of best fit (y) was inserted in each plot and the correlation coefficient (R) determined at each station.

During solar maximum (again using data from only the Grahamstown station), the SABIM model gave a higher R value of approximately 0.80 compared to 0.65 by the IRI-2012 model. During solar

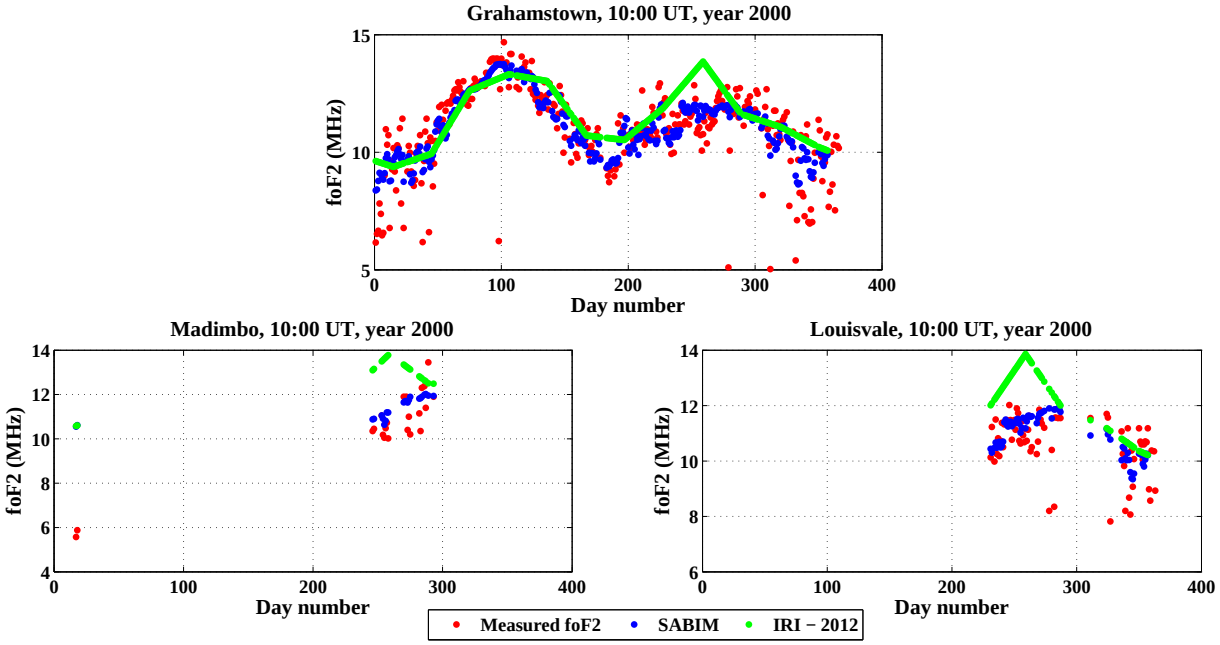

(a)

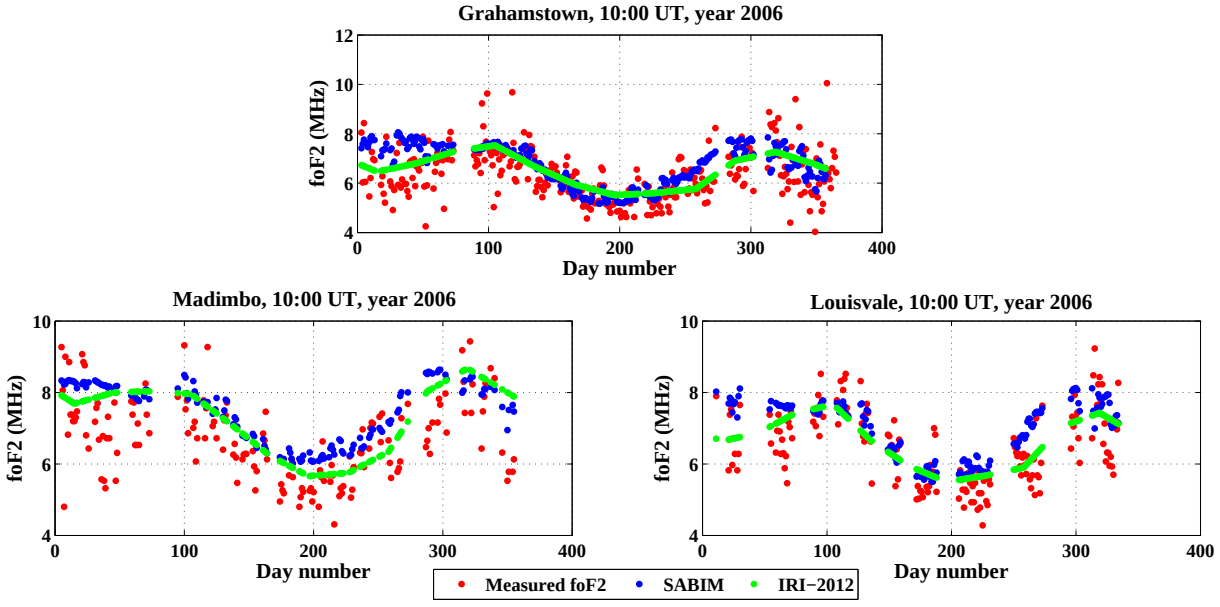

(b)

Figure 3.5: Ionosondes (Grahamstown, Madimbo and Louisvale), SABIM and IRI-2012 10:00 UT foF2 annual variation. (a) during solar maximum and (b) during solar minimum.

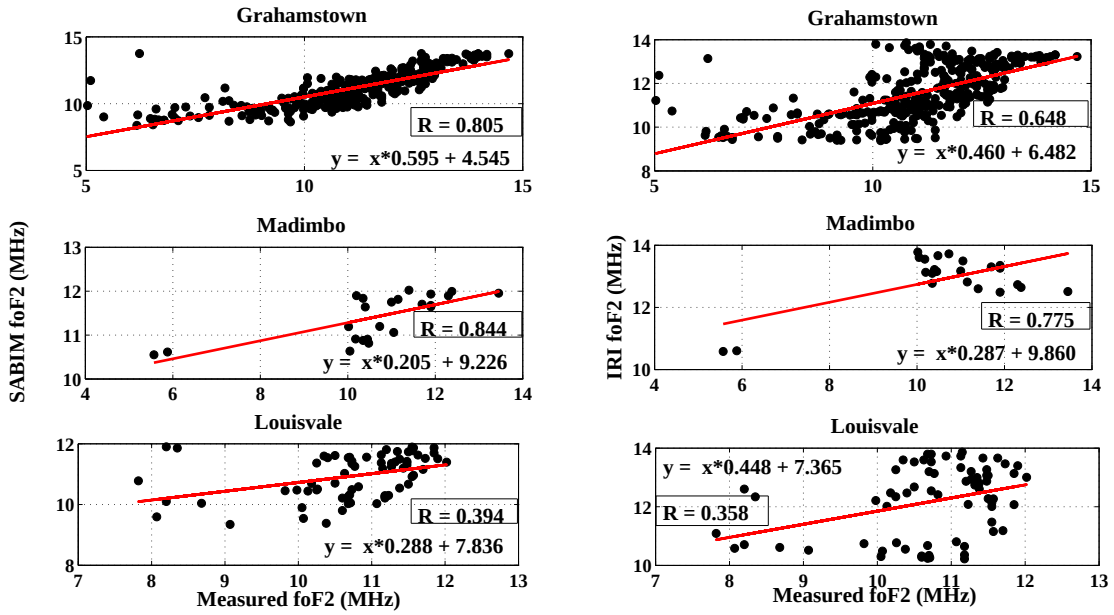

(a) Solar maximum (2000)

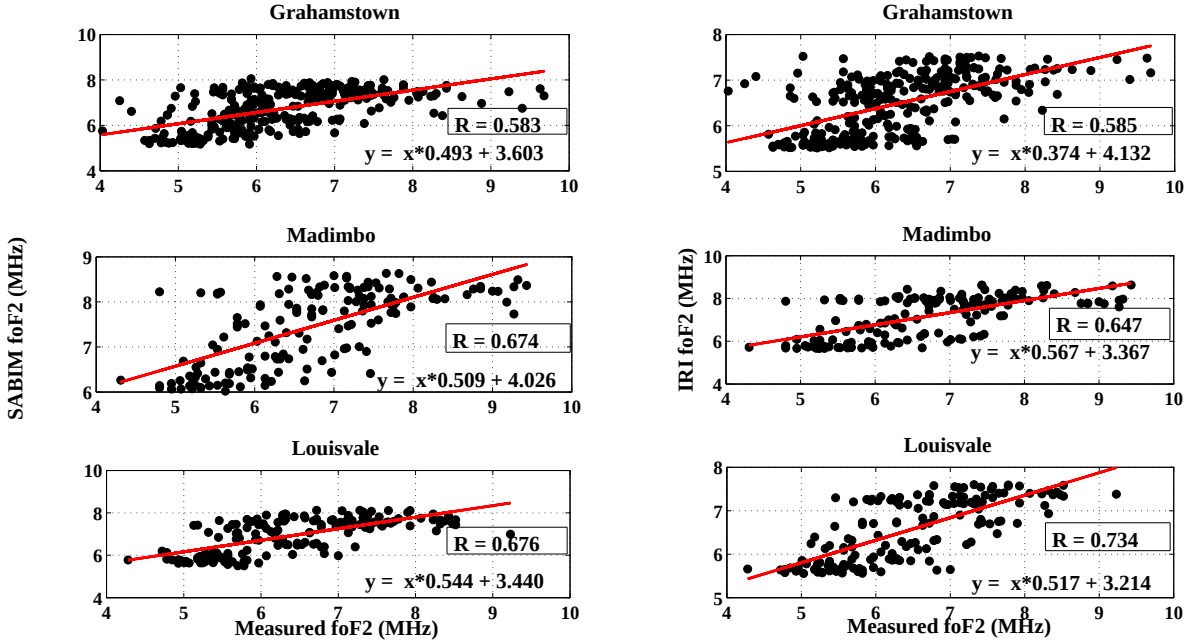

(b) Solar minimum (2006)

Figure 3.6: Scatter plots of annual foF2 values during solar maximum (figure 3.6a) and during solar minimum (figure 3.6b) at three ionosonde stations, Grahamstown, Madimbo and Louisvale. The left and right panels represent results from the SABIM model and the IRI-2012 model respectively.

Table 3.2: RMSE for the SABIM and IRI-2012 model for the years 2000 (solar maximum) and 2006 (solar minimum)

	Year	Hermanus (MHz)	Grahamstown (MHz)	Louisvale (MHz)	Madimbo (MHz)
SABIM RMSE	2000	-	1.047	0.966	0.592
	2006	-	0.825	0.695	0.994
IRI-2012 RMSE	2000	-	1.435	1.911	0.709
	2006	-	0.939	0.910	1.103

minimum (using all three stations) both models displayed an average R value of approximately 0.65.

3.4 SABIM Run Time

The old and new versions of SABIM were set to run the same task under the same conditions and the run time determined. The results displayed in table 3.3 indicate that the new version of SABIM is 4 times faster than the old version. This faster processing time will in return reduce the response time of SAIM.

3.5 Use of SABIM, IRI-2012 and Ionosonde Data in SAIM

3.5.1 SABIM and IRI-2012

For the purpose of using the two models in this work, executable programs were created from the Fortran (IRI-2012) and C++ (SABIM) codes using the gcc and Microsoft Visual C++ 2010 compilers respectively.

The use of the SABIM model in SAIM was previously limited to a triangular region formed by the three ionosonde stations, Grahamstown, Madimbo and Louisvale, the data of which data had been used during

Table 3.3: Run times of the new and old SABIM models

SABIM	Old	New
Windows version number	Windows NT 5.1 (Build 2600)	Windows NT 5.1 (Build 2600)
Exit time	4:11 pm, Sunday, July, 2012	4:03 pm, Sunday, July, 2012
Elapsed time	0:04:33.812	0:01:24.687
Process time	0:04:12.078	0:01:04.875

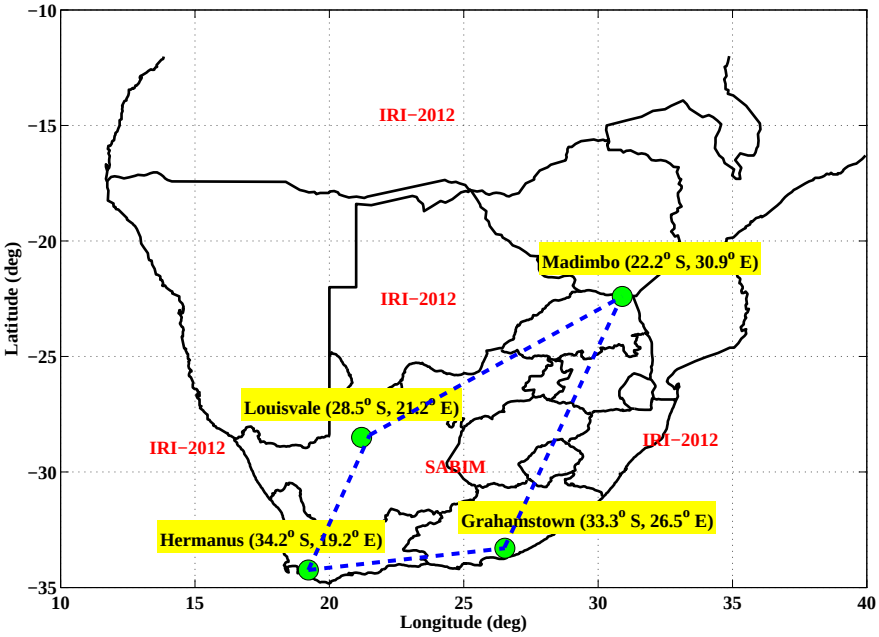

Figure 3.7: South African map indicating the regions where the SABIM and IRI-2012 models were used in developing the SAIM.

the model development. The newer version of SABIM has been trained by data from four ionosonde stations, thus expanding the region covered by the SABIM model to a quadrilateral region as shown in figure 3.7.

The IRI-2012 model was used outside of the quadrilateral region. Furthermore, a smoothing function was introduced at the boundary of the two models such that the SABIM model still contributed outside of the quadrilateral region. The smoothing function used is

$$f = f_s \cos^2 \beta + f_i \sin^2 \beta, \;\; \beta = \frac{90d}{1117} \tag{3.1}$$

where f_s is SABIM's foF2 value for a location outside the quadrilateral region, f_i is IRI-2012's corresponding foF2 value for that location, f is the resulting foF2 value for the location and d is a measure of the point's distance from the closest edge of the quadrilateral (Okoh et al., 2010). Further information on how the SABIM and IRI-2012 models are combined is found in a master's thesis written by Okoh (2009).

3.5.2 Ionosonde Data

Measurements by the ionosondes were used to adapt the model output to the ionosonde measurements. In the case of foF2 map generation, the program calculates the residues of the measured foF2 and the modelled foF2 at each ionosonde location, and then fits the best plane by the method of least squares. Depending on the obtained values, the plane values are added to or subtracted from the existing modelled map in order to adapt it to the ionosonde measurements (Okoh, 2009).

3.6 SAIM Validation

The validation of SAIM was based on the ionospheric foF2 diurnal, seasonal and solar cycle variation. In addition, the electron density profiles generated by the SAIM program were compared to the measured profiles from the ionosondes.

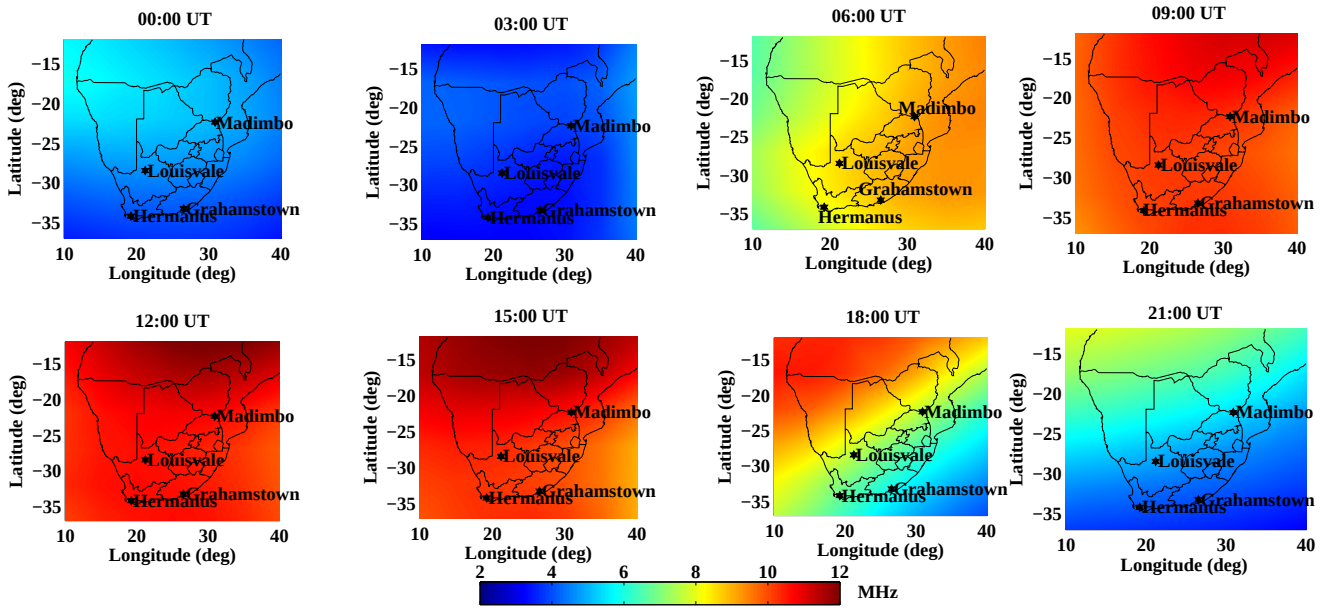

Figure 3.8: Diurnal maps of the foF2 parameter generated by SAIM.

3.6.1 Diurnal Variation

Figure 3.8 shows diurnal foF2 maps generated by the SAIM program, using a resolution of 3 hours on an arbitrarily chosen DOY 267, 2010. The ionosonde stations are indicated in black since the ionosonde data was not included.

The maps show the expected variation in foF2 which increases from low level intensity at night (00:00 - 03:00 UT), peaks during the day (06:00 - 15:00 UT) and decreases again after sunset (18:00 - 21:00 UT).

3.6.2 Seasonal Variation

Figure 3.9 shows 10:00 UT foF2 maps generated for 4 days, each corresponding to a different season (summer (DOY 46), autumn (DOY 135), winter (DOY 196) and spring (DOY 258) of the year 2010. The annual foF2 variation is well-depicted in the plots. Ionospheric ionisa-

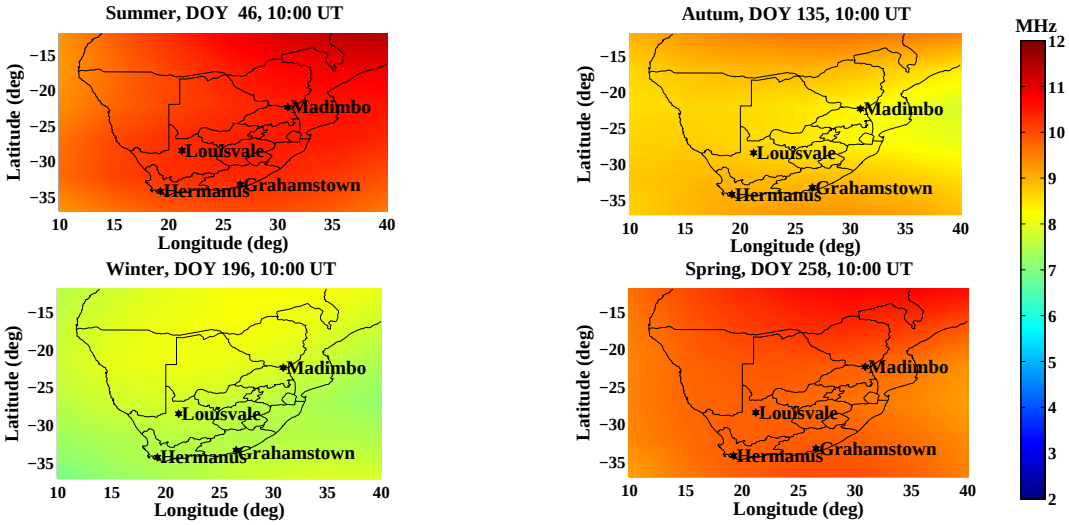

Figure 3.9: Seasonal variations: summer, autumn, winter and spring in 2010.

tion is seen to be more pronounced during summer and least during winter.

3.6.3 Solar Cycle Variation

Figure 3.10 shows 10:00 UT foF2 maps generated for an arbitrarily chosen DOY (202) during solar maximum (2000) and during solar minimum (2006). The maps show a distinct difference in the intensity of the foF2. During solar maximum the foF2 values reach 12 MHz as compared to 6 MHz during solar minimum. These variations are due to the amount of solar radiation emitted by the sun being strongest during solar maximum and least during solar minimum (see chapter 2).

3.6.4 Electron Density Profiles

To generate the profiles, the SAIM program passes the calculated foF2 and hmF2 values for any chosen location to the IRI-2012 model as inputs. The IRI-2012 model then uses the inputs to re-adjust and

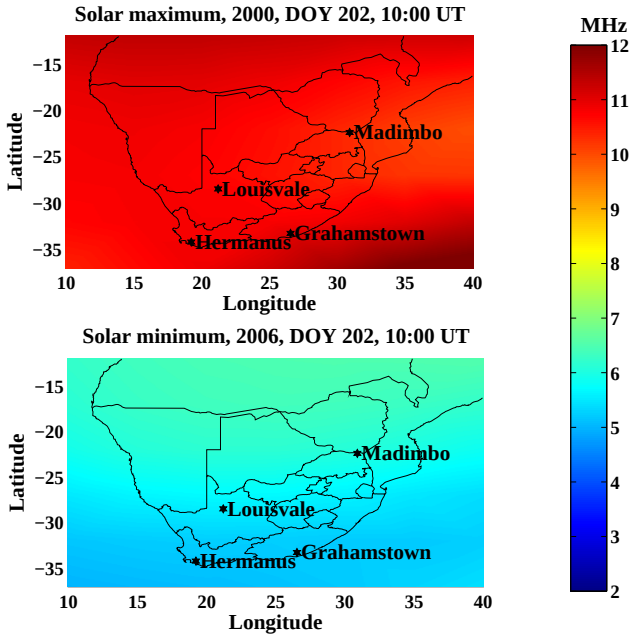

Figure 3.10: foF2 maps on an arbitrarily chosen DOY (202) during solar maximum (2000) and during solar minimum (2006).

generates the required profile. Figure 3.11 shows a comparison of the SAIM profiles and the measured profiles from three ionosonde stations (Hermanus, Grahamstown and Louisvale) in different seasons (summer (DOY 45), autumn (DOY 100), winter (DOY 182) and spring (DOY 246)) of 2012. The Madimbo ionosonde station was not included in the analysis since it was not operational during this period due to technical problems.

For each season, the SAIM shows a good estimation of both the foF2 and hmF2 values. On average the absolute difference between

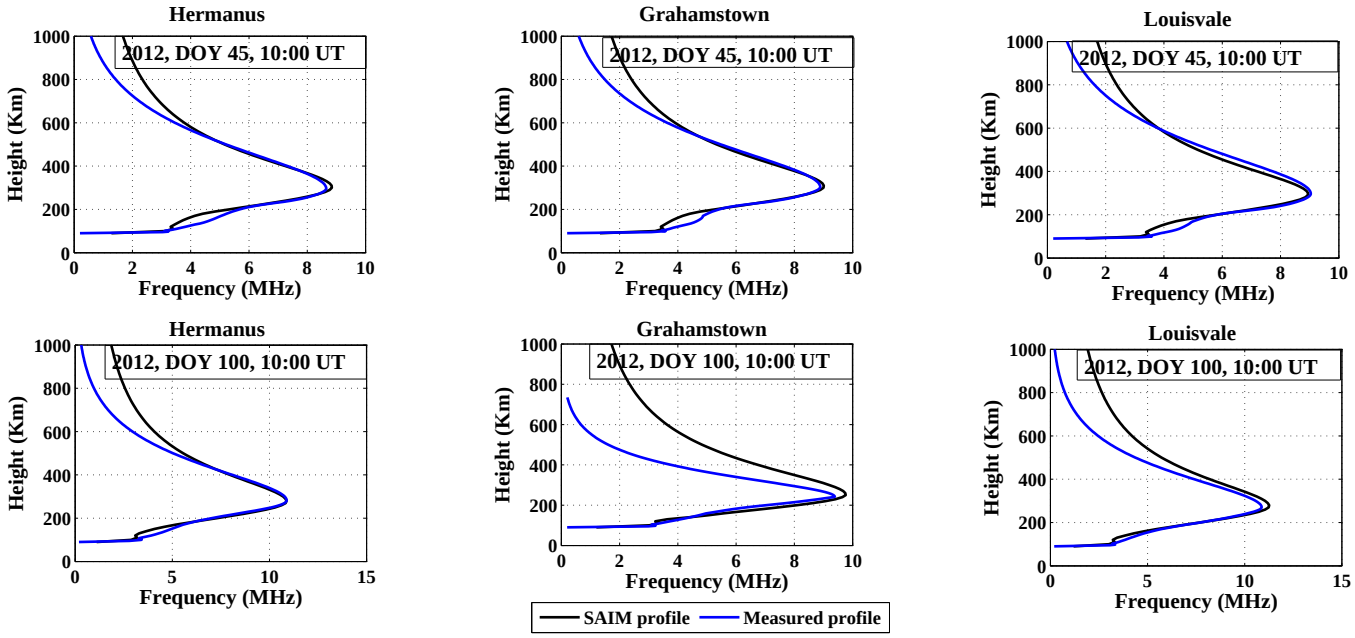

(a)

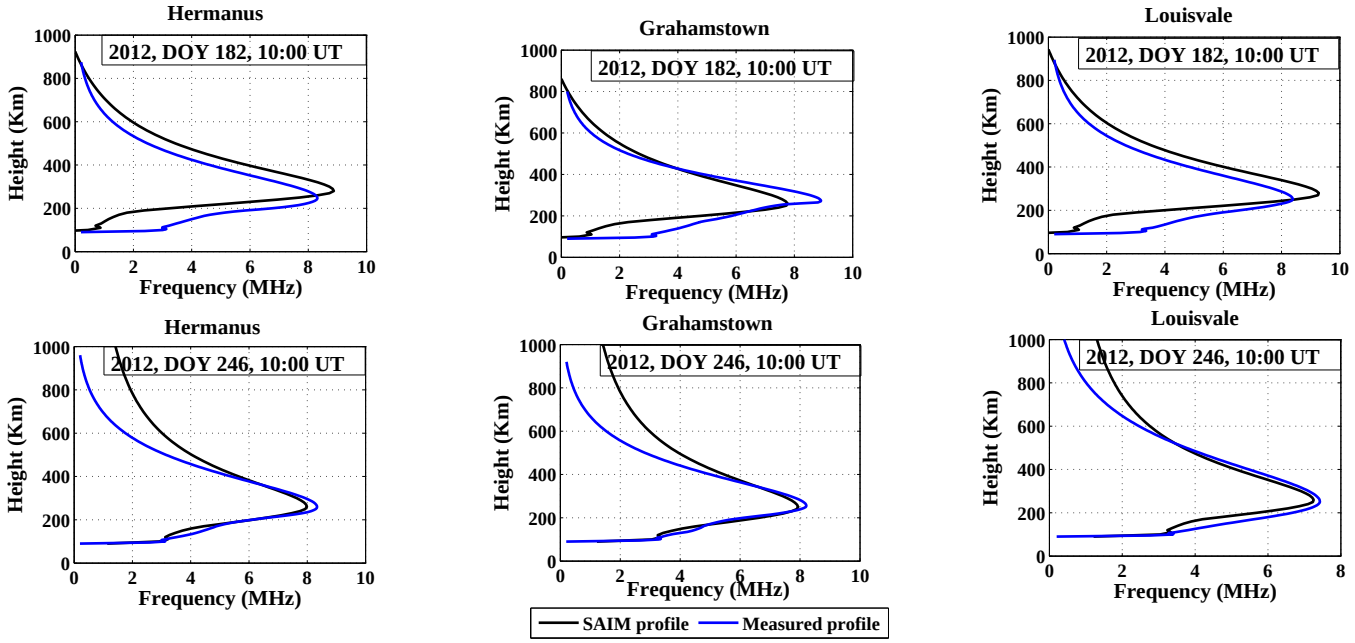

(b)

Figure 3.11: A comparison of SAIM profiles and ionosonde profiles from three stations: Hermanus, Grahamstown and Louisvale, for (a) summer (DOY 45) and autumn (DOY 100) in 2012, and (b) winter (DOY 182) and spring (DOY 246) in 2012.

the measured and estimated foF2 values was found to be 0.04 MHz, compared to 0.16 MHz by the previous version of SAIM.

3.7 Interface Change

A number of changes were made to SAIM's interface to make the map more user friendly. Figure 3.12 shows the new interface. The circled options are the added new functions.

ftp access: In the previous version of SAIM the ftp access details (ftp site, user name and password) of the ionosonde server were "hard-wired" into the program. For the details to be changed, the source code had to be updated and a new standalone program created. The new interface "ftp login" option gives the end user the ability to change the access details without having to change the source code. If the access to the ftp server fails, the program lets the user know by displaying an error message "Connection to the ftp server failed" and then continues to generate the required map using the SABIM model and the IRI-2012 model.

If the end user wishes to continue running the SAIM using the same access details for a given session, the radio button "Don't show again" is activated. The access details are then stored in the computer memory and invoked internally every time a new map is generated.

Hold on and Clear: This option lets the end user compare profiles from different locations on the map. Figure 3.13 shows an example of a comparison of profiles from four locations on the map at 17:00 UT

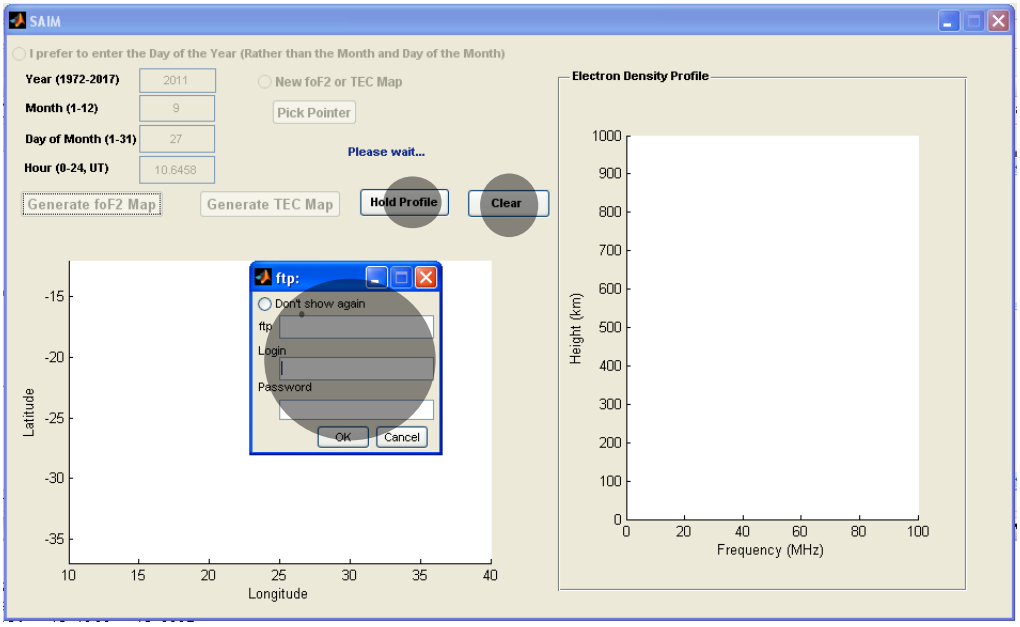

Figure 3.12: The new SAIM interface.

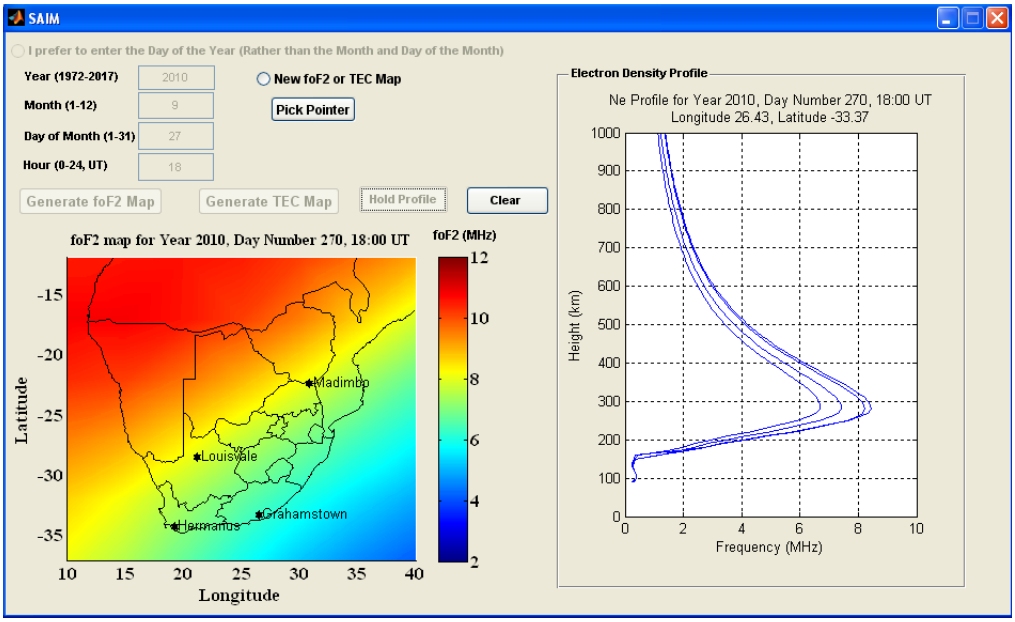

Figure 3.13: An example of a comparison of profiles from different locations on the map. Time: 17:00 UT, 2010-09-27.

(15:00, SAST). If new plots are needed for the same running time, the "clear" option is used to clear the axes.

3.8 Summary

This chapter discussed the improvements and validation of the new version of SAIM. The SAIM was updated with the Hermanus ionosonde data, the IRI-2012 model and the new version of the SABIM model. These updates have improved the performance of SAIM by 75 % over the previous version. The performance of the SABIM model was also validated for estimation of foF2 values over the South African region. The results show that the SABIM model outperforms the IRI-2012 model. In addition, the SABIM model was found to perform better during winter and solar minimum than during summer and solar maximum. In the next chapter the initial attempt to extend the development of the ionospheric map over the rest of Africa is discussed.

Chapter 4

Initial Attempt at Developing the AIM

4.1 Introduction

The initial attempt to develop the African Ionospheric Map (AIM) was based on the already existing SAIM. The data sources were the African ionosonde network, the IRI-2012 model and SABIM. This chapter discusses the process followed to obtain the initial AIM results that formed the basis of the improvement of the map's accuracy. The emphasis is on foF2, because it is the parameter of greatest interest in radio communication.

4.2 The African Ionosonde Network

The ionosonde network over the African region is sparsely and unevenly distributed with most stations located in the South as illustrated in figure 4.1. The green dots indicate stations that on average have been continuously active from 2008 to 2012 (see figure 3.1a for the period of

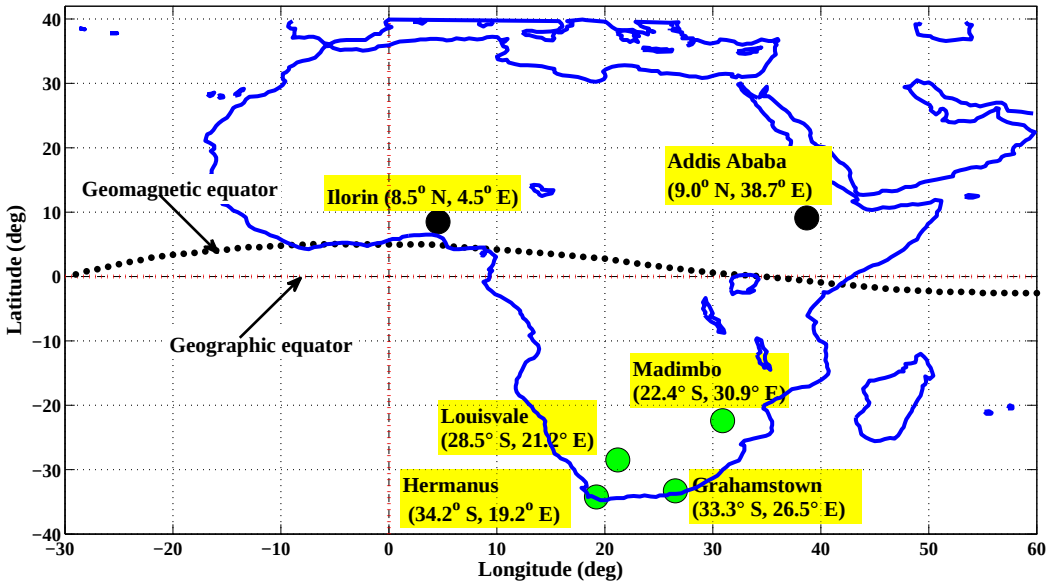

Figure 4.1: The African ionosonde network: the green dots indicate stations that on average have been continuously active throughout the past 4 years (2008-2012), while the black dots indicate either an upcoming ionosonde installation or a station with no readily available data due to technical problems.

operation of each station), while the black dots indicate either a planned ionosonde installation or a station with no readily available data due to technical problems.

In an attempt to overcome the challenge of the paucity of ionosondes, a symmetrical ionosphere about the geomagnetic equator was assumed. The ionosondes in the South were then reflected to the North using the geomagnetic equator as the "mirror line". This would take care of geomagnetic field secular changes which are reflected in the geographic position of the dip equator in different regions (Rangarajan and Barreto, 2012). The newly created points were each labelled with a prefix "R" and considered additional ionosonde stations as shown in figure 4.2.

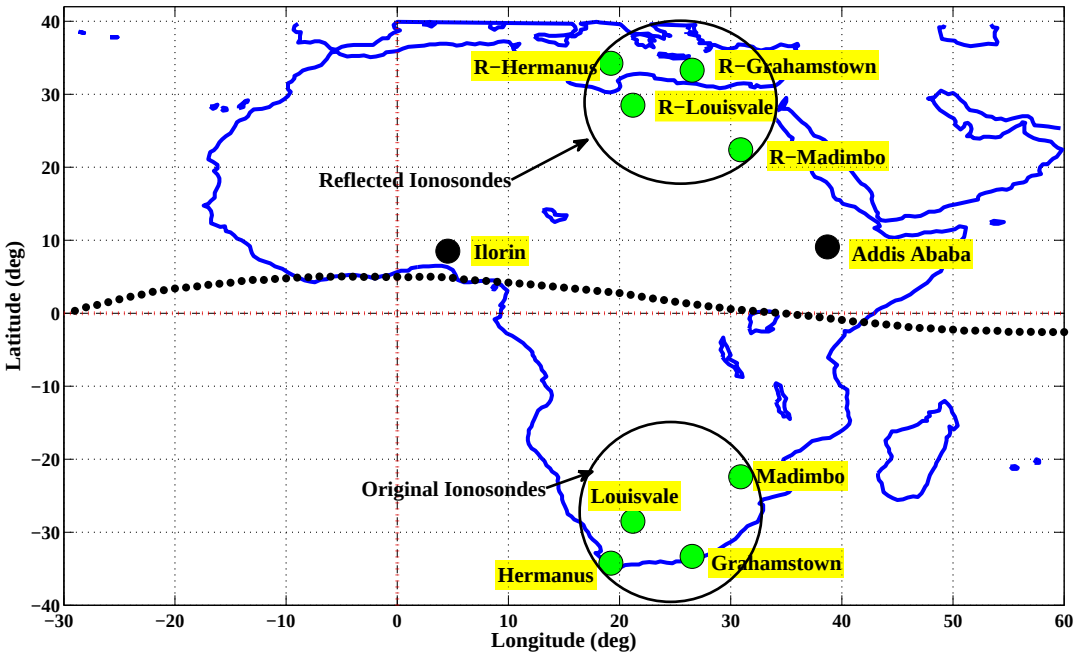

Figure 4.2: A map showing original and reflected ionosonde stations using the geomagnetic equator as the "mirror line". The reflected stations are labelled with a prefix "R".

4.3 Use of Ionosonde, SABIM and IRI-2012 Data in AIM

In SAIM the ionosonde measurements were used in such a way so as to not only affect the ionosonde locations, but also the whole South African region. A plane fit, in response to the varying degree of the differences between the ionosonde and model values at the ionosonde locations, was used to adapt the whole map to the true ionosonde measurements (Okoh, 2009). However, this technique could not be applied to the entire African region as a whole since part of the region lies within the low and equatorial latitudes. The ionosphere bound within these latitudes is characterised by low foF2 values in the equatorial trough and steep gradients in the rising part of the anomaly crests due to the fountain effect. Therefore, the African region was divided into three sections (as illustrated in figure 4.3): the south (20^o S - 40^o S, 30^o W - 60^o E), central (20^o N - 20^o S, 30^o W - 60^o E) and north (20^o N - 40^o N, 30^o W - 60^o E) and each dealt with separately.

The south section lies within the same region covered by SAIM but with an extended longitudinal coverage over the ocean areas. This section was modelled using the South African ionosonde network, the IRI-2012 model and SABIM as explained in chapter 3, but with an added modification, discussed below, to IRI-2012.

The IRI-2012 model offers two alternatives for the generation of the foF2 parameter, namely the International Radio Consultative Commit-

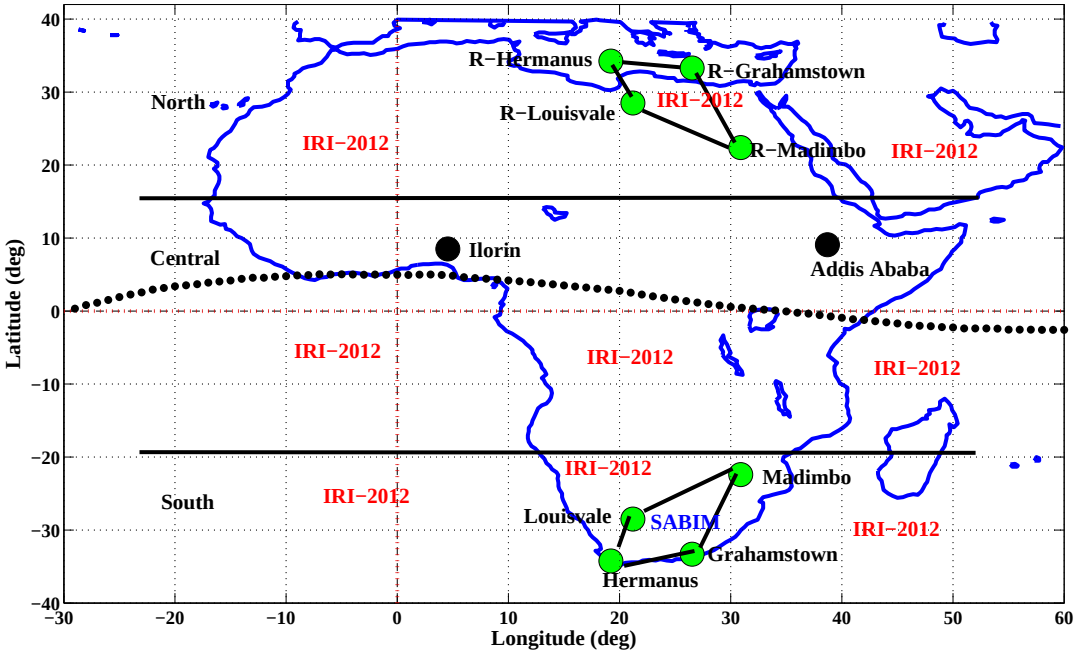

Figure 4.3: Application of the different data sources (ionosondes, SABIM and IRI-2012) in developing AIM.

tee (CCIR, 1966) model and the International Union of Radio Science (URSI) model developed by Rush et al. (1989). Both models use a similar spherical-harmonics-type representation of the monthly median diurnal variation of foF2 observed by the worldwide network of ionosondes, but with a different interpolation scheme for the ocean areas. Bilitza et al. (2011) and Adeniyi et al. (2003) mentioned that the CCIR model and the URSI model perform better over the continent and ocean areas respectively, and their application was such when modelling this section and the other areas of the map where the IRI-2012 model was applied.

The central section was modelled using the IRI-2012 model by generating data points at an interval of 5^o throughout.

The north section was modelled using the reflected ionosondes and the IRI-2012 model. The IRI-2012 model was used both inside and outside the quadrilateral area enclosed by the reflected ionosondes. A plane of best fit to the differences between the reflected ionosondes and model values at the ionosonde locations was used to adapt the quadrilateral area. This technique was limited to the quadrilateral area since the reflected ionosondes are not uniformly distributed throughout the northern section. Therefore, the use of the plane fit method throughout the section would introduce additional errors and increase the sensitivity of the results for those locations that are spatially distant from the ionosondes.

4.3.1 Plane Fitting to the Northern Quadrilateral Area

To formulate the equation of a plane, only 3 data points are required. In the case of the quadrilateral, 4 ionosonde station data points exit, but with the uncertainty that measurements from all 4 stations will always be available. The uncertainty arises from frequent technical problems at the stations, or other problems that may prevent data generation. For this reason, a different solution had to be formulated for each case, depending on the number of active ionosondes.

All 4 Ionosondes Available:

In this case, there are more equations than unknowns (system is over-determined) and so the least square minimisation method is used to fit

the best plane. The regression plane method is used during minimisation since the x (longitude) and y (latitude) values are fixed and the measured error (difference between ionosonde and model values) is in the z direction alone.

The Regression Plane Method

Given a set of 4 data points, $\{(x_i, y_i, z_i)\}_{i=1}^{4}$, three unknowns A, B and C need to be determined such that the plane, $z = Ax + By + C$, best fits the data points. This is obtained if the sum of squares of the errors, $\xi\,(A,\, B,\, C)$, between the plane and z_i is minimised.

$$\xi\,(A,\, B,\, C) = \left[(Ax_i + By_i + C) - z_i\right]^2 \tag{4.1}$$

At the minimum point, the gradient of $\xi\,(A,\, B,\, C)$ is equal to zero. That is,

$$\nabla\xi\,(A,\, B,\, C) = 2\sum_{i=1}^{i=4}\left[(Ax_i + By_i + C) - z_i\right](x_i,\, y_i,\, 1) = (0, 0, 0) \tag{4.2}$$

If equation 4.2 is reorganised and written in the form of a matrix,

$$\begin{bmatrix} \sum_{i=1}^{i=4} x_i^2 & \sum_{i=1}^{i=4} x_i y_i & \sum_{i=1}^{i=4} x_i \\ \sum_{i=1}^{i=4} x_i y_i & \sum_{i=1}^{i=4} y_i^2 & \sum_{i=1}^{i=4} y_i \\ \sum_{i=1}^{i=4} x_i & \sum_{i=1}^{i=4} y_i & \sum_{i=1}^{i=4} 1 \end{bmatrix} \begin{bmatrix} A \\ B \\ C \end{bmatrix} = \begin{bmatrix} \sum_{i=1}^{i=4} x_i z_i \\ \sum_{i=1}^{i=4} y_i z_i \\ \sum_{i=1}^{i=4} z_i \end{bmatrix} \tag{4.3}$$

a solution to the unknowns A, B and C can be determined and thereafter the required equation of the plane, $z = Ax + By + C$ (Eberly, 2000).

3 Ionosondes Available:

In this case three data points, (x_1,y_1,z_1), (x_2,y_2,z_2) and (x_3,y_3,z_3), are available with three unknowns A, B and C.

Using the general equation of a plane $Ax + By + Cz + d = 0$, four equations are formulated:

$$\begin{aligned} Ax_1 + By_1 + Cz_1 + d &= 0 \\ Ax_2 + By_2 + Cz_2 + d &= 0 \\ Ax_3 + By_3 + Cz_3 + d &= 0 \\ Ax + By + Cz + d &= 0 \end{aligned} \tag{4.4}$$

which can be written as a matrix:

$$\begin{pmatrix} x_1 & y_1 & z_1 & 1 \\ x_2 & y_2 & z_2 & 1 \\ x_3 & y_3 & z_3 & 1 \\ x & y & z & 1 \end{pmatrix} \begin{pmatrix} A \\ B \\ C \\ d \end{pmatrix} = \begin{pmatrix} 0 \\ 0 \\ 0 \\ 0 \end{pmatrix} \tag{4.5}$$

There is a non-trivial solution to this system of linear equations which is determined using the determinant method

$$det \begin{pmatrix} x_1 & y_1 & z_1 & 1 \\ x_2 & y_2 & z_2 & 1 \\ x_3 & y_3 & z_3 & 1 \\ x & y & z & 1 \end{pmatrix} = 0$$

From the solution the equation of the plane required can be determined.

2 Ionosondes Available

In this case, the 2 ionosonde points cannot define a unique plane, but would rather be part of any plane that is rotated around them. Thus, a third point (R) is chosen among the many infinite planes having the same longitude and z value as one of the two points. In addition, the line drawn from R must be perpendicular to the one joining the two ionosonde data points (Okoh, 2009). The equation of the plane is then obtained as in the 3-ionosonde case.

1 Ionosonde Available

In this case the z values of the other two points (to make three in total) is a duplicate of the z value at the available ionosonde station. The output or fitted plane is a plane of constant z values.

No Ionosonde Data Available

In this case the whole northern section is modelled by sing the IRI-2012 model.

4.4 Results

The three modelled sections (south, central and north) were combined to form one complete foF2 African map. At the edges, where the sections join, an overlap of 5^o smoothing was performed to reduce blocking artefacts. The map was interpolated to a resolution of 0.1 degrees using the triangular mesh interpolation method and the best surface was fit to the result. The final results were tested for portraying the basic background physics of the ionosphere, such as the diurnal, seasonal and solar cycle variations.

Diurnal: Figure 4.4 shows the variation of foF2 over the African sector using a 4-hour resolution starting 02:00 UT to 00:00 UT (the following day) in 2012. The intensity of the foF2 increases gradually from 02:00 UT, maximising at 10:00 UT and decreasing to low levels again during the night. This diurnal pattern is due to the plasma transportation processes in the F2-layer and the solar zenith angle dependence which peak at 00:00 UT and tends to a minimum at 10:00 UT.

At the equatorial magnetic latitudes where magnetic symmetry is nearly perfect, the latitude minimum of foF2 (in the trough) and the equatorial anomaly crests due to the fountain effect are also well-defined.

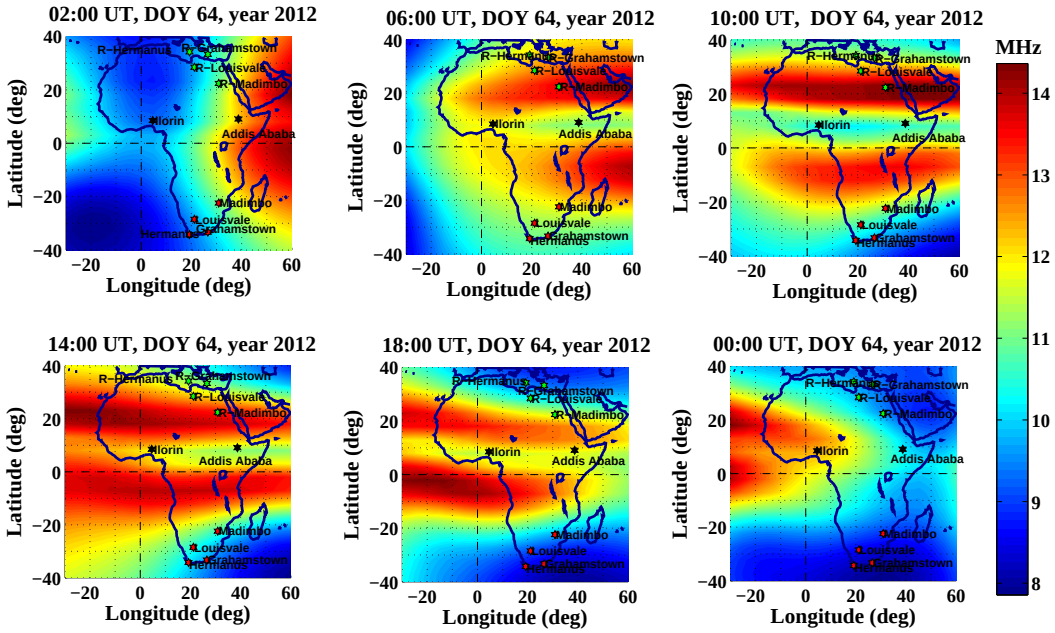

Figure 4.4: Diurnal variation of foF2 over the African region on day 64 of 2012.

Seasonal: Figure 4.5 illustrates maps generated for 10:00 UT on arbitrarily chosen days during the different seasons (summer (DOY 6), autumn (DOY 96), winter (DOY 187) and spring (DOY 279) in the year 2010. The maps depict the expected variation of the foF2 parameter, with the highest intensity during summer and the least during winter.

Solar cycle: Figure 4.6 shows three maps generated for 10:00 UT on an arbitrarily chosen day (DOY 6) of different years corresponding to different stages of the solar cycle. The maps show a trend in the foF2 intensity, highest during solar maximum (2000), moderate during the mid-solar cycle (2004) and lowest during solar minimum (2006). This trend is to be expected, since solar radiation decreases from solar maximum to solar minimum.

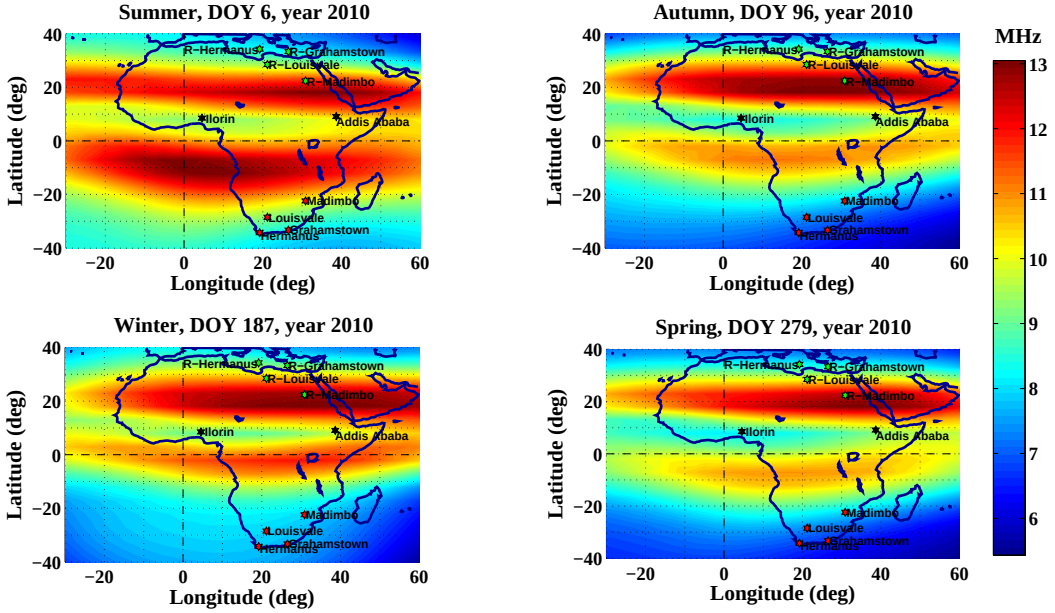

Figure 4.5: Seasonal variation at 10:00 UT of foF2 over the African region in 2010.

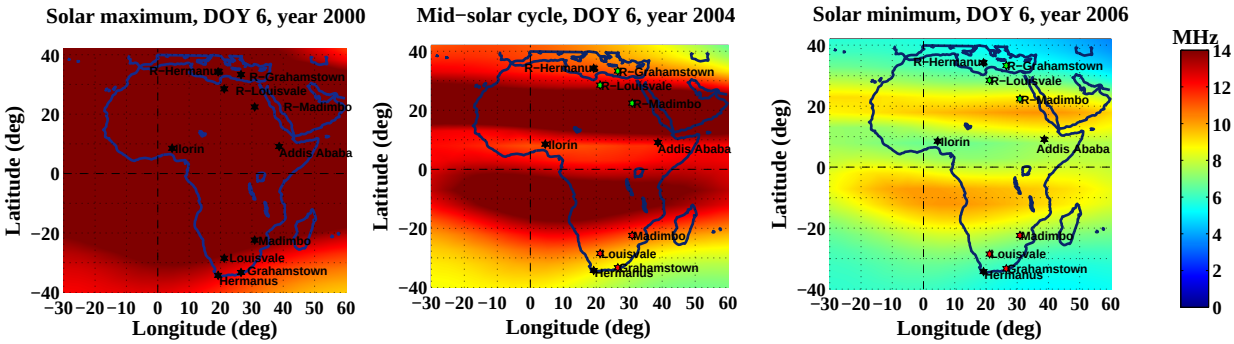

Figure 4.6: foF2 maps for 10:00 UT generated during the different stages of the solar cycle: solar maximum (2000), mid-solar cycle (2004) and solar minimum (2006).

4.4.1 Areas for Improvement

Although the generated maps did show the expected ionospheric variations, some areas of the map were identified as requiring improvement:

- In figure 4.4 mostly at 10:00 UT, the northern equatorial anomaly crest extends beyond the expected 20^o N mark.
- During the solar maximum of 2000 the ionosonde data was not included in the generation of the foF2 map (i.e. the map was generated using the IRI-2012 model and SABIM only). As a result, the map saturated, leading to a non-definable fountain effect at the equatorial region. Ouattara (2013) used the IRI-2007 to predict foF2 at Ouagadougou (12^o N, 1.8^o W) ionosonde station, during the quiet time periods from 1985 to 1995. The study revealed that the accuracy of the IRI-2007 model was best during the solar minimum phase and the worst during the solar decreasing phase. In addition, during solar maximum and decreasing phases, the IRI-2007 model did not express the signature of the fountain effect (E $\times$ B) for the African equatorial sector.

To overcome these challenges and improve the map's accuracy, data points from another data source would need to be included in the AIM.

4.5 Summary

This chapter described the initial attempt to develop the AIM using available resources and focusing on the ionospheric parameter foF2. The results show that the basic background physics of the ionosphere is depicted in the generated maps. However, some areas require improvement, particularly within the equatorial anomaly region where ionospheric observations are insufficient or lacking. The next chapter discusses a statistical method for estimating foF2 from GPS TEC, to be applied in regions of Africa without ionosondes to improve the map's accuracy.

Chapter 5

Extraction of foF2 From GPS TEC (TEC2F2)

5.1 Introduction

Ionospheric variability is commonly studied using measurements from ground-based ionosondes. Although ionosondes are known to be the most accurate available resource for measuring ionospheric parameters, the use of ionosondes is limited to measurements of the bottomside ionosphere. Ionosondes are also fairly expensive to install and therefore lacking in parts of the world (e.g. Africa) where resources are scarce. Therefore, there is a long-recognised need for alternate methods of deriving ionospheric information. One such method is the derivation of TEC from GPS receiver data. GPS receivers are low-cost instruments compared to ionosondes and other radars. They are easy to maintain and provide continuous measurements along a path that passes through the ionosphere, thus being the ideal candidates for ionospheric research in places like Africa.

Efforts have been made to estimate the F2 layer critical frequency (foF2) as a representation of the maximum electron density from GPS data or TEC. For example, Spalla and Cairolo (1994) suggested a simple model ($(foF2)^2 = 3.51$ TEC) which provides a coarse estimation of foF2 median values based on knowledge of TEC. Houminer and Soicher (1996) predicted foF2 values from GPS phase delays and suggested a possibility of using real-time TEC measurements to update the foF2 values.

This chapter discusses a new method (hereafter referred to as TEC2F2) to derive ionospheric foF2 information from GPS Vertical TEC (VTEC) over the African region using polynomials (Ssessanga et al., In-press). The method is based on the high correlation (usually greater than 0.80) that exists between VTEC and foF2 (Kouris et al., 2004). The results obtained are compared to the International Reference Ionosphere (IRI-2012) model and to the measured values recorded by the African ionosondes for validation purposes.

The aim of developing the TEC2F2 method is to establish an accurate method for estimating the foF2 parameter over the African region, especially in areas without ionosondes.

5.2 TEC2F2 Development Over South Africa

The process of estimating foF2 from VTEC was first considered for the South African region. This region is covered by a network of ionosondes that can provide a validation platform for the TEC2F2 method before being applied to other parts of Africa.

Table 5.1: Ionosondes and the closest GPS receivers which provide foF2 and TEC data respectively. At Hermanus and Grahamstown the ionosonde and GPS stations are co-located.

Ionosonde/ GPS station	Location	Code
Hermanus	34.4° S, 19.2° E	HE13N (ionosonde), HNUS (GPS)
Grahamstown	33.3° S, 22.4° E	GR13L (ionosonde), GRHM (GPS)
Louisvale	28.5° S, 21.2° E	LV12P (ionosonde)
Upington	28.4° S, 21.2° E	UPTA (GPS)
Madimbo	22.4° S, 30.9° E	MU12K (ionosonde)
Thohoyadou	23.0° S, 30.4° E	TDOU (GPS)

foF2 and ionosonde data from respectively four ionosondes and the corresponding dual frequency (L_1, L_2) GPS receivers (with a sampling period of 1 second) located in proximity were used. Table 5.1 lists the ionosondes and the respective GPS receivers used for this study.

The ionosonde data with a sampling period of 15 minutes are archived at SANSA and can also be downloaded from the SPIDR database (`http://spidr.ngdc.noaa.gov/spidr/`). GPS data is available (in either 1 or 30 sec intervals) from the TrigNet database (`http://www.trignet.co.za/`).

TrigNet is a network of permanent continuously operating GNSS base stations distributed throughout South Africa at distances approximately 100 km to 300 km apart. All stations record 1 second epoch data on both frequencies L_1 and L_2. Data from all stations is continuously streamed to the TrigNet control centre in the office of the Chief Directorate: National Geospatial Information from where it is made available

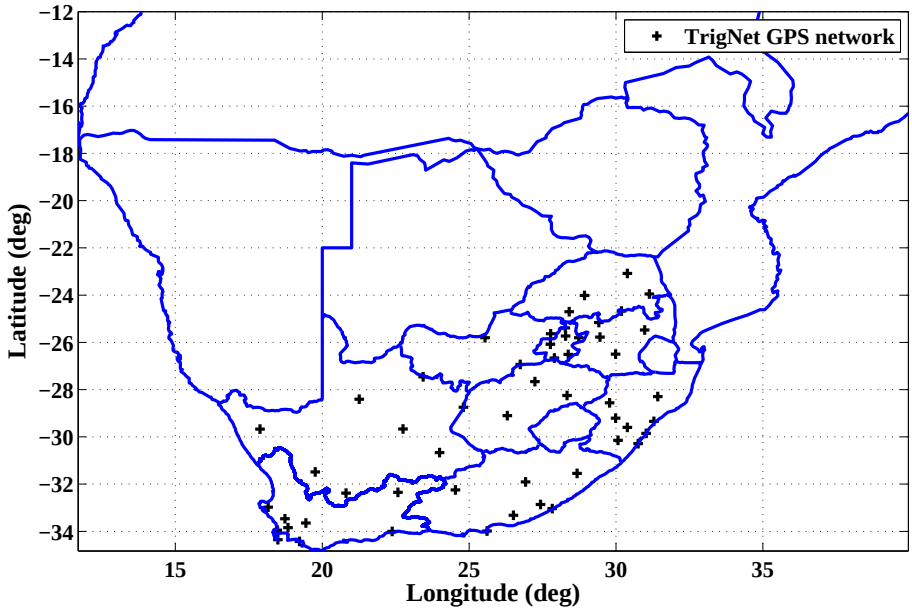

Figure 5.1: TrigNet stations across South Africa.

in RINEX (Receiver INdependent EXchange) format. Figure 5.1 shows the network of TrigNet stations across South Africa.

The data collected from the ionosonde and corresponding GPS receivers covers a period of 7 years from 2006 to 2012. This database covers all available data and includes the solar minimum and the approach to solar maximum.

5.2.1 GPS VTEC Processing

The VTEC values were derived from GPS observables using the Rinex GPS-TEC program Version 1.45 developed at Boston College (Seemala and Valladares, 2011). The program uses both L_1 and L_2 to calculate the relative STEC by removing errors due to clock biases and the tropospheric water vapour effect (Sardón and Zarraoa, 1997). To obtain the absolute TEC values, the differential satellite biases (publi-

shed by the University of Bern) are included along with the receiver bias values that are calculated by minimizing the TEC variability between 02:00 and 06:00 local time (Doherty et al., 2004). The equivalent vertical TEC at an Ionospheric Pierce Point (IPP) altitude of 350 km is calculated assuming the thin shell model (Coco et al., 1991; Wilson and Mannucci, 1993; Ciraolo and Spalla, 1997). The vertical TEC over a particular station is computed by averaging the TEC for individual satellites in view (Habarulema et al., 2013).

5.2.2 Data Analysis

The diurnal ionosonde foF2 data (at temporal resolution of 15 minutes) was interpolated using a cubic spline interpolation method to produce the same sample size as the VTEC data (which was derived at 6 minute intervals). The resulting foF2 and VTEC values were smoothed by using a running mean method with a span of 3 hours. This was done to reduce the noise in the data which may be due to measurement errors and data reduction processes (Houminer and Soicher, 1996).

The smoothed daily ionosonde foF2 values were correlated with the daily smoothed VTEC values of the co-located or nearest GPS receivers. On average the result was a "hysteresis loop" structure with a correlation coefficient (R) of more than 0.8. Figure 5.2 shows an example of a "hysteresis loop" over the Grahamstown station on an arbitrarily chosen day (6 February 2006). The R value was 0.98.

This "hysteresis loop" phenomenon is due to the diurnal variation of foF2 and TEC, which is a result of strong photo-ionisation during the

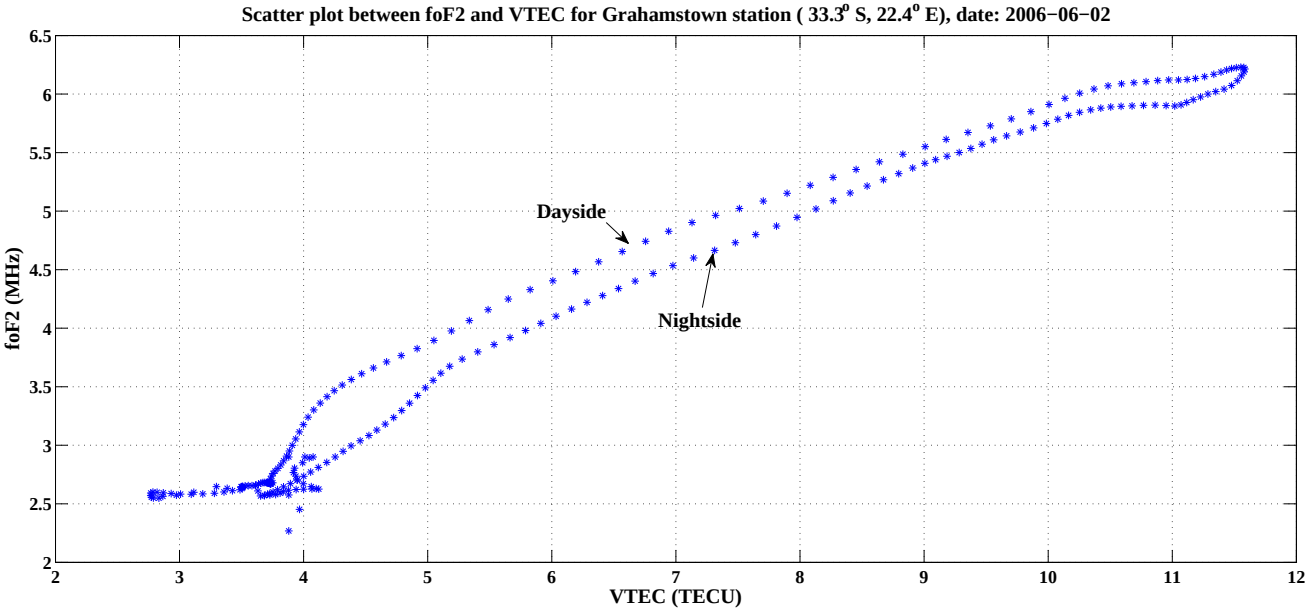

Figure 5.2: Scatter plot of daily foF2 and VTEC values for Grahamstown station on 6 February 2006. The "Hysteresis Loop" structure is a result of the dominance of ionospheric ionisation during the day and recombination during the night.

day and recombination of ions and electrons during the night (Kouris et al., 2004).

Based on the value of R, the data was filtered, with days corresponding to R less than 0.5 exempted from the analysis. This threshold was chosen based on a statistical analysis that on average most days showed an R value above 0.7. Days when R was less than 0.5 had a Kp greater than 4 (disturbed days) and, therefore, were not used in this analysis.

The filtered data was then grouped according to months and years, to reflect the relatively large ionospheric seasonal changes from one month to the next in a year. The foF2 and VTEC values were correlated on an individual hour-to-hour basis for each month and the R value corresponding to each hour determined. Figure 5.3 shows an example of the monthly variation of R using foF2 values from the Hermanus

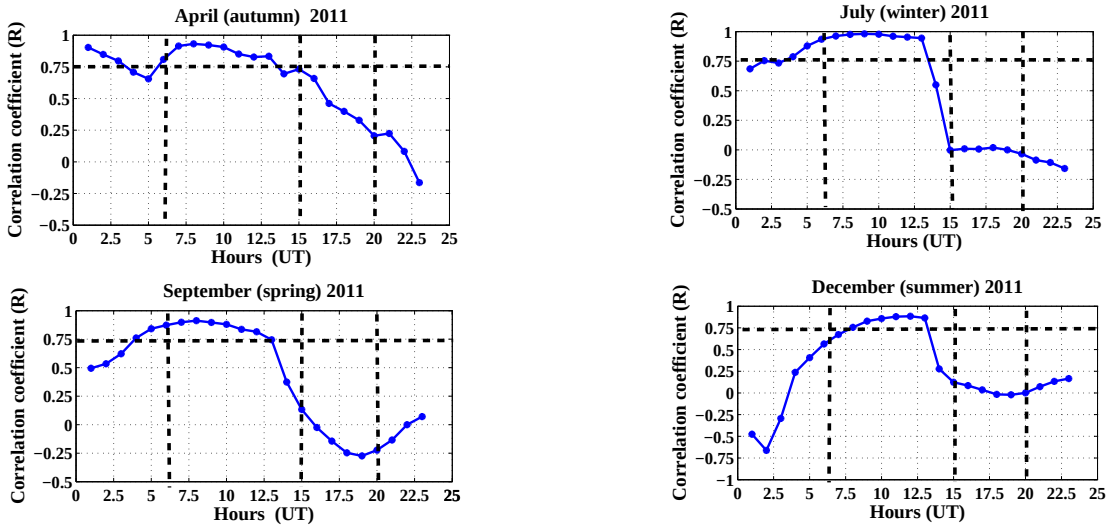

Figure 5.3: An example of the monthly variation of the correlation coefficient (R) of foF2 and VTEC values at Hermanus for different months in 2011. The months were chosen to reflect the seasons (autumn, winter, spring and summer). An R value above 0.7 is seen to occur during 06:00 - 15:00 UT and R below 0.5 during 20:00 - 23:00 UT.

ionosonde and VTEC values from the Hermanus GPS receiver. The months represented here were chosen to reflect the seasons of the year in the southern hemisphere; April (autumn), July (winter), September (spring) and December (summer) of 2011. The result showed that on average foF2 and VTEC had the greatest correlation of between 0.7 and 1 during the hours 06:00 - 15:00 UT, and the least correlation (R<0.5) between 20:00 - 23:00 UT. These results were later used in the regression analysis.

5.2.3 Regression Analysis

Using the results of the previous procedure, the daily foF2 and VTEC data were divided into four sections; 00:00 - 05:59 UT, 06:00 - 14:59 UT, 15:00 - 19:59 UT and 20:00 - 23:59 UT, as shown in figure 5.4.

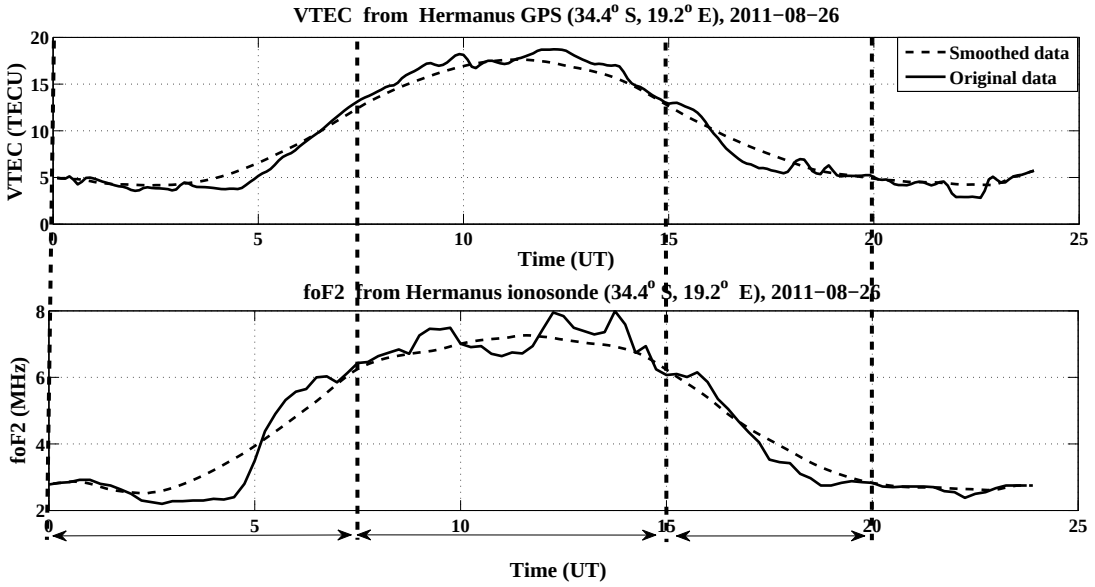

Figure 5.4: An example of the division of daily foF2 and VTEC values from the Hermanus ionosonde and GPS receiver respectively. The data is divided into four sections; 00:00 - 05:59 UT, 06:00 - 14:59 UT, 15:00 - 19:59 UT and 20:00 - 23:59 UT based on the monthly variation of R with time shown in figure 5.3.

For each section the scatter between the foF2 and TEC values was plotted for each day of the month through out each year in the data set. To each scatter plot, different polynomial functions (f(x)),

$$\mathrm{f(x)} = \sum_{i=1}^{N} \mathrm{p}i\mathrm{x}^{N-i}, \tag{5.1}$$

of different degrees, N-1, N = 2, 3, 4, 5 were fitted, as shown in figure 5.5, where f(x) represents the derived foF2 values in MHz, x the GPS VTEC values in TECU and pi the polynomial coefficients. For each fit the polynomial coefficients, R-squared (R2) and RMSE values were determined within a confidence interval of 95 %. Where

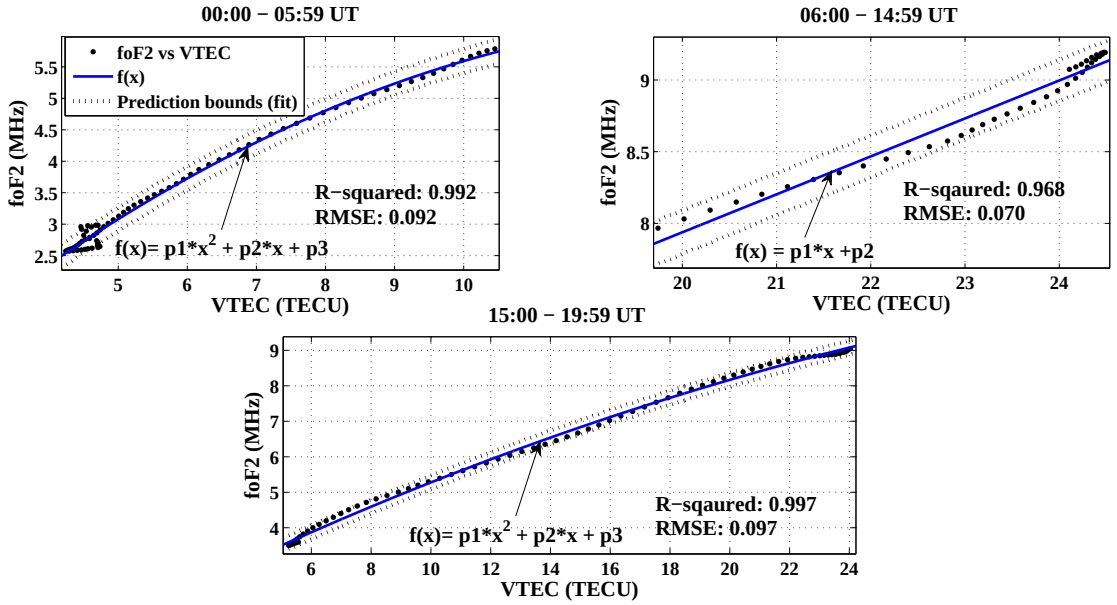

Figure 5.5: Polynomial fit to different parts of the "Hysteresis loop". The loop split was based on the daily variation of R shown in figure 5.3.

$$R2 = 1 - \frac{\sum_j^n \left(foF2_j - f(x)_j\right)^2}{\sum_j^n \left(foF2_j - \bar{foF2}\right)}, \tag{5.2}$$

$$\bar{foF2} = \frac{1}{n}\sum_j^n foF2_j$$

$$RMSE = \sqrt{\frac{\sum_j^n \left(foF2_j - f(x)_j\right)^2}{n}}, \tag{5.3}$$

n is the total number of measured foF2 values and j = 1, 2, 3, . . . , n.

The polynomial coefficients corresponding to the fit that provided the best R2 values and the least RMSE value were chosen to be used in building the model for that given month of the year. This process was repeated for all four ionosonde stations (listed in table 5.1) and the

Table 5.2: TEC2F2 averaged polynomial coefficients for every month of the year.

Month	00:00 - 05:59 UT				06:00 - 14:59 UT		15:00 - 19:59 UT	
	p1	p2	p3	p4	p1	p2	p1	p2
Jan	-9.016e-006	-1894e-006	0.332	1.206	0.238	2.497	0.299	1.699
Feb	-1492e-006	33360e-006	24760.0e-06	2.890	0.238	2.497	0.216	2.878
Mar	18.81e-006	-11690e-006	0.508	0.912	0.303	1.441	0.281	2.001
Apr	391.5e-006	-17370e-006	0.524	1.442	0.265	2.643	0.297	2.180
May	2832e-006	-88690e-006	1.291	-1.31	0.195	3.772	0.442	0.731
June	-20170e-006	0.318	-1.016	3.149	0.194	3.572	0.489	0.897
July	502500e-006	1.373			0.166	4.209	0.492	1.358
Aug	5343e-006	-0.173	1.953	-2.250	0.224	3.096	0.367	1.603
Sept	-8958e-006	0.227	-1.530	6.580	0.277	2.140	0.335	1.682
Oct	433.9e-006	-22910e-06	0.656	0.170	0.263	2.321	0.230	2.505
Nov	-856.9e-006	23810e-06	24160.0e-06	2.540	0.227	1.626	0.205	2.757
Dec	247.1e-006	-10810e-06	0.358	1.869	0.347	-0.432	0.201	3.410

coefficients averaged for use in the model for that section of the day in a given month of the year over the South African region (Ssessanga et al., In-press). Table 5.2 gives the averaged polynomial coefficients for the 12 months of the year.

For each month of the year, the different model coefficients from each time segment were put together to form one complete model for the whole day with the exception of the hours between 20:00 - 23:59 UT. Figure 5.6 shows scatter plots of foF2 against VTEC for the time segment 20:00 - 23:59 UT over the Grahamstown station during an arbitrarily chosen period of days (DOY 101 - 110) in 2006. The plots show that VTEC and foF2 do not have a consistent relationship. Because of this inconsistency, this segment (20:00 - 23:59 UT) was not modelled, hence not represented in the TEC2F2 model.

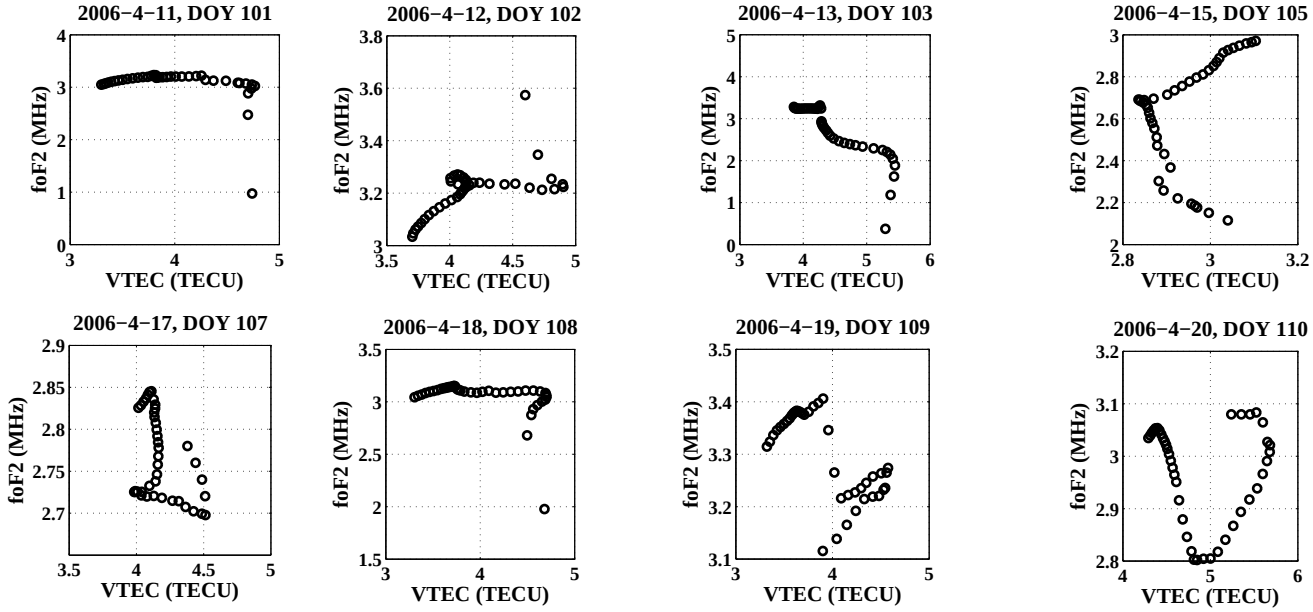

Figure 5.6: 20:00 - 23:59 UT scatter plots of Grahamstown ionosonde foF2 values and VTEC values from the co-located GPS receiver for an arbitrarily chosen continuous period of 8 days during 2006. The results show no consistent pattern between foF2 and VTEC values during this time of the night, which makes this segment difficult to model.

5.2.4 Results and Discussion

To test the performance of the TEC2F2 model, VTEC data from all four GPS receiver stations listed in table 5.1 was used to estimate the foF2 values. The results were then compared to the ionosonde data and the IRI-2012 model. This was done for the daily, seasonal and solar cycle variations. Most of the results presented here are from the year 2010 which had the most continuous data throughout the data set.

5.2.4.1 Diurnal Variation

Figure 5.7 shows an hourly comparison of measured ionosonde, TEC2F2 model and IRI-2012 model foF2 values over Grahamstown where the ionosonde and GPS receivers are co-located. The days were chosen around the equinox in March and solstice in June 2010. It can be observed that the TEC2F2 model performs better than the IRI-2012 model when estimating the peak daily foF2 values both during equinox (figure 5.7a) and solstice (figure 5.7b). The IRI-2012 model underestimates and overestimates the peak foF2 values during equinox and solstice periods respectively. These inaccuracies by the IRI-2012 model for the South African region have been pointed out by other groups. For example, McKinnell (2003) and Okoh et al. (2010) have developed models; the South African bottomside Ionospheric Model (SABIM) model and South African Ionospheric Map (SAIM) respectively, to more accurately predict the foF2 parameter based on the availability of the ionosonde data.

A correlation of the daily measured foF2 values from the four ionosonde stations and the two models, TEC2F2 and IRI-2012, was done for the 7-year period and the R2 and RMSE values calculated. Table

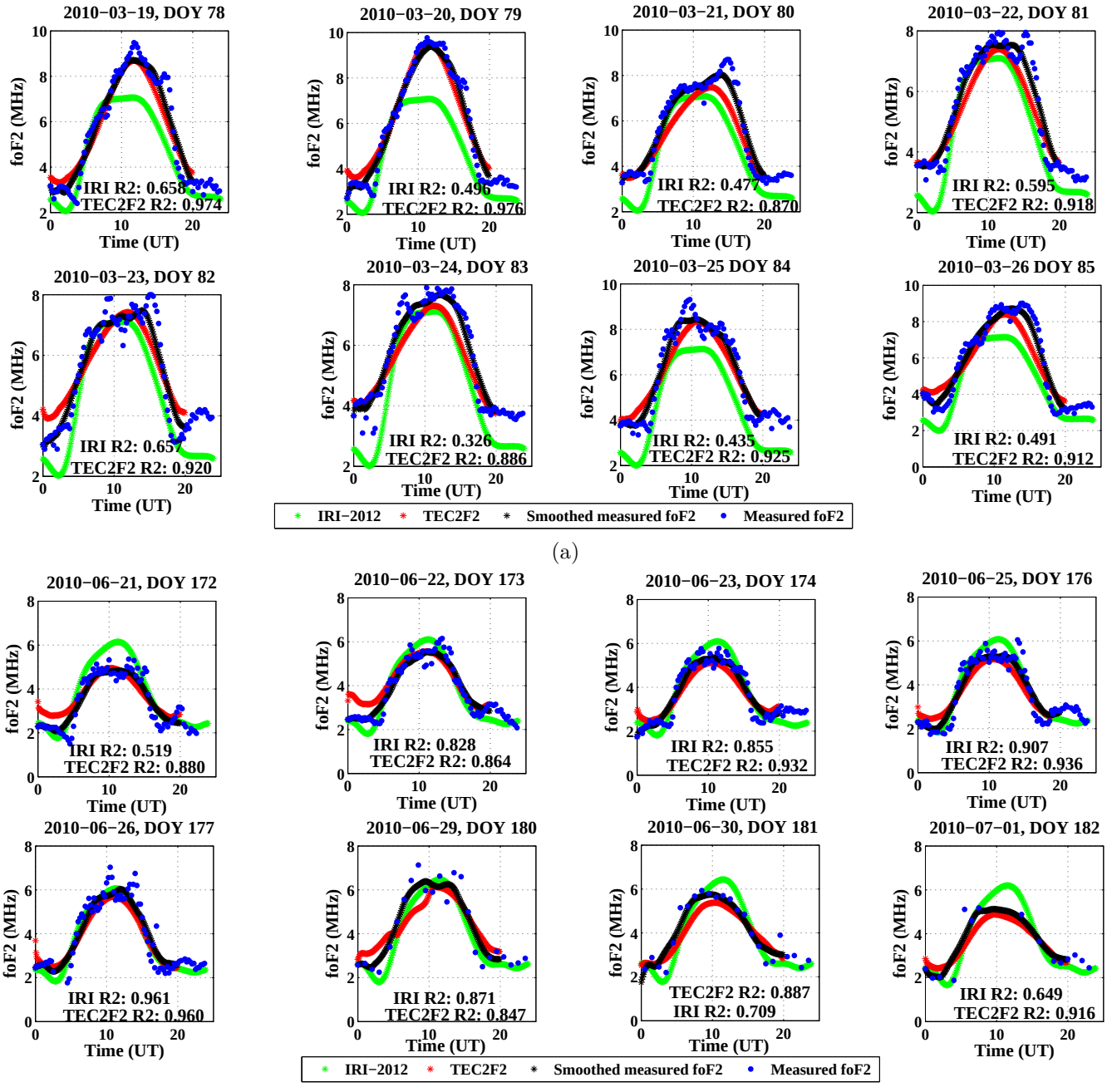

Figure 5.7: A comparison of hourly variation of foF2 values estimated by TEC2F2 and IRI-2012, and the measured data from the Grahamstown ionosonde station during equinox in March (figure 5.7a) and solstice in June (figure 5.7b) for the year 2010. The TEC2F2 model shows a better estimation of the peak foF2 values than the IRI-2012 model both during equinox and solstice.

Table 5.3: Root Mean Square Error (RMSE) and R-squared (R2) values for measured and TEC2F2 and IRI-2012 model predicted values for years 2006 to 2012.

Year	RMSE (MHz)		R2	
	TEC2F2	IRI-2012	TEC2F2	IRI-2012
2006	0.548	0.701	0.789	0.646
2007	0.683	0.651	0.596	0.472
2008	0.691	0.801	0.647	0.466
2009	0.699	0.725	0.637	0.527
2010	0.631	0.846	0.770	0.604
2011	1.000	1.324	0.713	0.453
2012	0.909	0.983	0.713	0.594
Average	0.732	0.861	0.695	0.537

5.3 provides the summary of the results. TEC2F2 gave an average R2 value of 0.69 and an RMSE of 0.73 MHz, where as the IRI-2012 gave an average R2 value of 0.54 and an RMSE of 0.86 MHz. Thus on average, the TEC2F2 value for foF2 estimation is 15 % better than the IRI-2012 model estimation. This also true for the work done by Okoh et al. (2010). However, it should be pointed out that the aim of developing the TEC2F2 model was not to improve SABIM or SAIM, but to complement the two models by using the GPS data, and ultimately extending this method to the rest of Africa where there are no ionosondes.

5.2.4.2 Annual and Seasonal Variation

Figure 5.8 shows ionosonde, TEC2F2 model and IRI-2012 model values of foF2 over the four ionosonde stations at local sunrise (02:00 UT), noon (10:00 UT) and after sunset (18:00 UT) in 2010.

The IRI-2012 model underestimates the foF2 values at all stations as compared to the measured values, especially before sunrise (figure 5.8a) and after sunset (figure 5.8c).

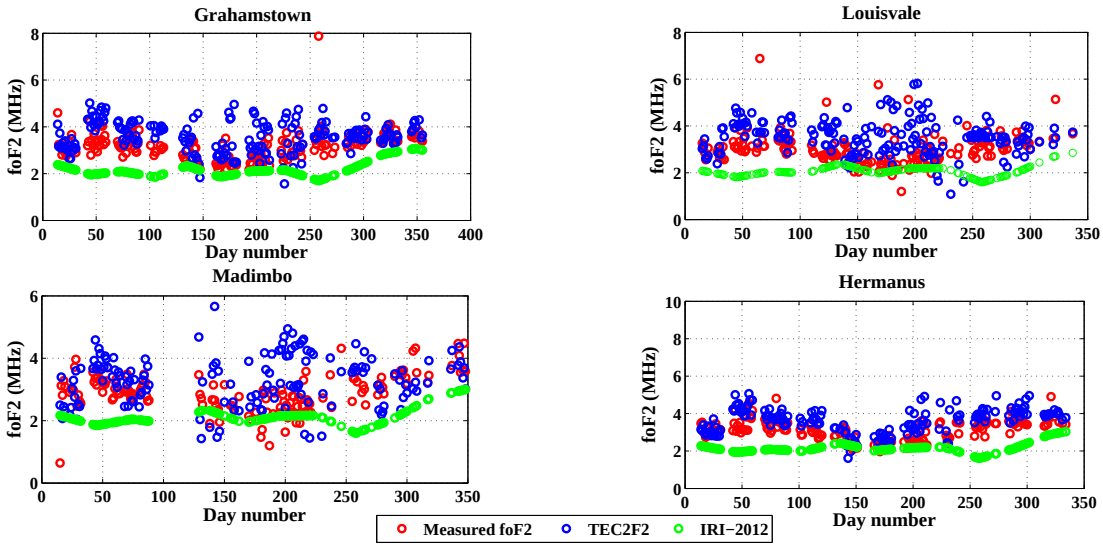

(a)

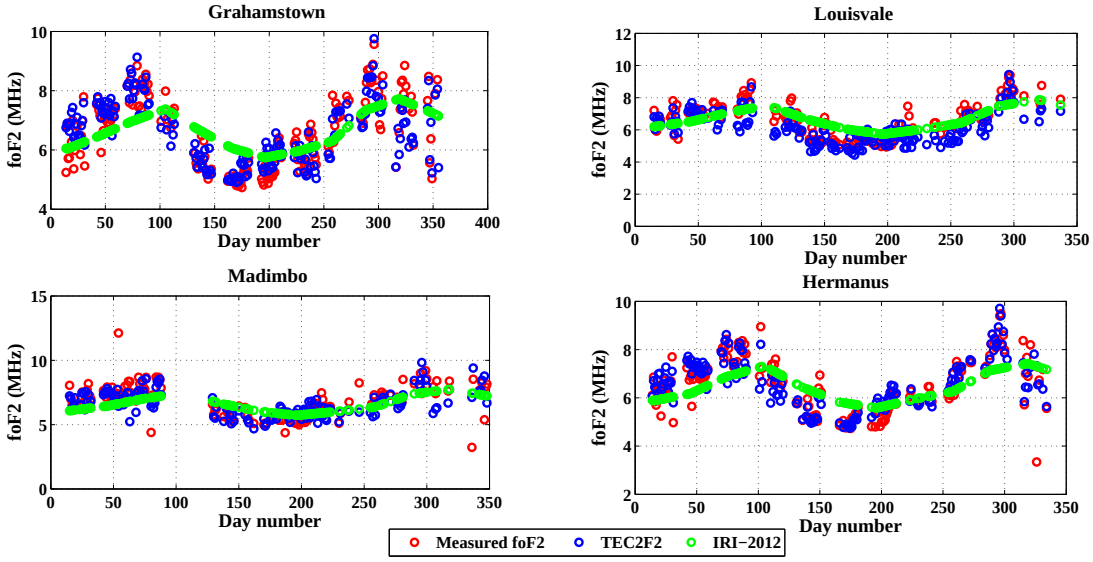

(b)

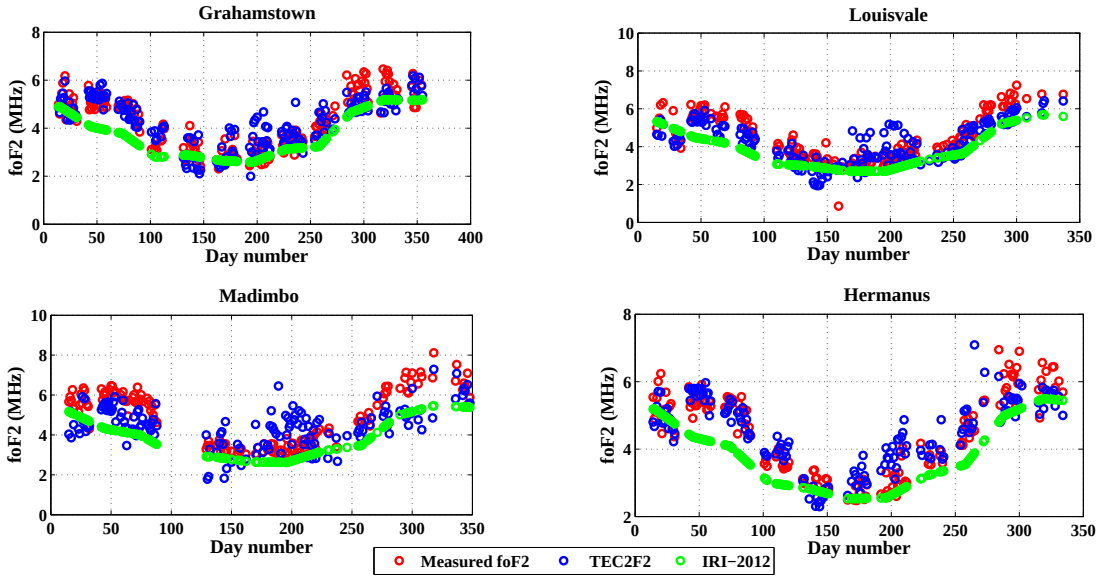

(c)

Figure 5.8: Variation of foF2 values estimated by TEC2F2 and IRI-2012, and measured data from the four ionosonde stations: Hermanus, Grahamstown, Louisvale and Madimbo. The times chosen are the: (a) before sunrise (02:00 UT), (b) local noon (10:00 UT) and (c) after sunset (18:00 UT), for the year 2010.

At local midday seasonal changes are well-defined (see figure 5.8b). A comparison between TEC2F2 model and the IRI-2012 shows that TEC2F2 estimates the foF2 parameter more accurately during all seasons (autumn, winter, spring and summer). This is well pronounced, especially at the Grahamstown and Hermanus stations. To confirm this result a further analysis of the 10:00 UT results was done.

In figure 5.9 the difference between the IRI-2012, TEC2F2 and the measured foF2 values was determined and the RMSE calculated at all four ionosonde locations. The residues for all four stations indicate that the TEC2F2 model estimates the 10:00 UT foF2 values better than the IRI-2012 model annually. On average, TEC2F2 had an RMSE value of 0.51 MHz, compared to the IRI-2012 RMSE of 0.70 MHz. Results obtained from the Grahamstown and Hermanus locations showed a better fit to the data, with RMSE values below 0.4 MHz, compared to Madimbo and Louisvale where RMSE values above 0.6 MHz were obtained.

Using data from all four ionosonde stations, scatter plots, as shown in figure 5.10, were drawn to illustrate the fit between the measured foF2 values and the two models. A line of best least squares linear fit (y) was inserted to demonstrate the relationship between the measured and estimated foF2 values. The results in figure 5.10 show that TEC2F2 provides a better correlation with the measured values compared to the IRI-2012 model. The TEC2F2 model produced high R2 values (above 0.8) for Grahamstown and Hermanus and lower R2 values for Louisvale (R2 = 0.59) and Madimbo (R2 = 0.48).

This inconsistency was more pronounced at Madimbo than at the other stations and was attributed to the distance between the ionosonde

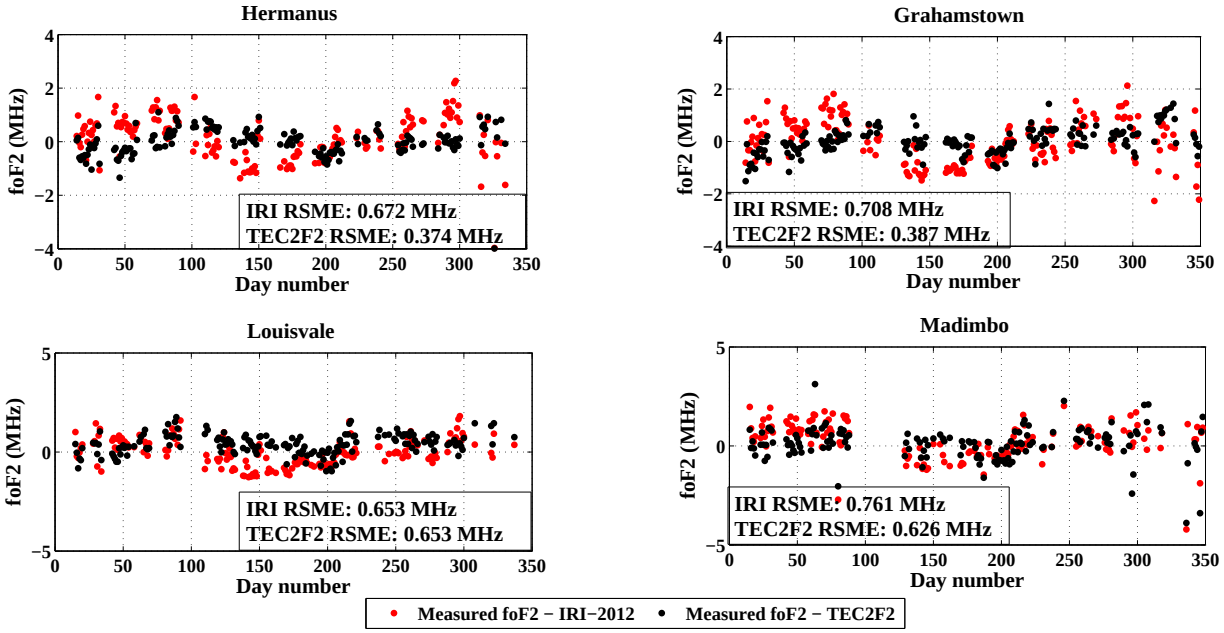

Figure 5.9: Residues of 10:00 UT measured foF2 values from ionosonde stations Hermanus, Grahamstown, Louisvale and Madimbo and models (IRI-2012 and TEC2F2).

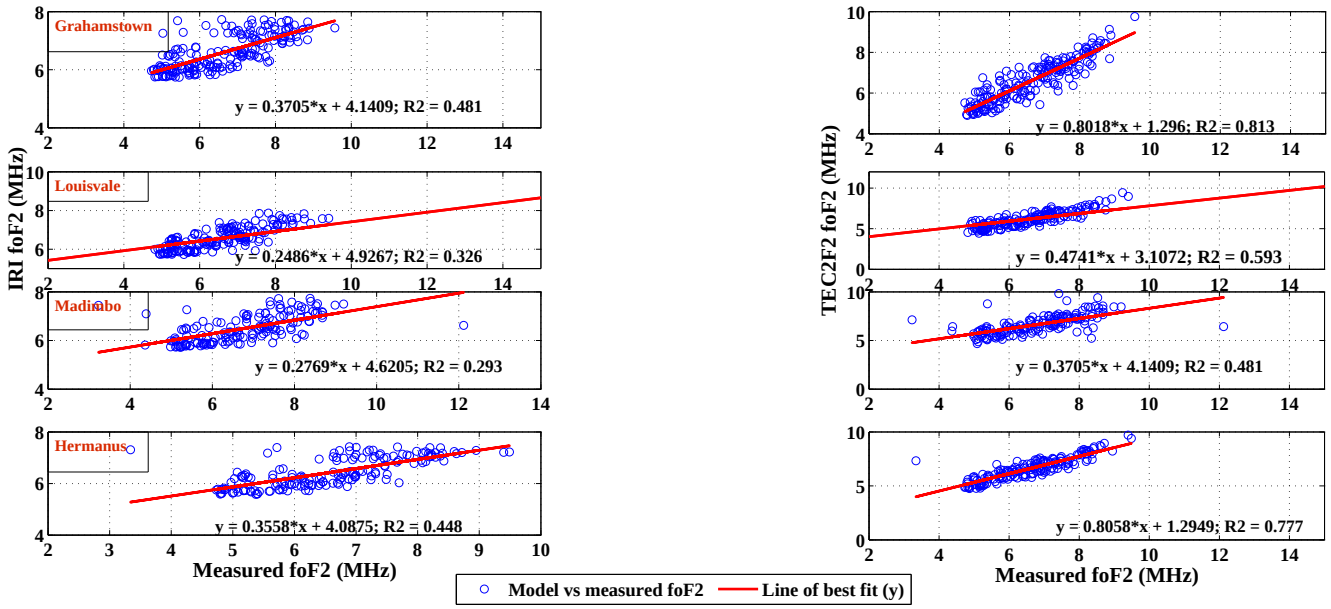

Figure 5.10: Scatter plots of measured foF2 values at 10:00 UT from the four ionosonde stations and the two models IRI-2012 (left) and TEC2F2 (right) for the year 2010.

and the closest GPS receiver (Thohoyandou). The distance between the two is approximately 130 km. Thus, it is important to note that the accuracy of the TEC2F2 model to estimate foF2 values from GPS VTEC at a particular location decreases with increasing distance between the point of interest and the closest GPS station chosen. Nevertheless, the results still show that TEC2F2 estimation is more accurate than estimation by the IRI-2012 model.

5.2.4.3 Solar Cycle Variation

Due to the paucity of GPS data compared to ionosonde data, and the lack of a complete solar cycle of GPS data, the validation of the TEC2F2 model over a solar cycle was constrained to a few years when data from both instrumentation networks were available. For the validation two locations were selected. These were Grahamstown and Louisvale. They were chosen for the availability of both appropriate ionosonde data and GPS data from the nearest GPS stations, Grahamstown and Upington, that coincided with the years required. The years 2006 and 2012 were selected to represent solar minimum and approach to solar maximum respectively. A solar maximum year of data from all appropriate stations was not available and so 2012 was chosen as the nearest to solar maximum for which data was available.

Figure 5.11 shows the variation of 10:00 UT foF2 values from IRI-2012, TEC2F2 and the two ionosonde stations. The upper and lower panels represent solar minimum (2006) and approach to solar maximum (2012) periods respectively. Residues of the two models and the measured foF2 are shown in figure 5.12. The TEC2F2 model shows a better estimation of the foF2 values during solar minimum than during solar

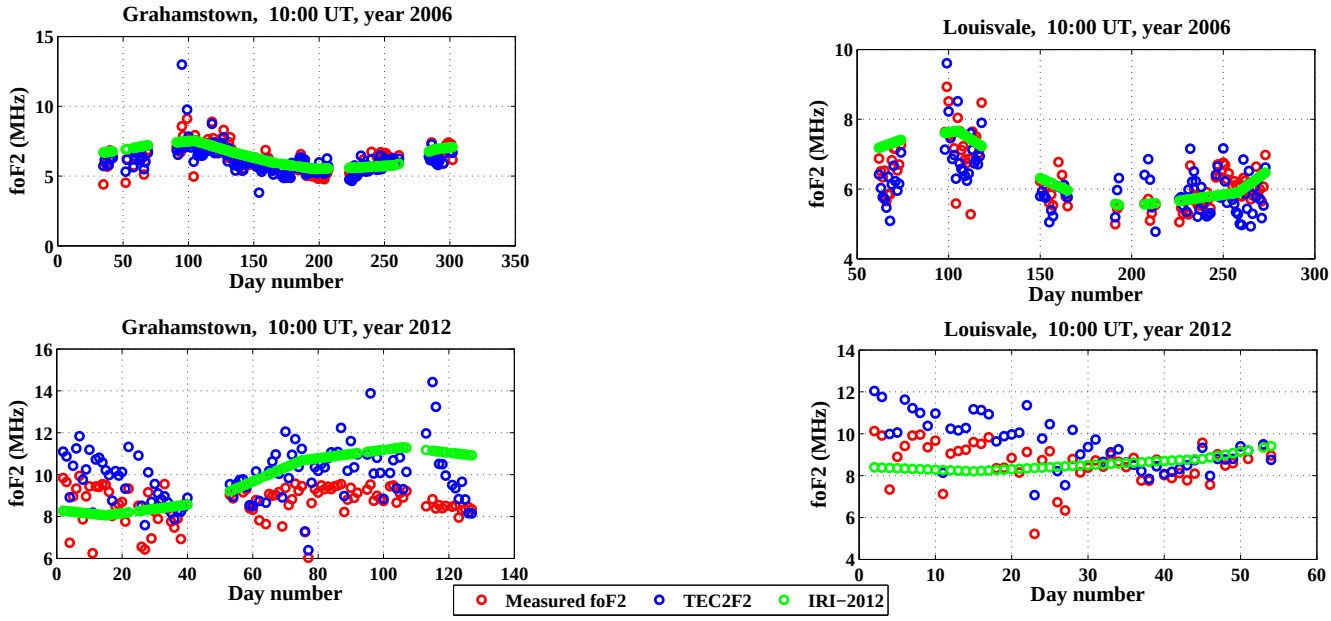

Figure 5.11: Variation of 10:00 UT foF2 values corresponding to solar minimum (2006) and approach to solar maximum (2012) at two ionosonde locations, Grahamstown and Louisvale. The TEC2F2 shows a better estimation of foF2 values during solar minimum than during solar maximum.

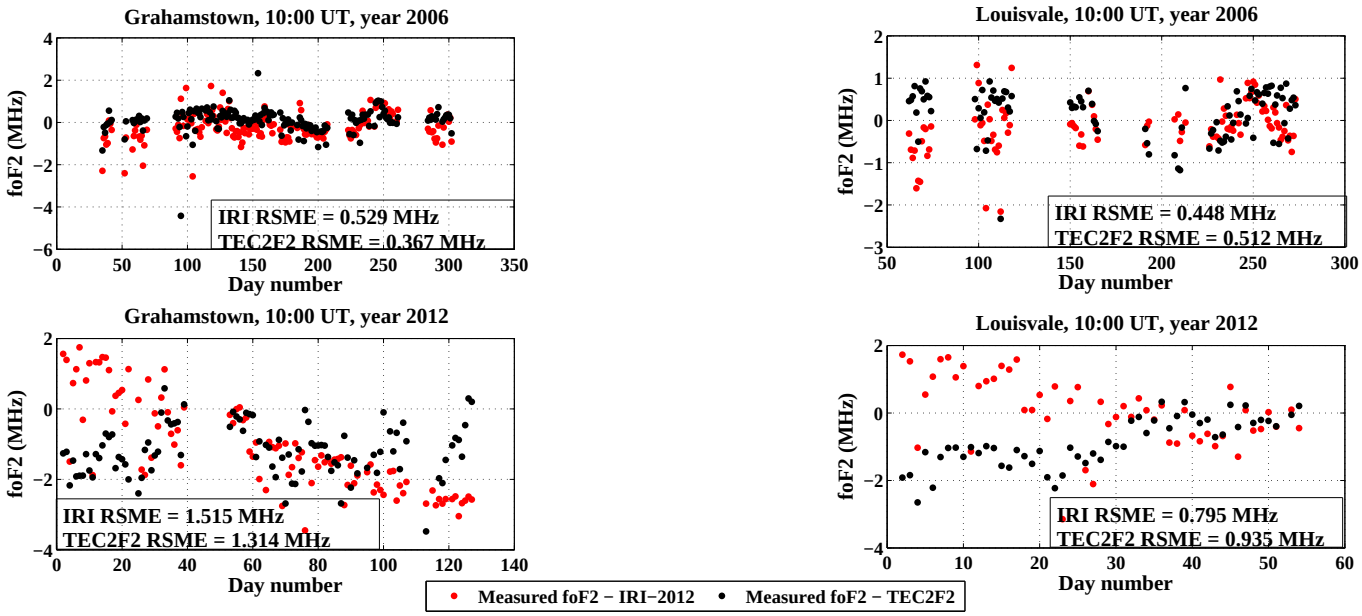

Figure 5.12: Residues of the 10:00 UT measured foF2 and model results (IRI-2012 and TEC2F2) during solar minimum (2006) and approach to solar maximum (2012). The measured values are from Grahamstown and Louisvale ionosonde stations. The TEC2F2 shows a lower RMSE during solar minimum than during the approach to solar maximum.

maximum. During solar maximum, the TEC2F2 model overestimates the foF2 values on average by a magnitude of 1 MHz. A comparison between the two models shows that the TEC2F2 model performs better than the IRI-2012 model during solar minimum than during the approach to solar maximum.

However, it should be noted that these conclusions were reached based on a limited amount of data for solar maximum. A comprehensive validation of the TEC2F2 should be done when the GPS database for South Africa expands to include more data for the solar maximum period.

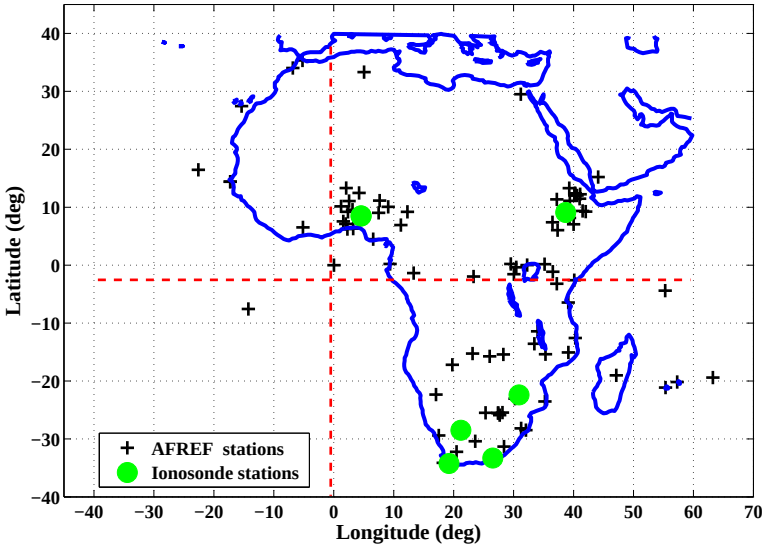

Figure 5.13: Ionosonde and AFREF GPS receiver networks over the African continent.

5.3 TEC2F2 Development over Africa's Equatorial Region

After the validation process had been completed and the conclusion drawn that the TEC2F2 method was more accurate at estimating the foF2 parameter than the IRI-2012 model in the mid-latitudes (South African region), the TEC2F2 model was applied to the rest of Africa where the distribution of ionosondes is significantly lacking. Figure 5.13 shows the sparsity of ionosondes as compared to GPS receivers over the African content. The receivers plotted on this map belong to the African Geodetic Reference Frame (AFREF) network.

In this section Africa's equatorial region is emphasised, because it is one of the most dynamic yet under-represented regions in ionospheric studies.

To adapt the TEC2F2 model to the equatorial latitudes, a set of new coefficients had to be obtained, since the model coefficients are latitude and longitude dependent. The new coefficients would represent both

Table 5.4: Stations from which the equatorial TEC2F2 model coefficients were obtained.

GPS station code	Geographic location	Dip	Country	Ionosonde	Geographic location	Dip
BJPA	9.3^o N, 2.6 ^{o} E	5.9^o S	Benin/ Nigeria	Ilorin	8.5^o N, 4.5^o E	8.0^o S
BRFT	3.7^o S, 38.8^o W	15.4^o S	Brazil	Fortaleza	3.7^o S, 38.8^o W	15.4^o S
PALK	7.3^o N, 80.7^o E	0.9 ^{o} S	Sri Lanka/ Marshall Islands	Kwajalein	9^o N, 167.2 ^{o} E	8.1^o N

the northern and southern equatorial regions, assuming a symmetric ionosphere about the geomagnetic equator. However, due to the paucity of ionosonde data over Africa's equatorial region, data from other stations that were longitudinally distant from Africa's equatorial region, but within the $\pm$ 20^o geomagnetic latitude range were chosen to fill the data gaps. See table 5.4 for a list of GPS and ionosonde stations used.

As a precautionary measure, before the data from the stations listed in table 5.4 could be used in the analysis, the following conditions had to be satisfied

1. Low longitudinal variability: The foF2 or TEC measured at any given point in the northern or southern equatorial anomaly should remain almost the same as the anomaly drifts westwards following the geomagnetic equator. This condition was set to ensure that data from stations that are longitudinally distant from the region of interest would not create substantial errors in the proposed model.

2. Symmetry: The foF2 or TEC measured at any point in the southern anomaly region should be approximately equal to that mea-

sured at the conjugate point in the northern anomaly. This condition was set to ensure that the proposed model could be used both in the northern and southern equatorial anomaly regions.

5.3.1 foF2 Longitudinal Variability Test

The daily foF2 data (covering the year 2010) from the ionosonde stations listed in table 5.4 were used for this analysis. For comparative purposes, the time difference between the stations was removed using

$$t = \begin{cases} t_c = t_s - \frac{24(\phi_r - \phi_s)}{360} \\ t_c < 0,\ t_c = t_c + 24 \end{cases} \tag{5.4}$$

where t_c is the new time in hours after removing the time difference, t_s is observation time in hours at the time-shifted station and ϕ_r and ϕ_s are the geographic longitudes of the reference and time-shifted stations respectively.

Figure 5.14 shows a plot of daily foF2 values for 2010 from ionosonde stations Kwajalein, Fortaleza and Ilorin. The Fortaleza and Ilorin data were shifted in time using Kwajalein as the reference station. The gaps in the data are due either to the low sampling rate (in the case of the Ilorin ionosonde station) or absence of recorded data during that period due to technical problems.

In figure 5.15 the absolute difference between the foF2 values of the reference station and each of the time-shifted stations was determined and plotted. The mean of the results in each plot was calculated and

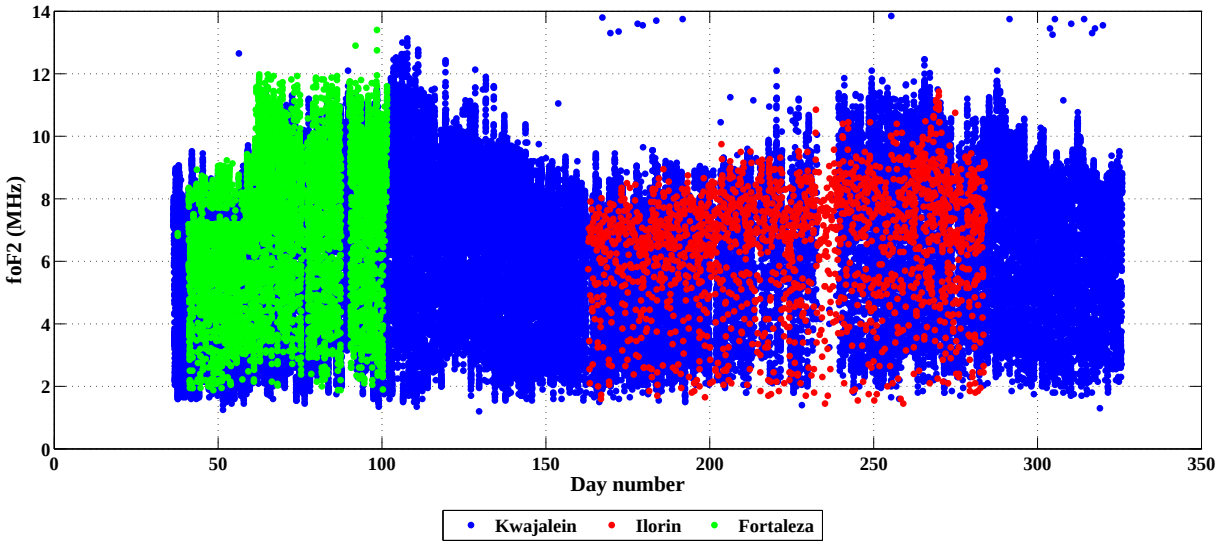

Figure 5.14: Daily ionosonde foF2 values for 2010 from the three selected stations: Fortaleza, Ilorin and Kwajalein.

found to be less than 1.5 MHz. The ratio $\left(\frac{mean(Kwajalein-Ilorin)}{mean(Kwajalein-Fortaleza)}\right)$ was also determined and found to be 0.87.

Scatter plots were also drawn and a line of best fit inserted as illustrated in figures 5.16a (Kwajalein versus Ilorin) and 5.16b (Kwajalein versus Fortaleza). A positive R value above 0.75 was obtained for both plots, thus satisfying condition 1.

Bilitza et al. (2004) also studied the variability of equatorial foF2 using monthly average data from two ionosonde stations, Korhogo (9.3^o N, 5.4^o W, dip 1.6^o S) and Ouagadougou (12^o N, 1.8^o W, dip 5.9^o S), in the African longitude sector. (Korhogo ceased operation in September 2002 due to hostilities in the northern part of Ivory Coast. Ouagadougou was operational between June 1966 and February 1998). They found that Korhogo, which is located in the equatorial anomaly trough, mea-

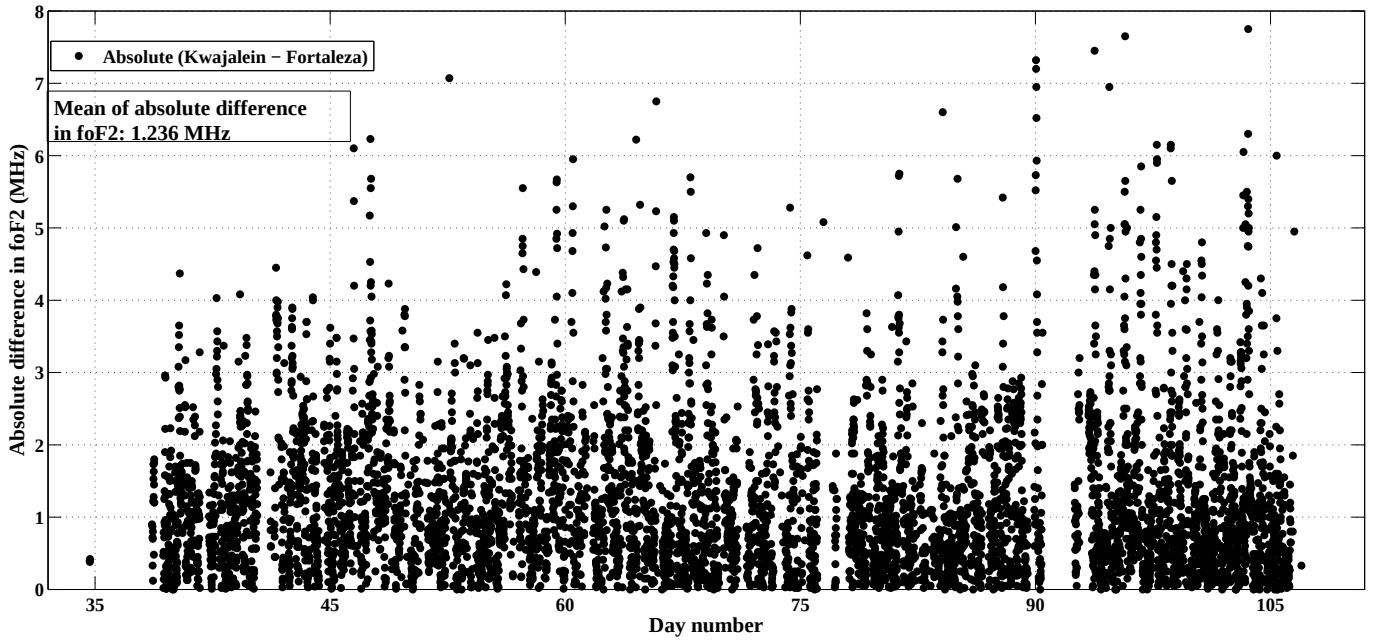

(a)

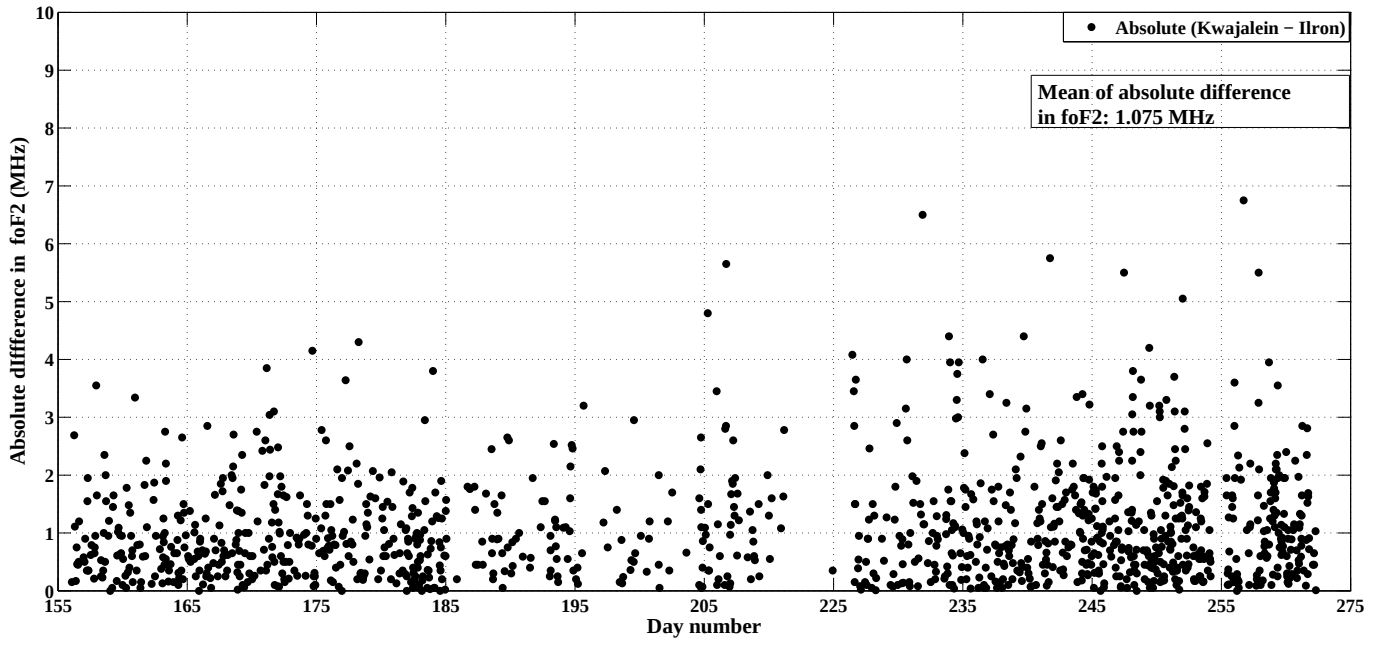

(b)

Figure 5.15: Absolute difference in daily foF2 values for 2010 from equatorial ionosonde stations for (a) Kwajalein - Fortaleza, and (b) Kwajalein - Ilorin.

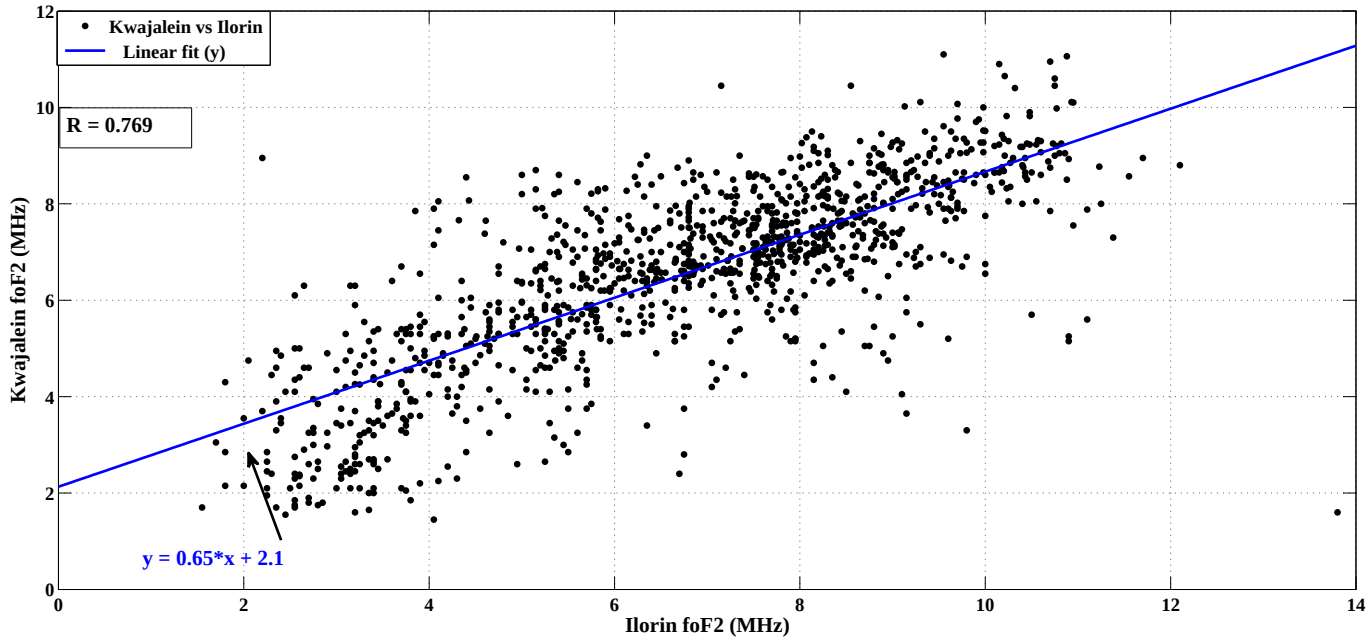

(a)

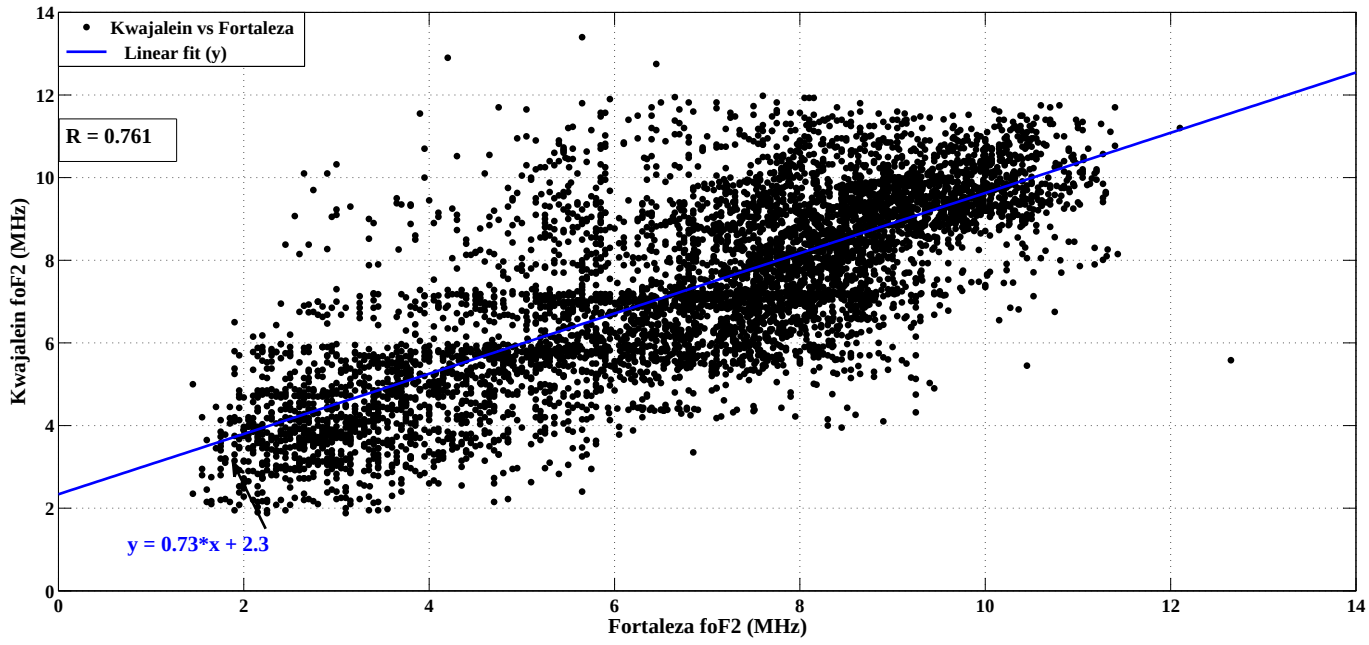

(b)

Figure 5.16: A Scatter of equatorial ionosonde foF2 values for (a) Kwajalein versus Ilorin, and (b) Kwajalein versus Fortaleza.

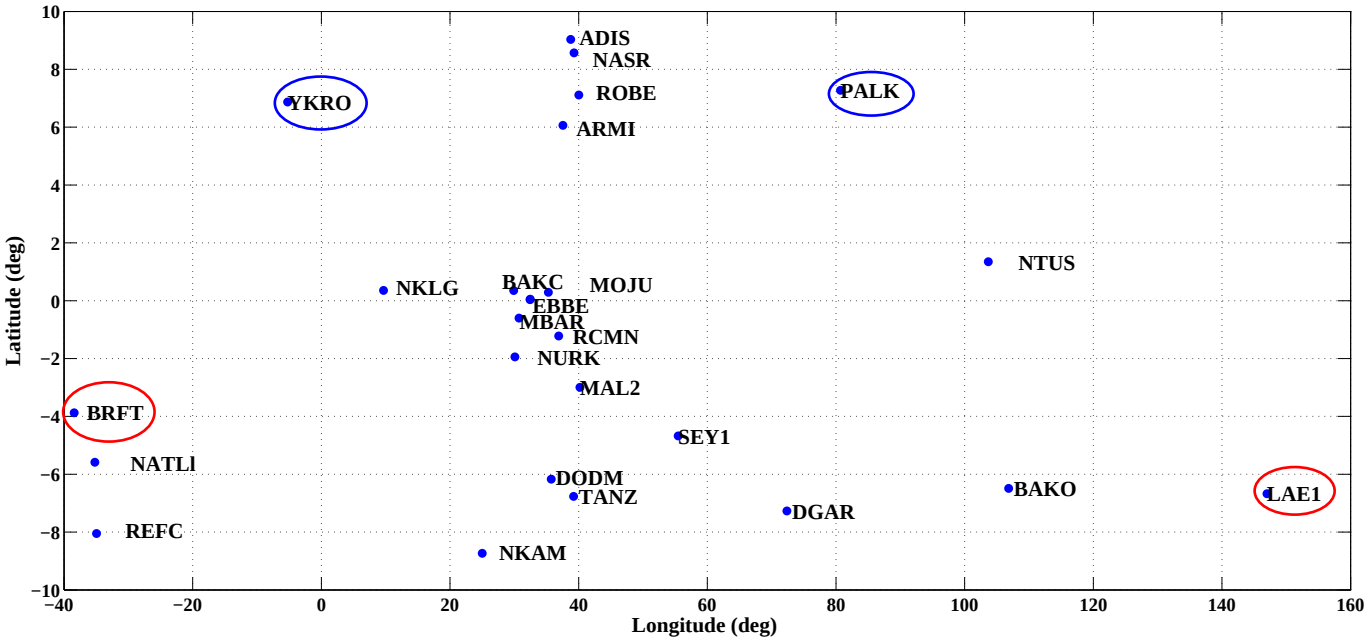

Figure 5.17: GPS stations within the equatorial region.

sured slightly lower foF2 values than Ouagadougou, which is situated closer to the highly variable equatorial anomaly crests.

5.3.2 TEC Longitudinal Variability and Symmetry Test

Figure 5.17 shows the GPS stations in the equatorial region of interest. The circled stations were chosen for this analysis based on their

location. Table 5.5 gives the station codes, geographic location and magnetic dip in 2010 for all the chosen stations.

Table 5.5: GPS stations within the equatorial region between geographic latitude (9^o N - 9^o S) and longitude (40^o W - 170^o E)

Station code	Country	Geographic location	Dip
LAE1	Papua New Guinea	6.7^o S, 146.9^o E	28.0^o S
BRFT	Brazil	3.7^o S, 38.8^o W	15.4^o S
TANZ	Tanzania	6.7^o S, 39.2^o E	35.1^o S
PALK	Sri Lanka	7.3^o N, 80.7^o E	$0.9\ ^o$ S
YKRO	Ivory Coast	6.8^o N, 5.2^o W	12.3^o S

5.3.2.1 Longitudinal Variability Test

The daily TEC values for the year 2010 were derived from the GPS data recorded at the stations listed in table 5.5. The time difference between the stations was removed from the data using PALK and LAE1 stations as the reference stations for the northern and southern geographically located stations respectively. The absolute difference in TEC was then determined and the results plotted. Figure 5.18a shows the absolute difference between stations LAE1 and BRFT, while figure 5.18b shows the absolute difference between stations PALK and YKRO. In both plots the mean of the results was calculated and found to be below 0.5 TECU.

Scatter plots were also drawn as illustrated in figures 5.19a (LAE1 versus BRFT) and 5.19a (PALK versus YKRO). For each scatter plot an R value was calculated and found to be above 0.7. This result agrees with the study carried out by Lin et al. (2001) who examined the TEC response to geomagnetic storms in the western pacific equatorial anomaly region, using stations, DGAR (7.3^o S, 72.4^o E, dip 33.8^o S), BAKO

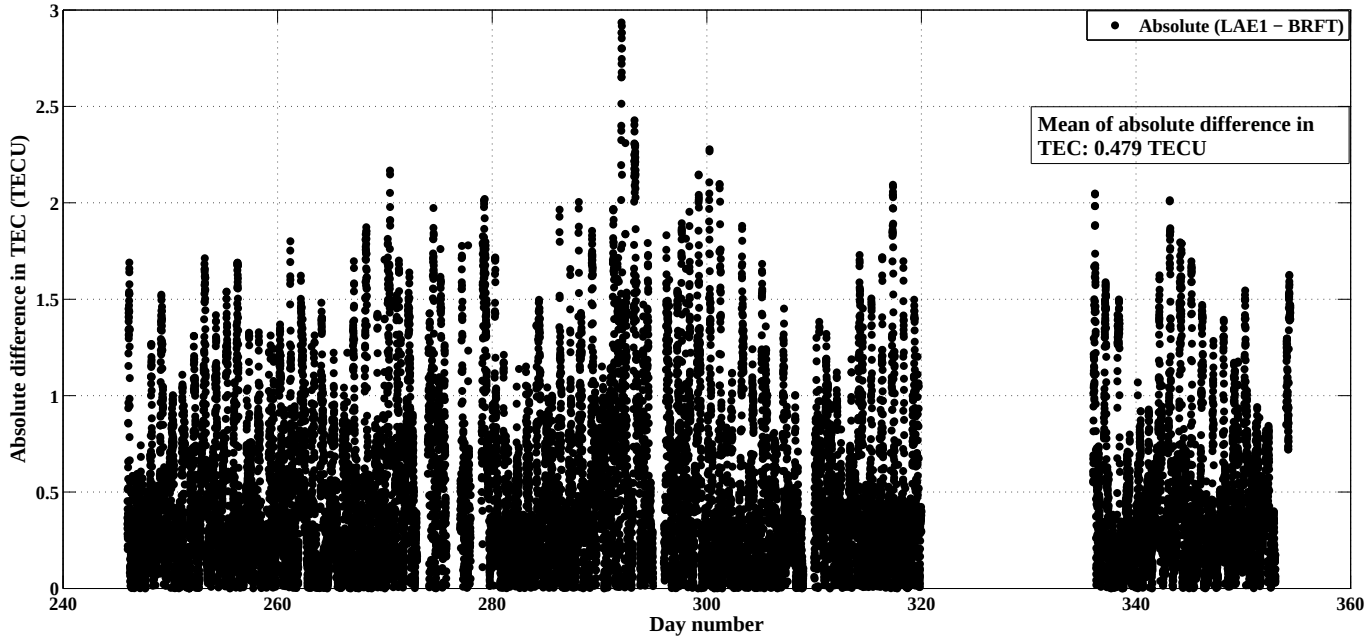

(a)

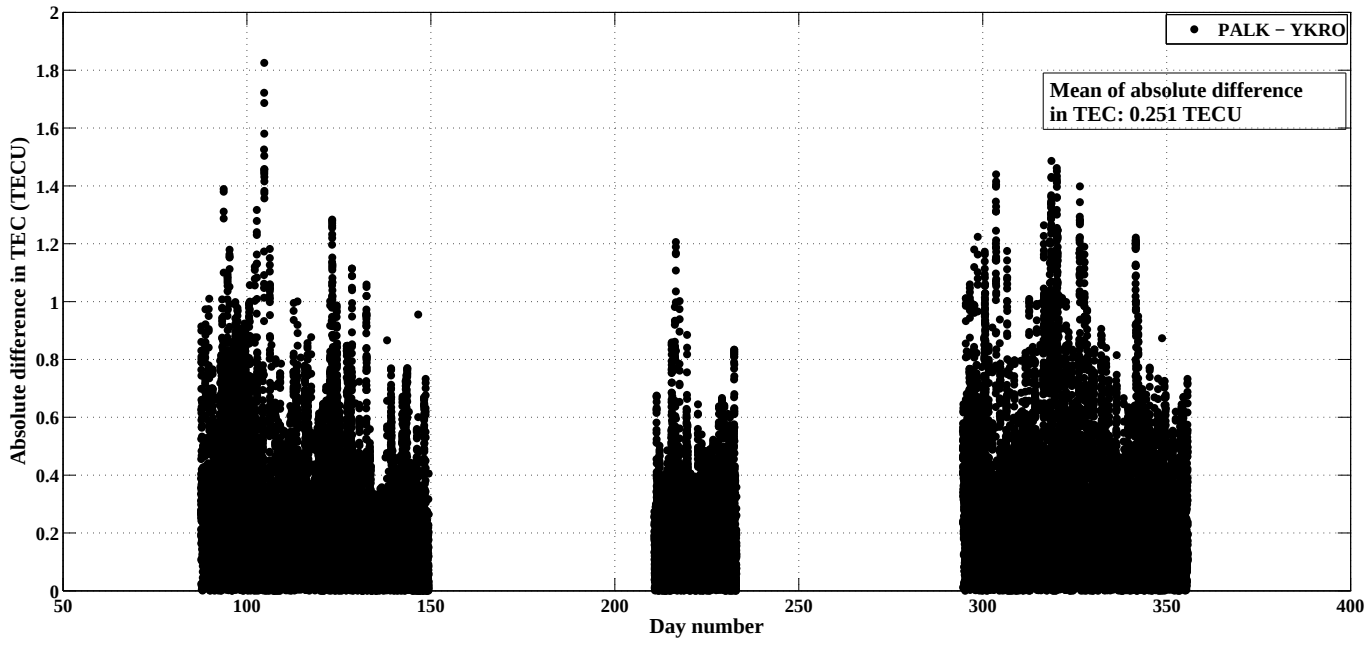

(b)

Figure 5.18: Absolute difference in annual TEC values from equatorial GPS stations for (a) LAE1 and BRFT, and (b) PALK and YKRO.

(6.5^o N, 107^o E, dip 2.6 ^{o} S) and NTUS (1.3^o N, 103.7^o E, dip 15.3 ^{o} S). Their study revealed that TEC variation for longitudinally distant stations was not significant.

5.3.2.2 Symmetry Test

To test for symmetry, two stations TANZ (10.2^o S, 110.0^o E, geomagnetic) and YKRO (10.5^o N, 68.4^o E, geomagnetic), located south and north of the geomagnetic equator were chosen for analysis. The annual absolute difference in TEC values between the two stations was determined and plotted as shown in figure 5.20. The mean of the result was calculated as less than 0.6 TECU. A scatter plot was drawn (see figure 5.21) and a high positive R value above ≈ 0.7 was obtained, thus satisfying the symmetry condition.

However, although the symmetry condition holds as discussed above, note should be taken that not all equatorial variations in the northern anomaly region appear in the southern anomaly region and vice versa. For example, the ionospheric equatorial TEC seasonal variation analysis performed by Tsai et al. (2001) during the solar minimum of 1997, showed that the equatorial winter anomaly does not appear in the southern anomaly region.

5.3.3 Determination of the Equatorial TEC2F2 Model Coefficients

With the low longitudinal variability and symmetry conditions satisfied, data from the ionosondes and GPS stations listed in table 5.4 were used to determine the coefficients for the equatorial TEC2F2 model using the

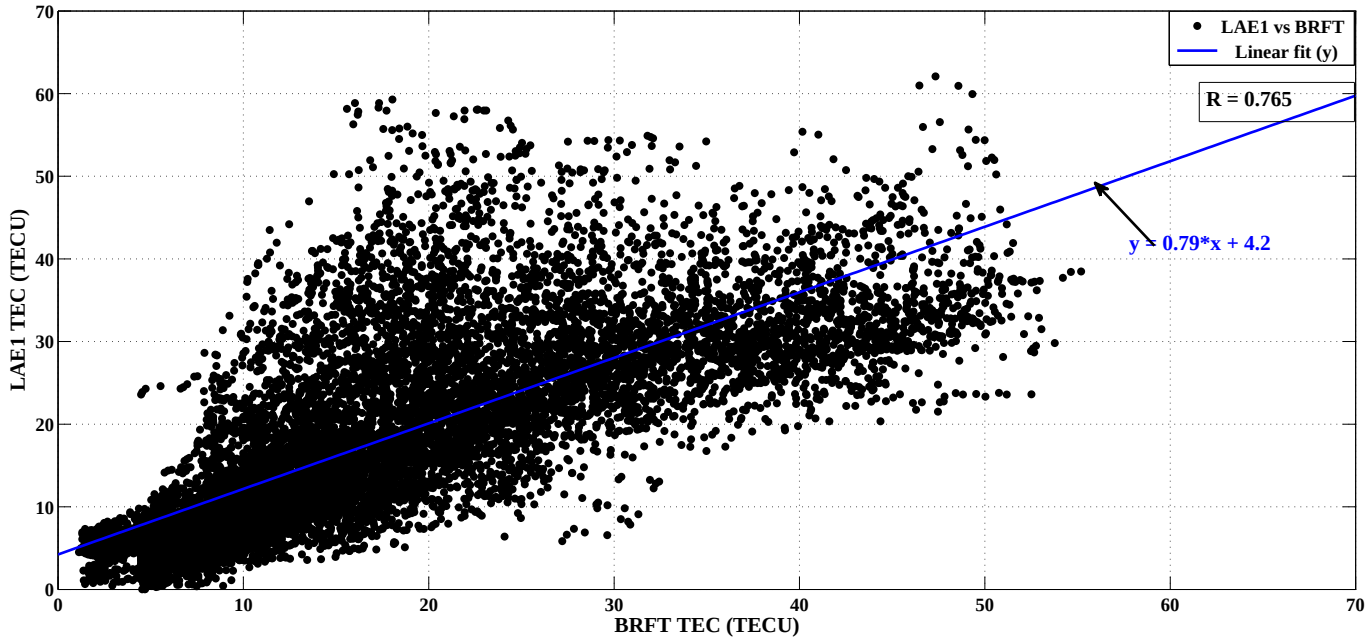

(a)

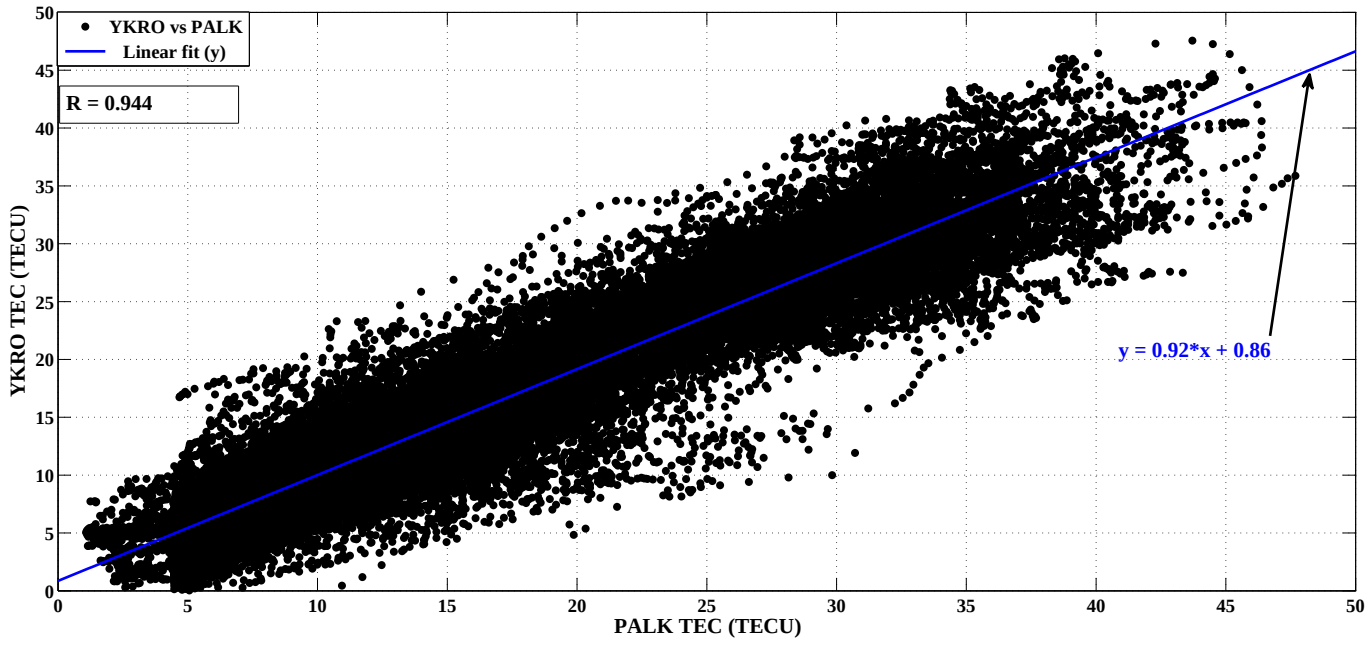

(b)

Figure 5.19: A scatter plot of TEC values for 2010 GPS stations located in the equatorial region for (a) LAE1 versus BRFT, and (b) YKRO versus PALK.

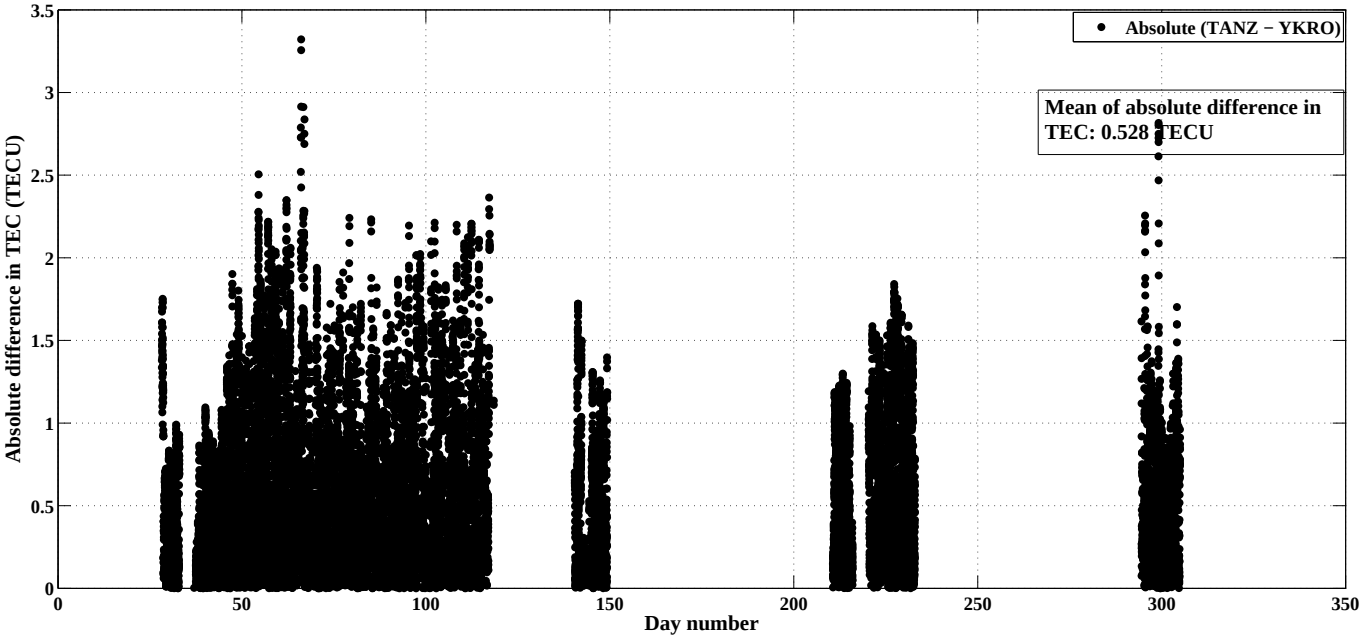

Figure 5.20: Absolute difference between TANZ and YKRO daily TEC values for 2010.

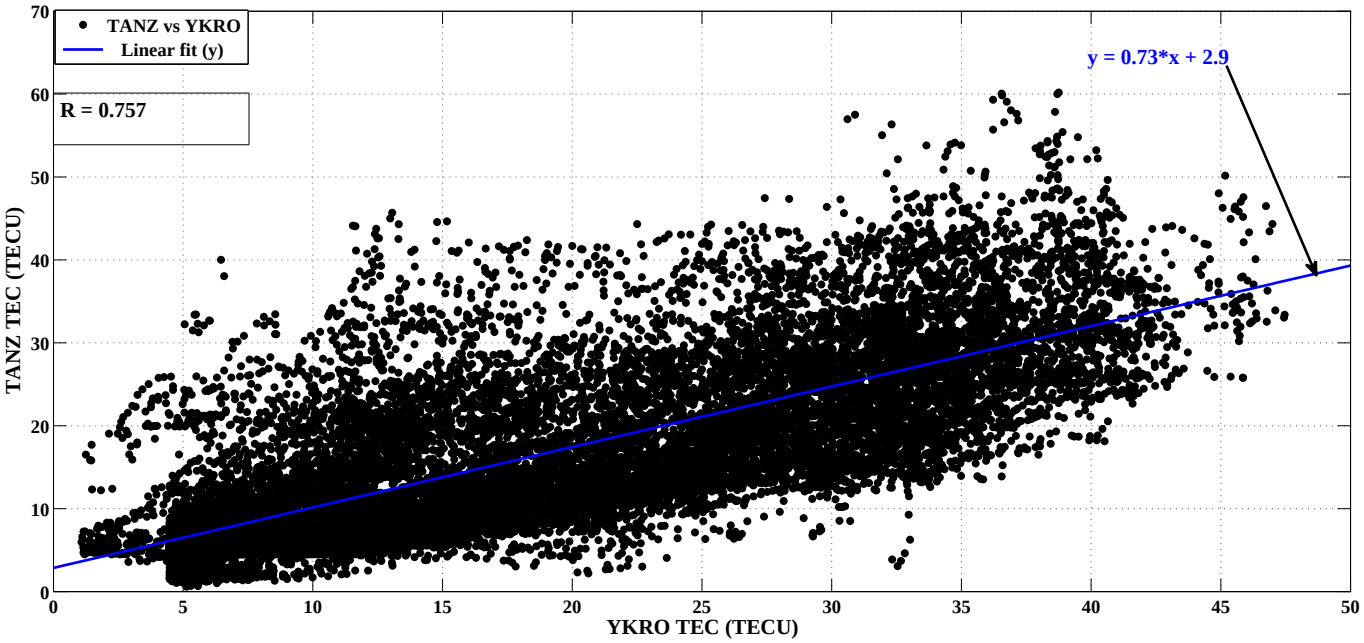

Figure 5.21: A scatter plot of TANZ TEC versus YKRO TEC values for 2010.

Table 5.6: Equatorial TEC2F2 coefficients

Month	00:00 - 5:59 UT		06:00 - 10:59			11:59 - 14:59 UT			15:00 - 19:59 UT		
	p1	p2	p1	p2	p3	p1	p2	P3	p1	p2	p3
Jan	0.221	2.557	0.106	5.286		0.0169	7.325		0.221	2.557	
Feb	0.376	1.132	-0.046	8.819		0.148	3.524		0.191	3.265	
Mar	0.377	1.469	0.108	5.286		0.017	7.325		-0.011	0.480	4.417
Apr	0.360	1.907	-0.019	8.525		0.061	6.428		-0.008	0.557	3.867
May	0.078	6.059	0.078	6.059		0.061	6.428		-0.009	0.509	3.434
June	0.385	1.043	0.267	2.238		-0.029	1.171	-4.530	0.221	2.557	
July	0.321	1.695	-0.065	7.471		-0.029	1.171	-4.530	-0.009	0.509	3.434
Aug	0.271	2.212	-0.122	11.460		0.209	1.522		-0.023	0.702	2.990
Sept	0.317	1.750	-0.122	11.460		0.209	1.522		0.206	4.082	
Oct	0.364	1.752	-0.018	0.963	-4.087	0.209	1.522		0.119	6.122	
Nov	0.339	2.074	-0.122	11.460		0.048	6.865		0.204	2.75	
Dec	0.305	1.924	-0.120	10.610		0.059	5.657		0.198	2.186	

same procedure that was applied over the mid-latitude region. Table 5.6 lists the obtained coefficients. The time interval 06:00 - 14:59 was subdivided into two more sections, 06:00 - 10:59 and 11:00 - 14:59 UT, in order to increase the sensitivity of the model at the peak of the diurnal variation.

5.3.4 Validation of the Results from the Equatorial TEC2F2 Model

5.3.4.1 Diurnal

Figure 5.22 compares diurnal foF2 values from the TEC2F2 model, the IRI-2012 model and Ilorin ionosonde for 2010. The output of the two models was down-sampled to the same resolution as the ionosonde data.

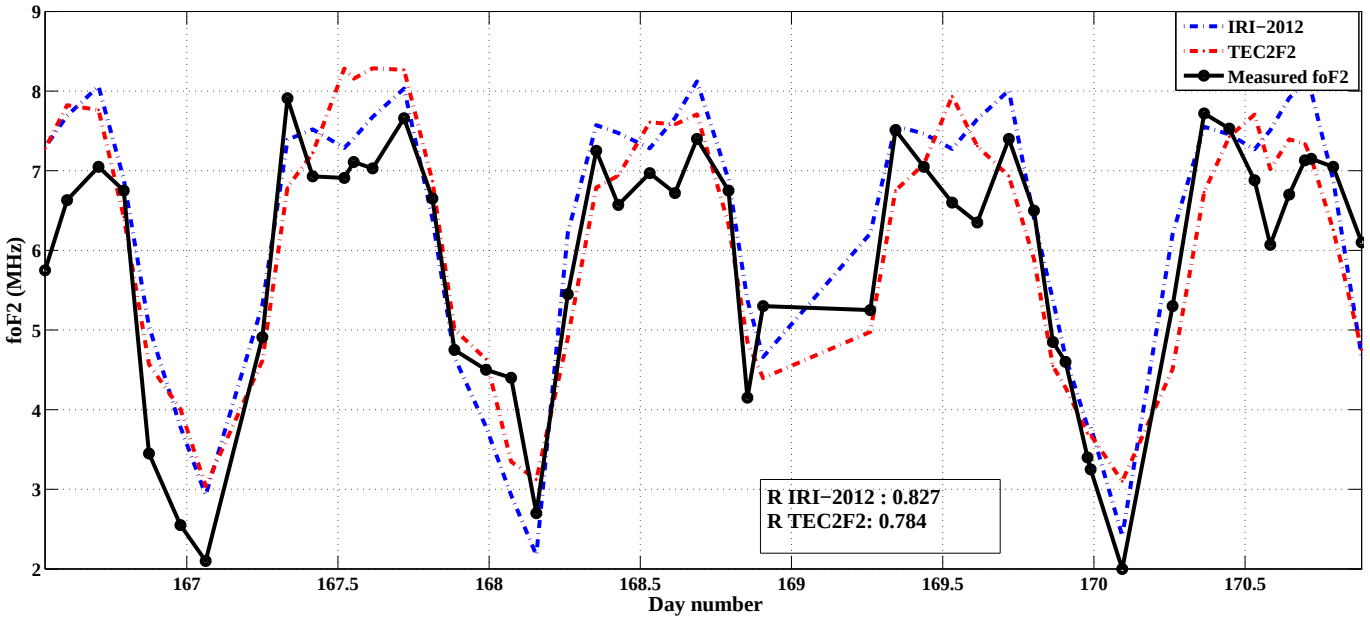

Figure 5.22: A comparison of diurnal foF2 values from TEC2F2, IRI-2012 model and Ilorin ionosonde station.

The TEC2F2 model results were based on VTEC values from the GPS station closest to the Ilorin ionosonde station, BJPA.

The TEC2F2 model gave an R value of $\approx$ 0.8 compared to 0.83 obtained from the IRI-2012 model. However, this result was not credible enough due to the low resolution data used in the analysis. For a better analysis, the performance of both models (TEC2F2 and IRI-2012) was tested at the Fortaleza ionosonde station and the results compared to measured foF2 values at that station, as shown in figure 5.23. (The TEC2F2 model results were in this case obtained using VTEC from the BRFT GPS station). The R value was again determined and the TEC2F2 model performed better with a value of 0.74 compared to 0.68 by the IRI-2012 model.

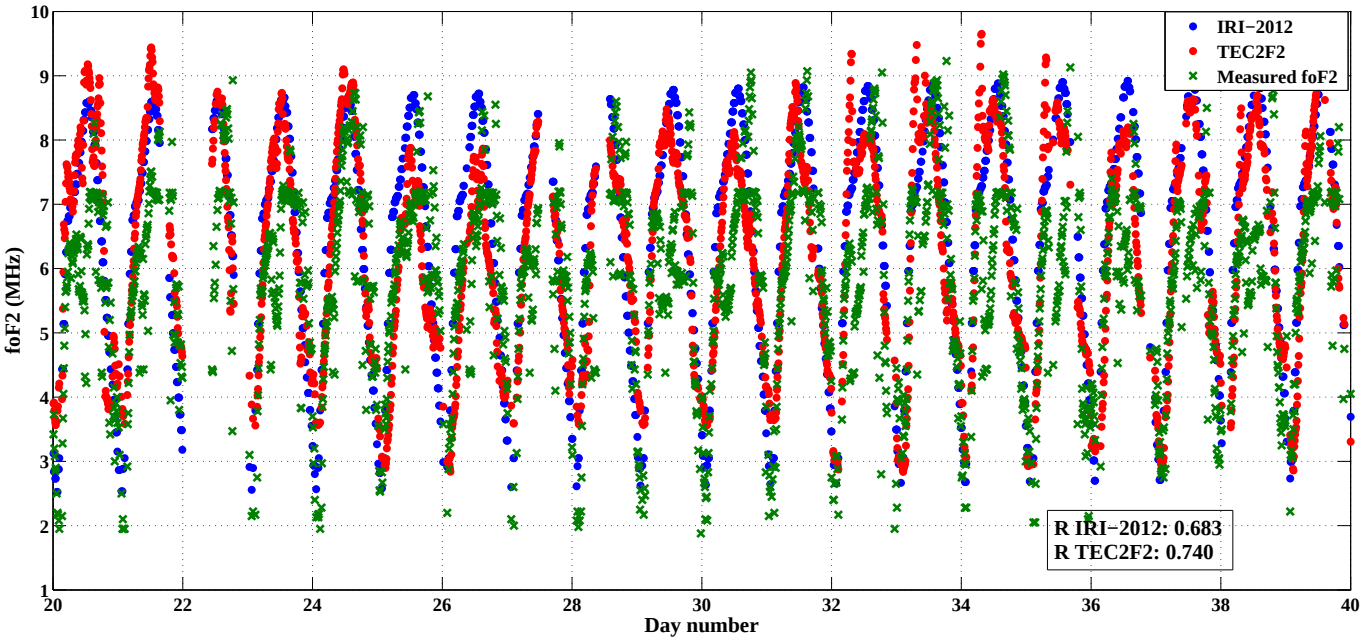

Figure 5.23: A comparison of diurnal foF2 values from TEC2F2, IRI-2012 model and Fortaleza ionosonde.

5.3.4.2 Annual and Seasonal Variability

The TEC2F2 model was used to generate daily 12:00 UT foF2 values in 2010 using data from the following GPS stations found within the African equatorial region, namely ADIS (9.0 ^{o} N, 38.7^o E, dip 1.8^o N), MAL2 (2.9^o S, 40.2^o E, dip 26.6^o S), SEY1 (4.6^o S, 55.4 ^{o} E, dip 27.5^o S) and BJPA (9.4^o N, 2.7^o E, 5.8^o S). The result reflects the expected seasonal variation of foF2 values, namely, high in summer and low in winter (see figure 5.24). A marked increase and decrease of foF2 during equinox (in March and September) and solstice (in June and December) respectively are also well-defined.

For further analysis, only one GPS station, MAL2, was arbitrarily chosen and the TEC2F2 result plotted with the IRI-2012 and measured foF2 values (from the Kwajalein ionosonde station), as shown in figure

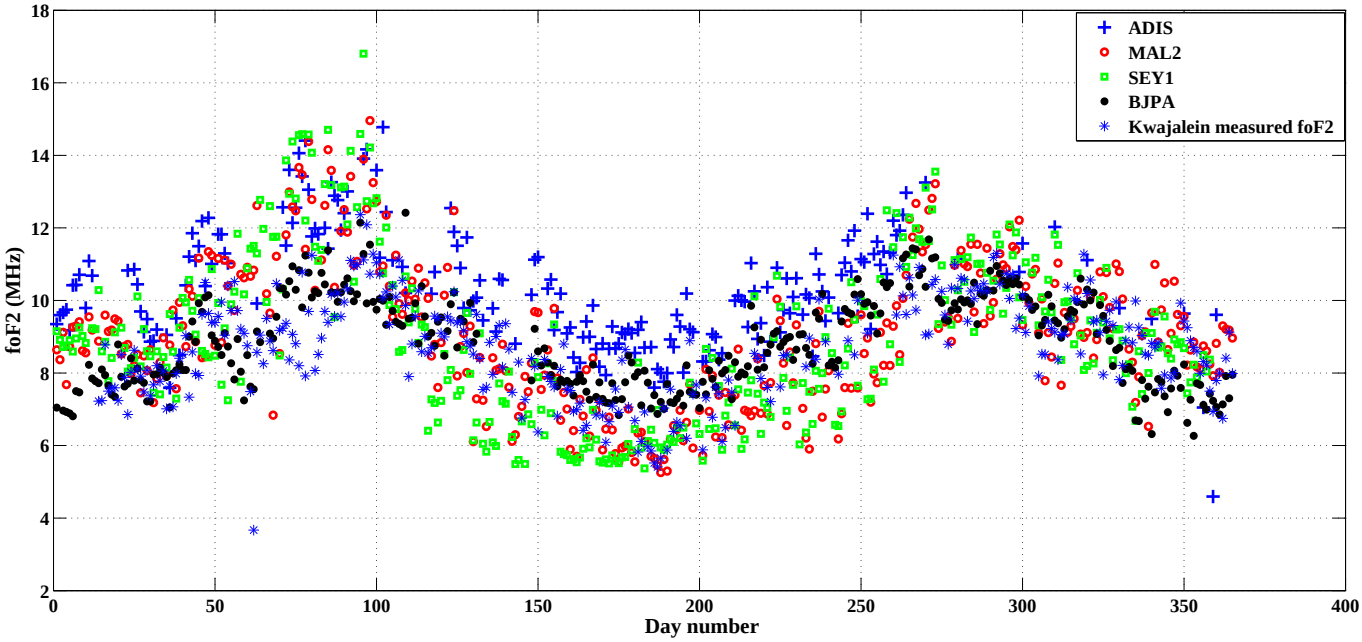

Figure 5.24: Variation of 12:00 UT foF2 values from Kwajalein ionosonde and the TEC2F2 model output based on VTEC from the following GPS stations; ADIS, MAL2, SEY1 and BJPA.

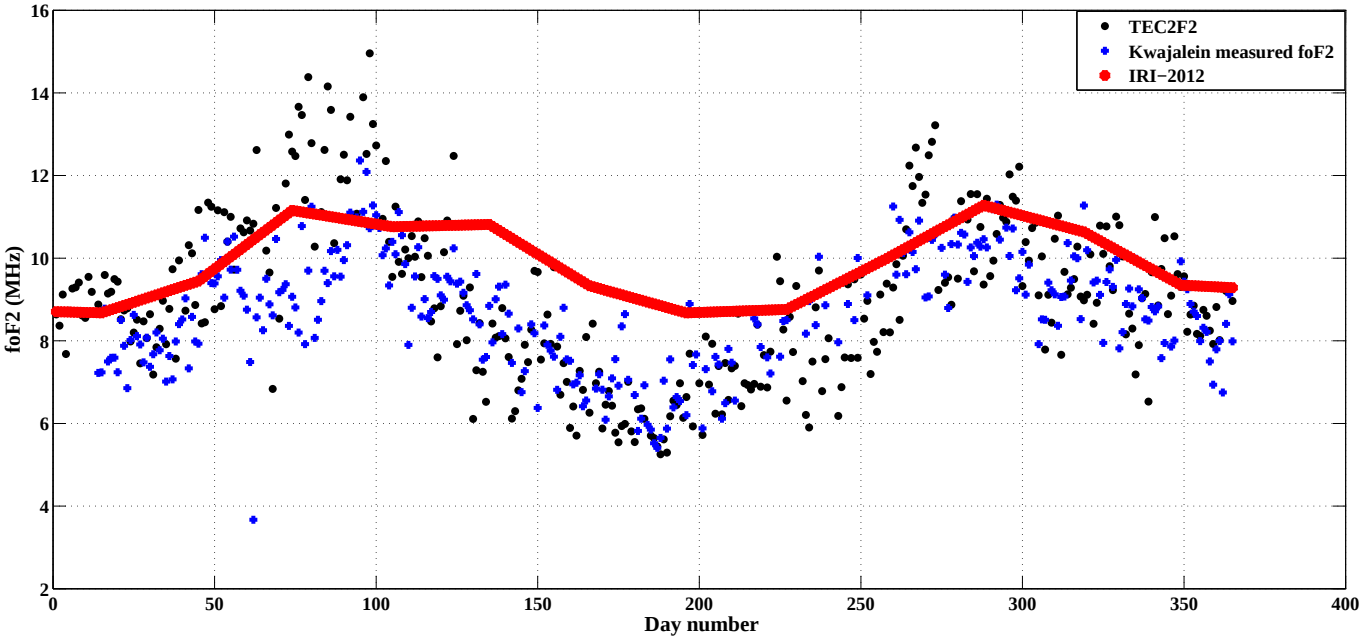

Figure 5.25: A plot of 12:00 UT foF2 values from the TEC2F2, IRI-2012, and Kwajalein ionosonde for 2010.

5.25. During the March equinox the TEC2F2 model overestimated the foF2 values. Despite this inaccuracy, scatter plots (see figures 5.26a and 5.26b) for each model (TEC2F2 and IRI-2012) result and the Kwajalein ionosonde foF2 values, show that the TEC2F2 model better estimates the foF2 values than the IRI-2012 model, with an R2 value of ≈ 0.8 and RMSE ≈ 0.73 MHz, compared to the IRI-2012 model with an R2 ≈ 0.61 and RMSE ≈ 0.85 MHz.

5.4 Analysis of AFREF Stations

Use of the TEC2F2 model in the AIM requires that GPS data be downloaded from the AFREF data archive centre. However, some AFREF GPS stations do not operate continuously throughout the year due to technical problems. Therefore, checking for the presence of data at each AFREF station would increase the response time of the AIM, which would in return affect the temporal resolution of the map.

To overcome this problem, it was decided to select AFREF stations that have historically been continuously operating between 2009 and 2012. The selected AFREF stations would then be checked for data availability by AIM prior to determining the appropriate map. This would significantly reduce the download time and therefore increase the AIM response time, since not all AFREF stations would have to be checked every time.

Data pertaining to all the continuously operating GPS stations as selected (here referred to as "days on") throughout the analysis period was obtained from the AFREF archive. From the data an average,

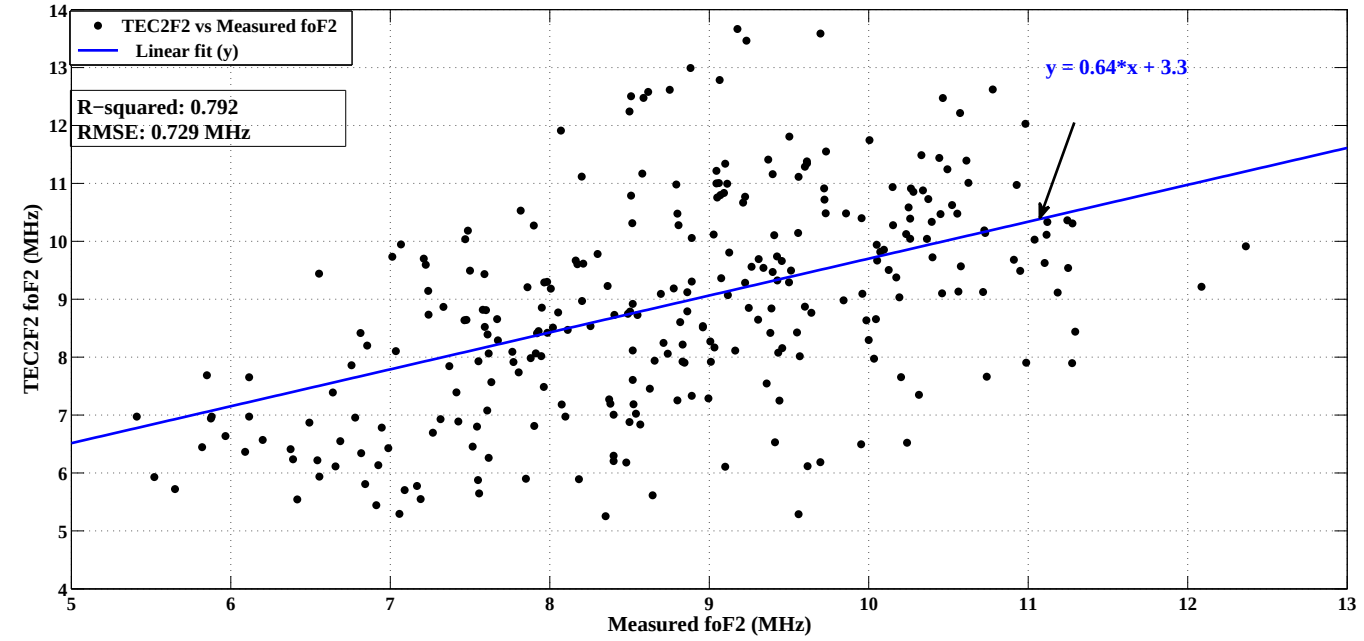

(a)

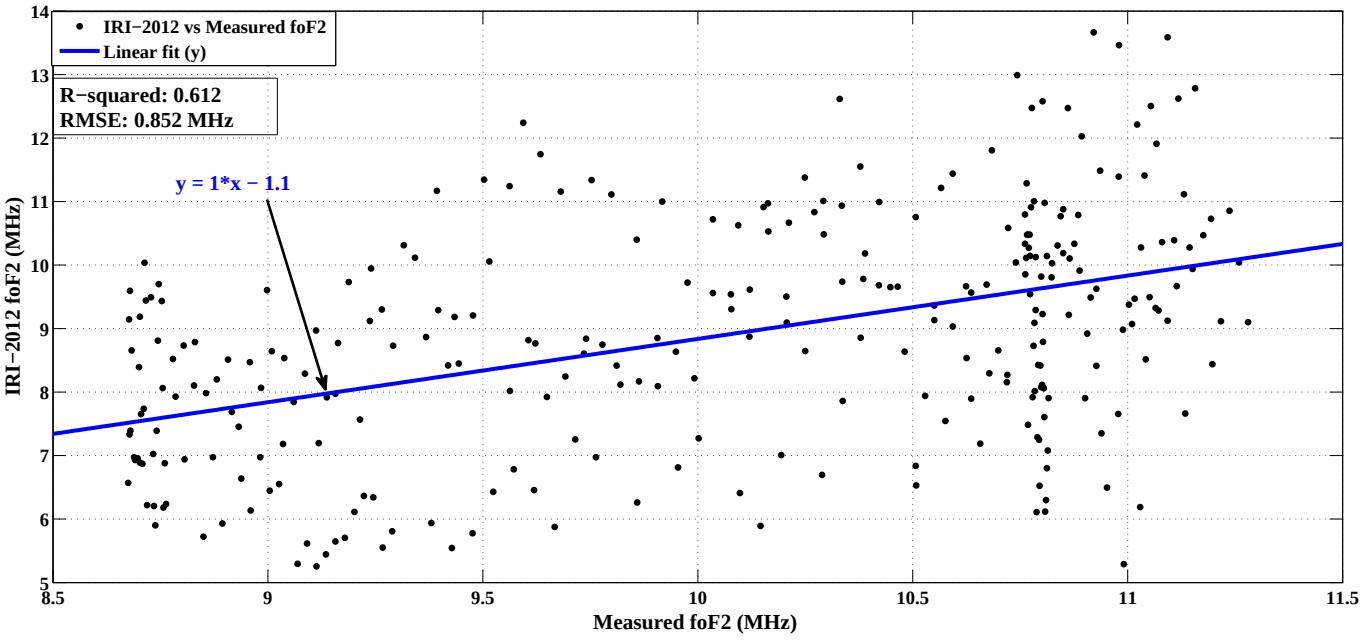

(b)

Figure 5.26: A scatter of 12:00 UT foF2 values at the MAL2 GPS station in 2010 for (a) TEC2F2 model results versus the Kwajalein ionosonde measured foF2, and (b) the IRI-2012 model results versus Kwajalein ionosonde measured foF2.

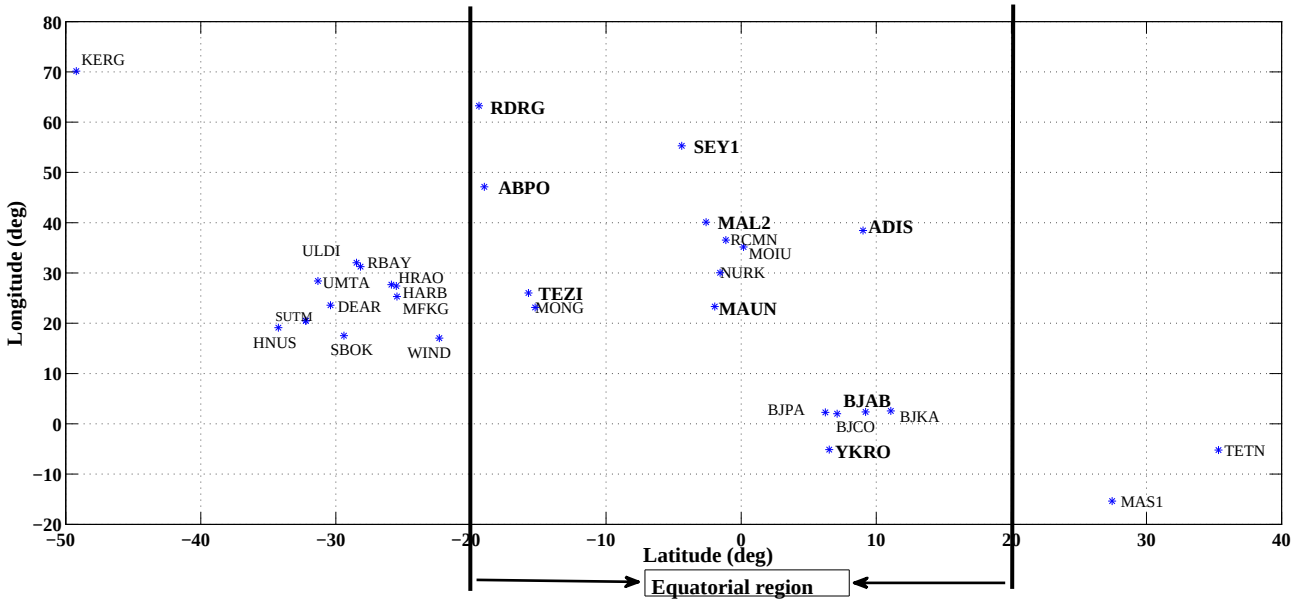

Figure 5.27: AFREF GPS stations that have on average been continuously operational between 2009-2012.

$\left(\frac{days\ on}{Total\ number\ of\ days\ (2009-2012)}\right)$, was determined for each GPS station. Stations with an average below 182 (50 % of the year) were omitted. The results from this process indicated the number of available GPS stations for AIM, and are shown in figure 5.27. The solid lines in figure 5.27 indicate the range of the equatorial anomaly region where the application of the TEC2F2 model is mainly required. The stations selected to primarily be checked during AIM's GPS data download in the equatorial region are marked in bold and also listed in table 5.7. These stations were chosen based on their location within the equatorial anomaly region: north-crest, into the trough and south-crest.

Table 5.7: Stations selected for GPS data download in the equatorial anomaly region

Station code	Country	Location	Average of "days on" (2009-2012)
		North-crest	
YKRO	Ivory Coast	6.8^o N, 5.2^o W	212
BJAB	Benin	9.4^o N, 2.7^o E	237.3
ADIS	Ethiopia	9.0 ^{o} N, 38.7^o E	231.3
		Trough	
NURK	Rwanda	1.9^o S, 30.1^o E	243
MAL2	Kenya	2.9^o S, 40.2^o E	303
SEY1	Seychelles	4.6^o S, 55.4 ^{o} E	204.3
		South-crest	
TEZI	Zambia	15.7 ^{o} S, 26.0 ^{o} E	364
ABPO	Madagascar	19.0^o S, 47.2^o E	243.5
RDRG	Rodrigues	19.7^o S, 63.4^o E	316

5.5 Summary

This chapter presented research on a method to estimate ionospheric foF2 parameter values from GPS VTEC provided the Kp is less than 4. The results show that the TEC2F2 model is more accurate at estimating foF2 values than the IRI-2012 model over the African region. On average, the TEC2F2 model estimated foF2 values estimation 15% better than the IRI-2012 model. However, the model has room for improvement in some areas.

- The accuracy of TEC2F2 at a particular location depends on the spatial distance between the GPS receiver chosen to provide the VTEC data and the point of interest. This was observed when the foF2 values from Madimbo ionosonde station were compared to foF2 values from TEC2F2 using VTEC from the Thohoyandou GPS receiver that is 130 km away.

- The model estimates foF2 values more accurately during solar minimum than during solar maximum. This was due to the fact that the GPS dataset (2006-2012) did not include enough data for the solar maximum period. This can be improved upon as the GPS database over Africa expands to include more data.

- The model needs further validation over the equatorial region once the ionosonde database includes enough data from this region.

The next chapter discusses the use of occultation data in the AIM in an effort to further improve the map's accuracy.

Chapter 6

The Use of Occultation Data in AIM

6.1 Introduction

An occultation is an event that occurs when one object is hidden by another that passes between it and the observer. In recent years, the GPS has been exploited via radio occultation techniques to obtain profiles of refractivity, temperature, pressure and water vapour in the neutral atmosphere and electron density in the ionosphere (Kursinski et al., 2000). This chapter briefly discusses the basic theory of obtaining ionospheric information from GPS radio occultation observations. The chapter also examines the use of this occultation data to complement existing inputs to the AIM program to enhance its performance.

6.2 GPS Occultation

A GPS occultation occurs when a GPS satellite sets/rises below/above the horizon of a Low Earth Orbit (LEO) satellite. Under such circum-

stances, when the LEO is equipped with a GPS receiver on board, the change in the delay and the bending of the signal path between the GPS and the LEO satellite caused by the ionosphere can be derived from the observations from the GPS receiver on the LEO (Aragon-Angel et al., 2009). With a constellation of 24 GPS satellites around the globe transmitting at L_1 and L_2, the LEO satellite observes approximately 500 rising and setting occultations in a day (Schreiner et al., 1999).

In the ionosphere above about 100 km the contributions of temperature, pressure and water vapour pressure to the atmospheric refractive index are negligible compared to the contribution of free electron density. Using this advantage, ionospheric information (electron density (N_e)) is derived from occultation observations using two techniques, (1) Abel's inversion through the bending angle data, and (2) Abel's inversion using STEC. Each of these techniques is briefly discussed below.

6.2.1 Abel's Inversion Through Bending Angle Data

This technique relies on determining the bending angle (α) and expressing it in terms of the refractivity (μ) of the ionosphere. α can be determined by analysing figure 6.1 which illustrates the scheme of occultation geometry. With reference to figure 6.1, a is the impact parameter, P is the impact at the tangent point, $\mathrm{V_{LEO}}$ and $\mathrm{V_{GPS}}$ are 2-D projections of the GPS and LEO satellite 3-D velocities onto the occultation plane, r_{LEO} and r_{GPS} are the position vectors of the LEO

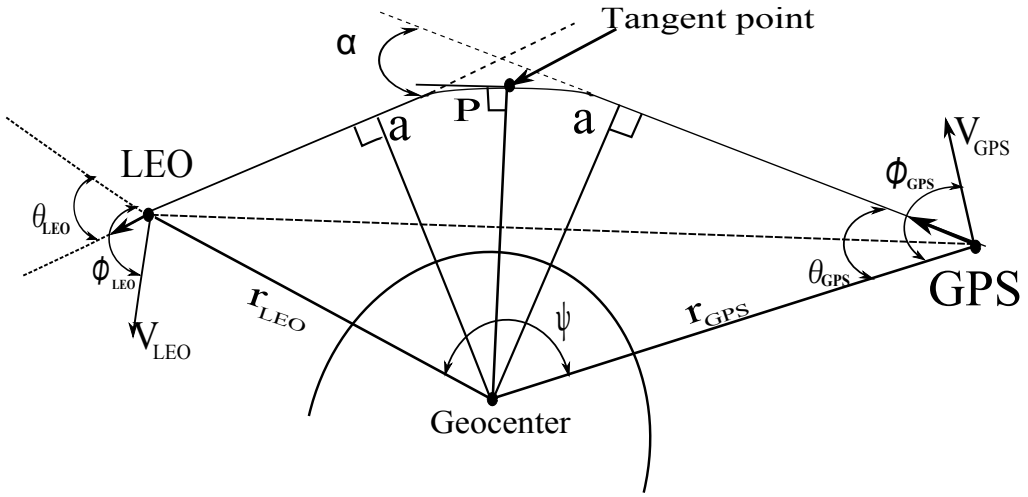

Figure 6.1: Schematic illustration of occultation geometry (García, 2004).

and GPS satellites relative to the geocentre and ψ is the central angle subtended by the ray from the GPS to the LEO satellite.

Using the equation in which the sum of inner angles of a quadrilateral are equal to 2π, the angle α can be expressed in terms of other angles, as illustrated in equation 6.1.

$$\alpha = \psi + \theta_{\mathrm{GPS}} + \theta_{\mathrm{LEO}} - \pi \tag{6.1}$$

If local spherical symmetry within the ionosphere is assumed and equations 6.2 (Bouguer's formula (Born and Wolf, 1986)) and 6.3 (Doppler shift of the carrier frequency (f_d) (Schreiner et al., 1999)) are used, α can further be expressed in terms of a and μ as shown in equation 6.4 (Schreiner et al., 1999; Phinney and Anderson, 1968). The refractivities at the GPS and LEO positions have been assumed to unity which causes an error of no more than 0.5 % (Hajj and Romans, 1998).

$$\mathrm{r_{GPS}}\mu_{\mathrm{GPS}}\sin\theta_{\mathrm{GPS}} = \mathrm{r_{LEO}}\mu_{\mathrm{LEO}}\sin\theta_{\mathrm{LEO}} = \text{constant} \tag{6.2}$$

$$f_d = \frac{c - \mathrm{V_{LEO}}\mu_{\mathrm{LEO}}\cos\left(\phi_{\mathrm{LEO}} - \theta_{\mathrm{LEO}}\right)}{c - \mathrm{V_{GPS}}\mu_{\mathrm{GPS}}\cos\left(\phi_{\mathrm{GPS}} - \theta_{\mathrm{GPS}}\right)} - 1, \tag{6.3}$$

$$\alpha(a) = -a\left[\int_a^{xLEO} + \int_a^{xGPS}\right]\frac{d\mu/dx}{\mu(x)\sqrt{x^2 - a^2}}dx, \;\; x = \mu r \tag{6.4}$$

If the contribution from above the LEO is considered negligible, and taking advantage of the symmetry, then equation 6.4 becomes

$$\alpha(a) = -2\int_a^{\infty}\frac{d\mu/dx}{\mu(x)\sqrt{x^2 - a^2}}dx \tag{6.5}$$

The above equation (6.5) is solved using Abel's transform (Corduneanu, 2008) to express the refractivity as

$$\mu(x) = \exp\left(\frac{1}{\pi}\int_a^{\infty}\frac{\alpha(a)}{\sqrt{a^2 - x^2}}\right)da \tag{6.6}$$

Since $\mu(x)$ depends on N_e and the frequency (f) of transmission (see equation 2.3), a precise measurement of L_1 and L_2 at the LEO satellite can be used to determine the electron density profile.

6.2.2 Abel's Inversion Using STEC

In this technique, the bending angle caused by the ionosphere is considered negligible for F2 layer monitoring, and the path between the

carrier signals L_1 and L_2 not more than 3 km. As a result, the ray path from the GPS to LEO becomes a straight line.

Based on the definition of STEC (see equation 2.14), the total electron content along the ray path becomes

$$STEC = \int_{r_o}^{r_{GPS}} + \int_{r_o}^{r_{LEO}} N_e ds, \tag{6.7}$$

where r_o is the shortest distance from the geocentre to the ray.

The element of geometry (ds) along the ray path, can further be expressed in terms of r using trigonometry:

$$STEC = \int_{r_o}^{r_{GPS}} + \int_{r_o}^{r_{LEO}} N_e(r) \frac{r}{\sqrt{(r^2 - r_o^2)}} dr, \;\; ds = \frac{r}{\sqrt{(r^2 - r_o^2)}} dr \tag{6.8}$$

If local spherical symmetry within the ionosphere again is assumed, equation 6.8 is then reduced to (Schreiner et al., 1999)

$$STEC = 2 \int_{r_o}^{r_{LEO}} N_e(r) \frac{r}{\sqrt{(r^2 - r_o^2)}} dr \tag{6.9}$$

The above equation (6.9) is then solved using Abel's inversion to obtain

$$N_e(r) = \frac{1}{\pi} \int_{r_o}^{r_{LEO}} \frac{d(STEC)/dr_o}{\sqrt{r_o^2 - r^2}} dr_o \tag{6.10}$$

This solution shows that the accuracy with which N_e is determined depends on the accurate measurement of STEC, which again is affec-

ted by errors due to clock biases and phase ambiguity (see chapter 2). Therefore, a precise measurement of these errors is vital.

6.3 Occultation Data Availability Over the African Region

The availability of GPS radio occultation data depends on how many receivers are in orbit. The COSMIC (Constellation Observing System for Meteorology, Ionosphere and Climate) mission (a collaborative project between Taiwan and the United States, launched April 2006) of 6 satellites (with on-board receivers) was able to provide about 2500 occultations per day uniformly distributed all over the globe (Cheng et al., 2006). Currently, COSMIC is at the end of its life. However, there are some missions which are actually providing occultation ionospheric data. Three of these, OCEANSAT-2 (India), SAC-D (Argentina) and Megha-Tropiques (India/France) are flying on-board the Italian ROSA receiver managed by the Italian Space Agency. However, for the current research only data from the COSMIC mission was considered. The data is accessible on `http://tacc.cwb.gov.tw/cdaac/index.html` and the selected database covers the period 2007-2012.

Figure 6.2 illustrates occultation data points over the African continent on an arbitrarily chosen DOY 23 of 2007. The spatial distribution of the data points shows that occultation data offers a good coverage of the continent compared to data used in the previous chapters. However,

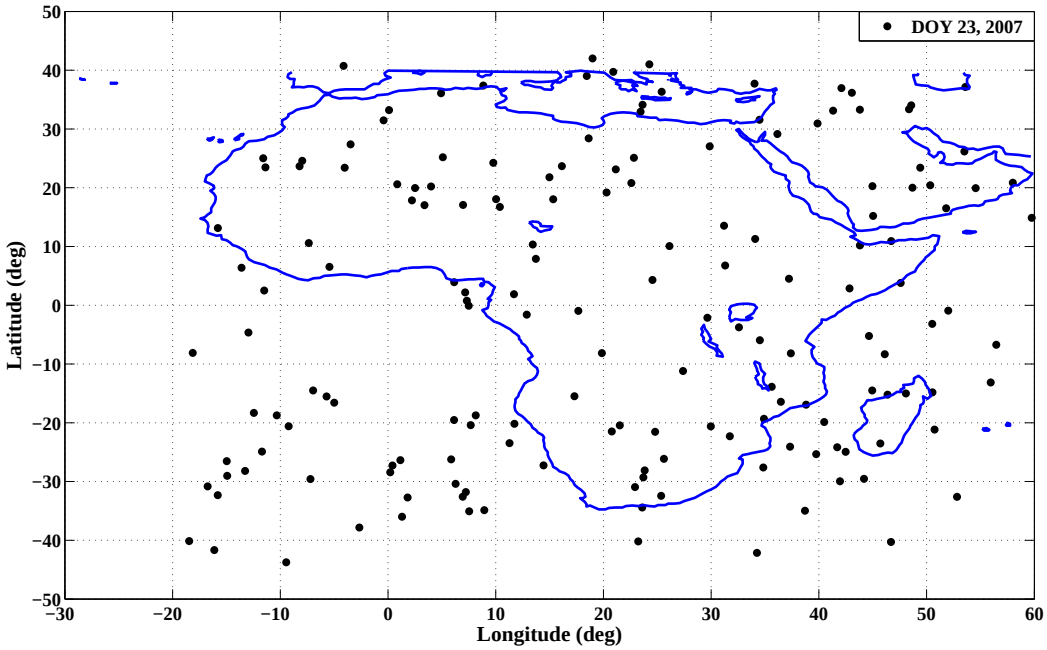

Figure 6.2: Occultation data points (166) over the African sector on DOY 23 of 2007.

despite this advantage, the use of occultation data in the AIM is not a trivial matter, due to the following points:

- The electron density profiles derived from occultation data make use of algorithms that assume ionospheric spherical symmetry, which is not entirely true (Yue et al., 2011, 2010). If the ray from the GPS to the LEO satellite is through a non-spherically distributed ionosphere which is mostly the normal case, the profile generated turns out to be inaccurate.

- The ray traversing geometry causes the GPS radio occultation data to have unique characteristics which are different from the localised point measurements obtained from ground-based ionosondes (Kuo et al., 2001).

- The number of occultations on consecutive days of the year differs due to failed measurements, usually caused by locking onto the GPS carrier signals too late or ending too early during an occulation (Tsai et al., 2009). Figure 6.3a shows an example of the number of occultation data points on arbitrarily chosen consecutive days of the year 23 and 24 of 2009. On day 23 the number of occultations was 233, while on day 24 the number of occultations was 117. This inconsistency was also observed when occultation data points were plotted on DOY 23 of two consecutive years, 2010 and 2011 (see figure 6.3b). The number of occultation data points was 113 and 103 respectively.

- The number of occultations produced during a 24-hour period does not provide a consistent temporal coverage of the ionosphere over a specific region. This is observed in figure 6.4, where only occultations covering Africa's equatorial region ($\pm 20^o$ geographic latitude) were selected on DOY 23 of 2010. The "pencil-like" markings represent the geographic trace of the occultations and the numbers marked in red represent the time (in decimal hours) when that specific occultation occurred.

- Another point to consider is that not all the operative missions carrying on-board receivers provide ionospheric observations (i.e. Leo-GPS satellite STEC profiles and it's inversion products (electron density profiles)).

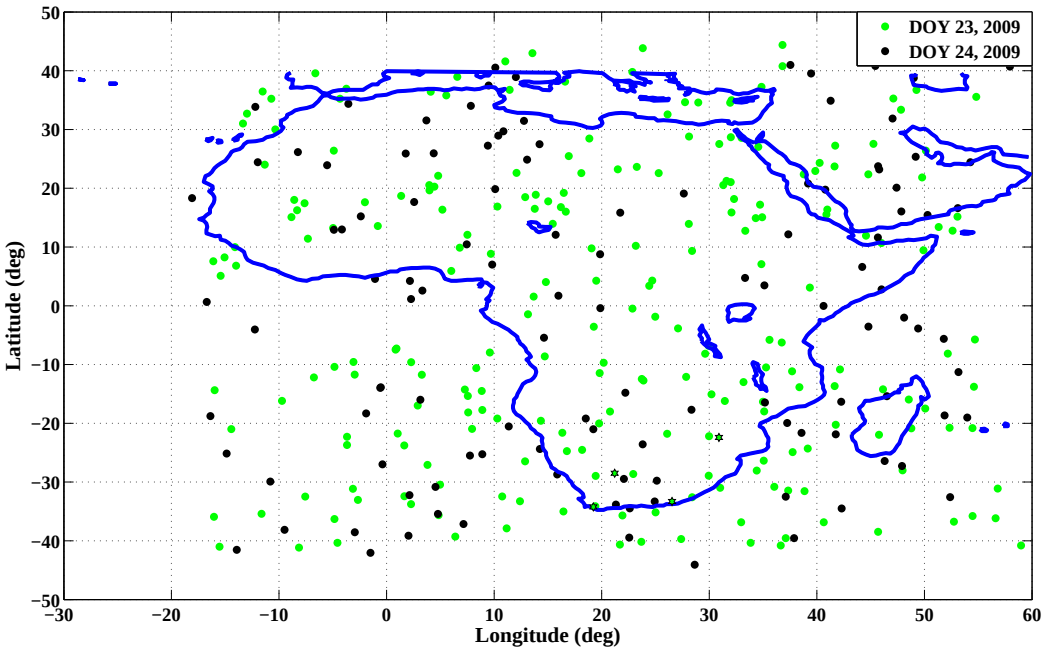

(a)

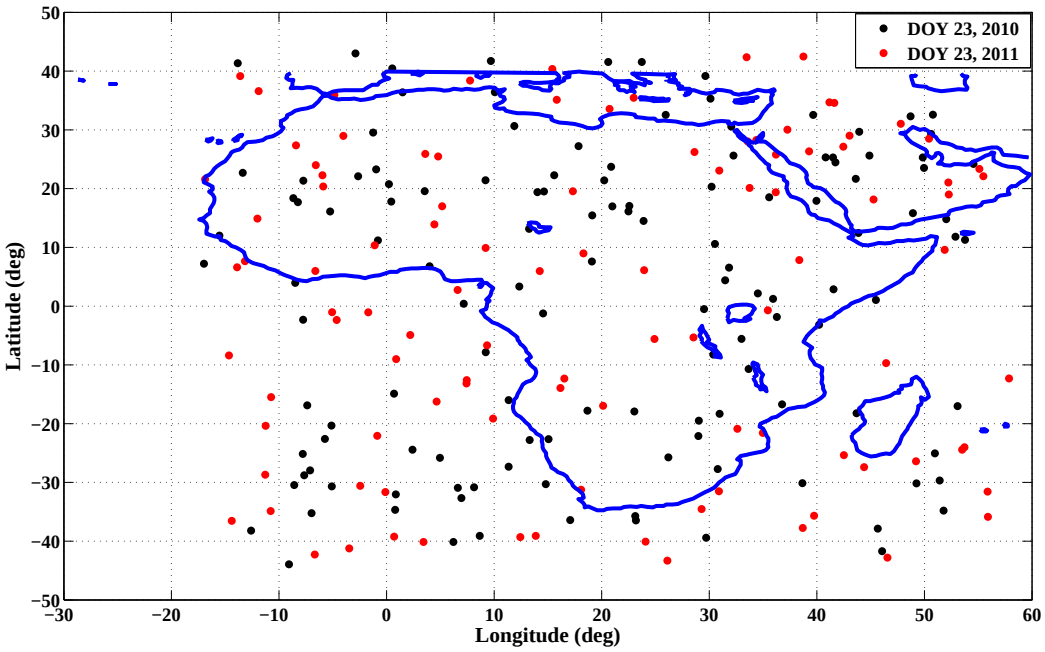

(b)

Figure 6.3: Occulation data points over the African sector. (a) DOY 23 and 24 of 2009, (b) DOY 23 of 2010 and 2011.

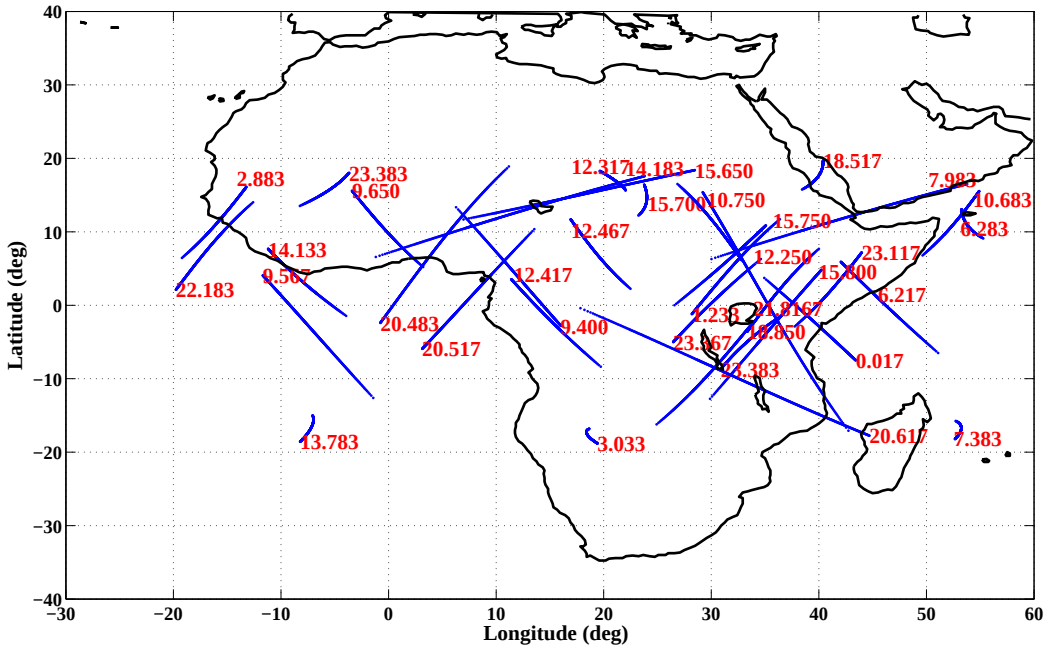

Figure 6.4: A geographical trace of occultations over Africa's equatorial region (covering a latitude range ±20°) on DOY 23 of 2010.

Despite the above shortcomings, occultation data was still considered for use in the AIM, provided it was more accurate than the IRI-2012 model.

6.4 Validation of Occultation Data

In order to assess the accuracy of COSMIC electron density retrievals over the African sector, a comparison of diurnal foF2 values from COSMIC observations with ionosonde measurements from the South African ionosonde network was done.

Figure 6.5 shows the geographic trace of occultations over the South Africa region on DOY 23 of 2010. It is clear to see that the number of occultations on a single day in a given year is not sufficient to provide a full day's information for analysis. To obtain enough data points,

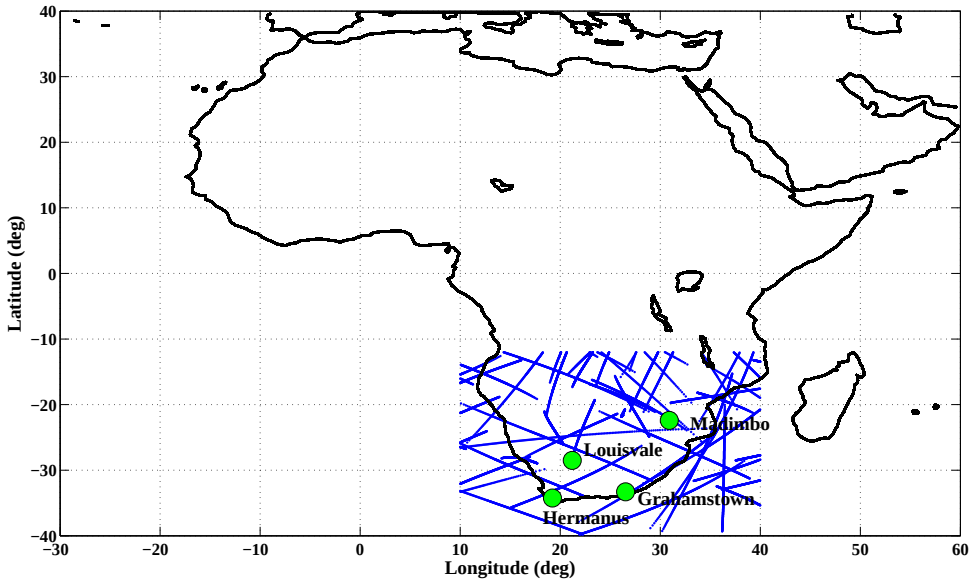

Figure 6.5: A map showing the geographic trace of occultations over the South African region on DOY 23 of 2010.

occultation foF2 values on DOY 23 of years from 2007 to 2012 were plotted, as shown in figure 6.6a. The 2012 noon foF2 values are higher compared to foF2 values of other years. This is to be expected since 2012 is closer to the solar maximum (2013). In figure 6.6b, the raw data was smoothed (using a moving average with a span of 5 data points) and a Fourier curve fit. The result depicts the expected diurnal variation.

Furthermore, occultation foF2 values within a 5^o radius around the ionosonde stations (of the South African network) were selected and compared to the ionosonde foF2 values, as illustrated in figure 6.7. The Louisvale station was omitted from the comparison, since the station did not have enough occultation foF2 values within the specified radius. The average R2 and RMSE for the three stations (Hermanus, Grahamstown and Madimbo) were calculated to be 0.62 MHz and 0.80 respectively. Compared to the IRI-2012 model results (R2 = 0.52 and RMSE =

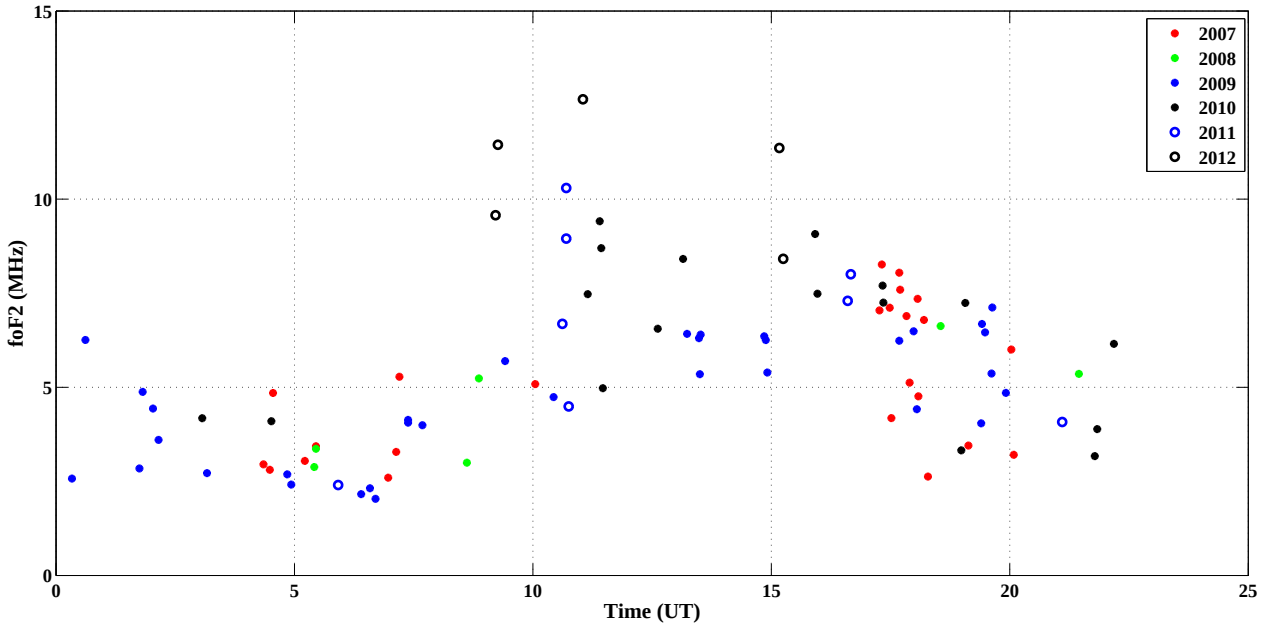

(a)

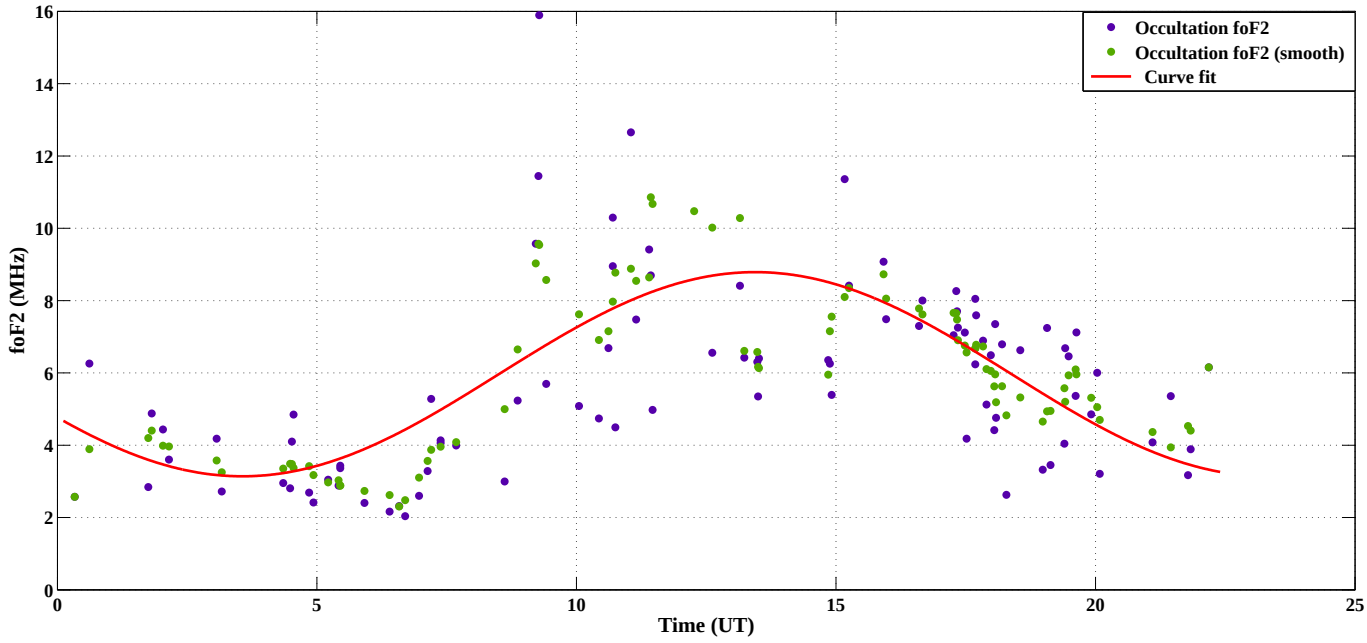

(b)

Figure 6.6: Diurnal occultation foF2 values over the South African region on day number 23 of years 2007 - 2012. (a) raw foF2 values, and (b) smoothed foF2 values.

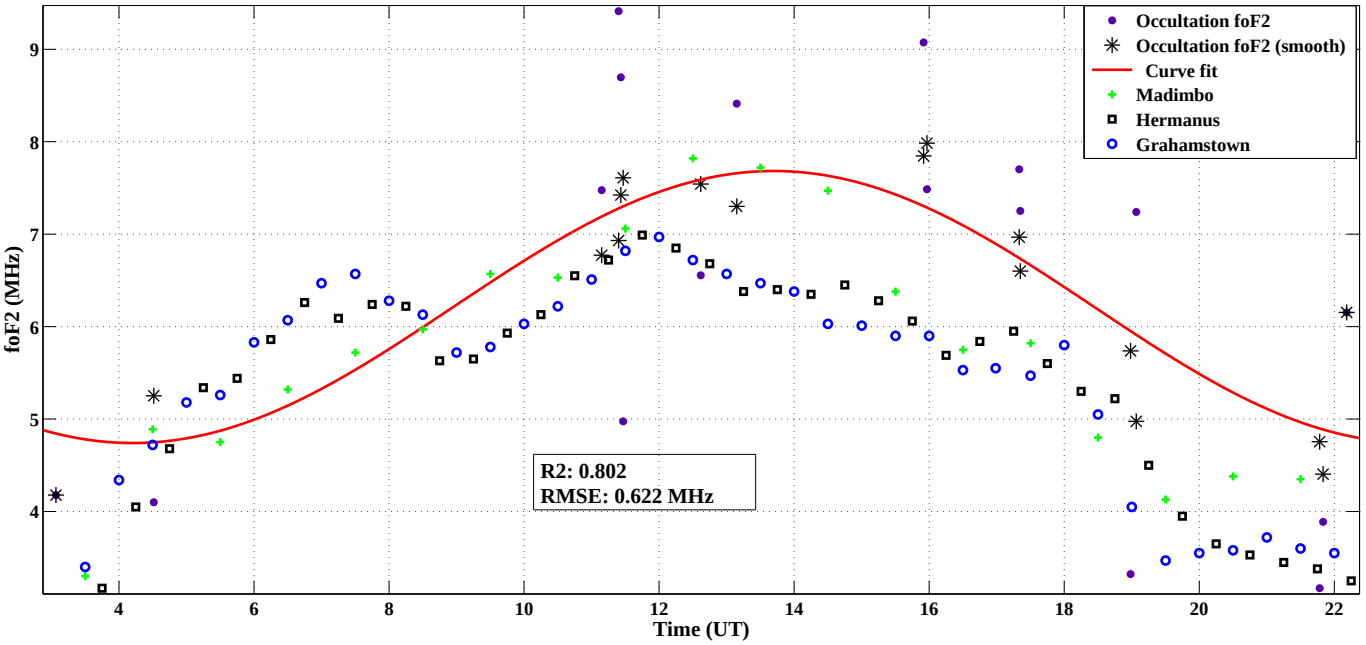

Figure 6.7: Ground ionosonde and occultation foF2 values on DOY 23 of 2010.

0.86 MHz) obtained in chapter 5, occultation data is more accurate at estimating the foF2 parameter.

A number of other researchers have also compared the radio-occulted electron densities of COSMIC with ground-based ionosonde, Incoherent Scatter Radar (ISR), and model predictions to validate the accuracy and precision of COSMIC-based values of parameters. For instance, a short term comparison between COSMIC retrieved electron density profiles and ionosonde and ISR by Lei et al. (2007) revealed both to be in agreement. The derived peak density and height of the F2 layer were in agreement with that calculated by the IRI-2001 model and the National Centre for Atmospheric Research Thermosphere Ionosphere Electrodynamics General Circulation Model (NCAR TIEGCM). However, features such as the north-south asymmetry and longitudinal variation of the equatorial anomaly were not fully present in the IRI-2001 model.

Further, Lühr and Xiong (2010) compared the CHAMP and GRACE observed electron densities with the IRI-2007 predictions. They found that the IRI-2007 can on average overestimate the electron density by as much as 50 % during 2008 and 60 % during 2009, especially during the daytime of low latitude regions. Jakowski and Tsybulya (2005) compared ionospheric radio occultation data (from CHAMP) with IRI-2001, and found that the IRI-2001 model systematically overestimates the electron density above 250 km, whereas it underestimates the lower part of the ionosphere under high solar activity conditions.

Note: The data used in the analysis are post-processed data (evaluated by considering precise orbit estimates), usually available after 6 weeks of observation. In a near real-time case, the data is provided on a 3-hourly basis, but with an accuracy trade-off due to the use of less accurate methods and models for obtaining the geometry solution. Therefore, for the sake of accuracy in the AIM, occultation data was only used if the required map was historic (dating back more than 6 weeks from the present).

6.5 Summary

This chapter briefly discussed the background theory to obtaining ionospheric information from a radio occultation technique (LEO-GPS). The shortcomings of using occulation data in the AIM were pointed out. A comparison of diurnal derived occultation foF2 values with ionosonde measurements showed that the former was more accurate at estimating the values of the foF2 parameter than the IRI-2012 model. However, due to the delay in obtaining the precise orbit estimates, GPS occultation

data was considered for use in the AIM only when developing historic ionospheric maps. The next chapter describes the operation of AIM and use of its interface.

Chapter 7

AIM's Operation and Interface

7.1 Introduction

This chapter discusses the operation of AIM and the use of its interface. The focus is placed on three ionospheric parameters, foF2, TEC and M3000F2, which are vital in radio communication. The interface was designed with the Matlab Graphical User Interface (GUI) software with the objective of making the map user-friendly. It can be operated in two modes, manual or automatic.

7.2 The Manual Mode Interface

This is the default interface when the AIM program is set to run. It is divided into four sections labelled A, B, C and D as shown in figure 7.1.

- Section A requires an input of the time (year, month, day and hours (in decimals)) for which the program should run. The default time is the time on the computer time on which the program is being

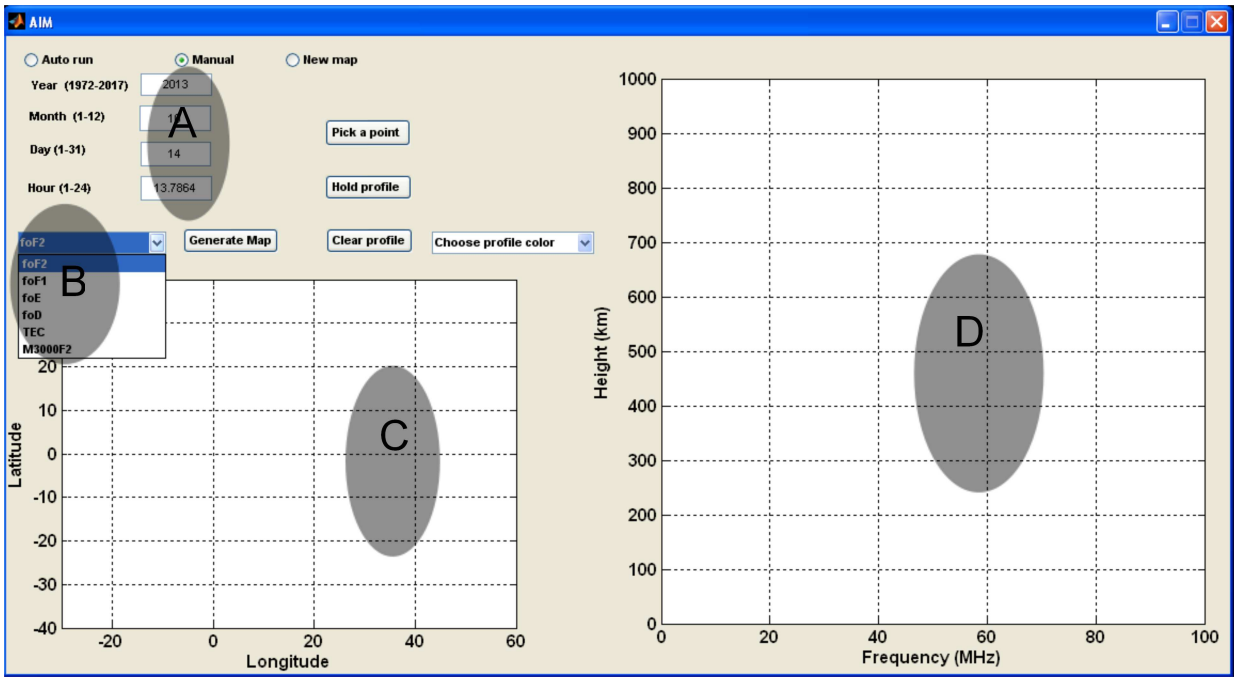

Figure 7.1: Manual mode interface of AIM.

run, but it can be edited to suit the end-user's need. For historic maps, the time limit is 1972 since the current versions of the IRI and SABIM only date back that far. If a wrong year, month, day or hour is entered, an error message is displayed on the screen, warning the user of the invalid input. The program will not continue until the error has been corrected. Figure 7.2 shows an example of an attempt to run the program with an invalid year (1962) input.

- Section B offers the ionospheric parameters (foF2, foF1, foE, foD, TEC and M3000F2) from which the user chooses to generate the desired map.

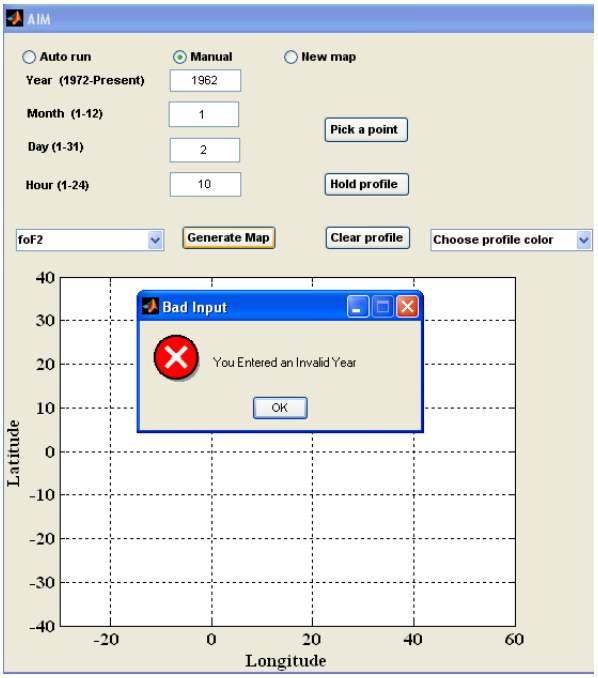

Figure 7.2: An error message due to an invalid year input.

- Section C displays the axes on which the geographical (longitude, latitude) variation of a chosen parameter is represented. The geographical area is limited to 40^o S - 40^o N and 30^o W - 60^o E.

- Section D displays the generated profiles for any chosen geographical location. The location or point on the map is selected by using the push button "Pick a point". If the selected location is outside the map's range, an error message ("Out of Range") is displayed on the screen and no further action is taken by the program.

- The "clear profile" and "hold profile" buttons have the same functions as explained in section 3.7. The "Choose profile color" pop-up menu button can be used to plot different profiles in different colours once the "hold profile" function is active.

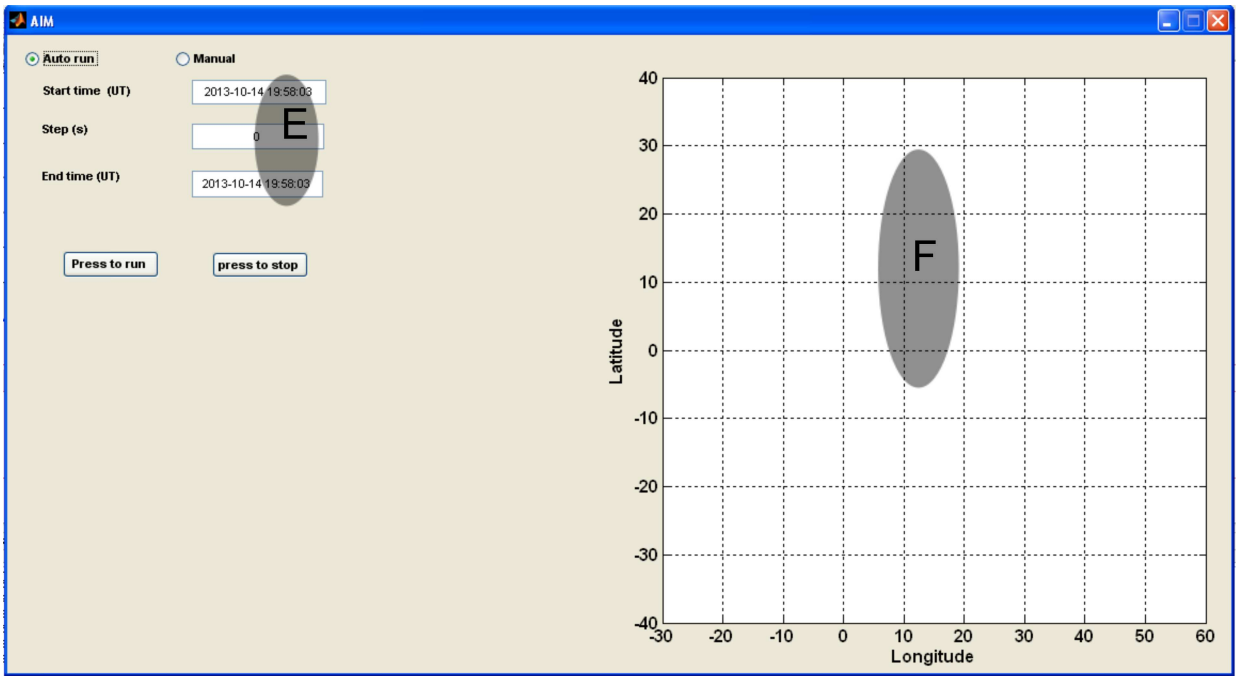

Figure 7.3: Automatic mode interface of AIM.

7.3 The Automatic Mode Interface

This mode is activated by selecting the "Auto run" radio button, thus changing from the manual interface to automatic interface (see figure 7.3). This option was added to the AIM at the request of the SANSA Space Weather Centre which requires a continuous prediction of ionospheric values.

When the program is in the automatic mode, the user specifies the start time (UT), step size (s) and end time (UT) for which the map is to run, otherwise the current computer time is set as the default (see section E of figure 7.3). When generating foF2 maps, it is recommended that multiples of 15 minutes (900s) are used as a step size for the sake of accuracy. The ionosonde data used in the map has a temporal resolution

of 15 minutes and therefore it is recommended that the resolution is set to the resolution of the most accurate data source available.

The "Press run" button activates the program and the output (a geographical variation of the chosen parameter) is plotted in section F in intervals of the step size. To deactivate the automatic process, use the "Press to stop" button.

7.4 Operation of AIM

The operation or procedure followed by the AIM program depends on the parameter chosen (see section B of the interface) and whether the program is running online (able to access and download the required data) or offline (with no access to the required data). This section briefly explains the procedure followed.

7.4.1 foF1, foE and foD

The accuracy of these three parameters was not discussed in detail, because their application in radio communication is minimal. Should the user choose any of these parameters as the output, the program uses the IRI-2012 model standard output without any adjustments.

7.4.2 foF2

When this parameter is chosen, the program goes on-line, tries to access and download ionosonde and GPS data from the SANSA and the AFREF server links. If download is successful, the program calculates the time difference between the downloaded data and the input time (section A of the interface). If the difference is less than two hours,

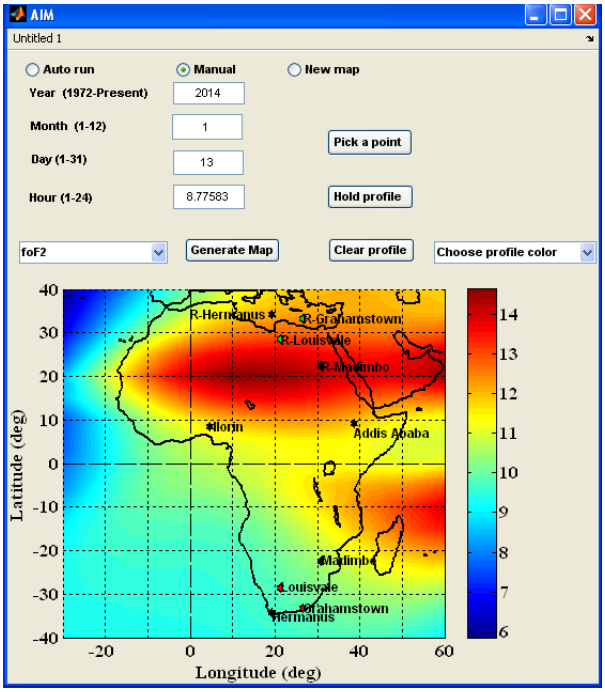

Figure 7.4: AIM foF2 map generated using IRI-2012 model, SABIM and ionosondes

the program follows the procedure for ionosonde data, as discussed in chapter 4. Otherwise, the data is not used and the program continues to work as if it were offline. Figure 7.4 shows an example of a generated AIM foF2 map using all the data sources. The red stars indicate the active original ionosondes, the green stars indicate the reflected ionosondes and the black stars indicate non-active or non-accessible ionosondes.

7.4.2.1 Profile Generation

When the user chooses to generate a profile for any geographic location on the map, the program sources the coordinates of the chosen location. Depending on the locus of the chosen point, the following procedure is followed:

- If in the south (below the $-\ 20^o$ geographic latitude), the program uses the generated result from the ionosondes and the two models IRI-2012 and SABIM (as explained in chapter 3) to obtain the foF2 value.

- If located within the equatorial region ($\pm\ 20^o$ geographic latitudes), the program checks within a radius of 10 ^{o} for any available GPS station data. If data is available, the program uses the TEC2F2 model to generate the foF2 value, otherwise the program uses the IRI-2012 model value. The TEC2F2 model in this case is a function of TEC, time (t), longitude ($long$) and latitude (lat), as illustrated in equation 7.1.

$$\text{foF2} = \text{TEC2F2}(TEC, t, long, lat) \tag{7.1}$$

- If located in the north above the equatorial anomaly boundary (above $+\ 20^o$ geographic latitude), the program uses the foF2 values obtained using the reflected ionosondes and the IRI-2012, as discussed in chapter 4.

To generate the profile, the program passes three variables, namely latitude, longitude and the obtained foF2 value, as inputs to the IRI-2012 model, which then adjusts its algorithm to give the required output. An example of an foF2 map and profiles generated for, 20:00 UT DOY 9 of 2012 is shown in figure 7.5. The profiles are of different locations on the map with the intersection of the cross-wire indicating the location of the last selected point. The title above the profile axes indicates the time and location of the last profile generated.

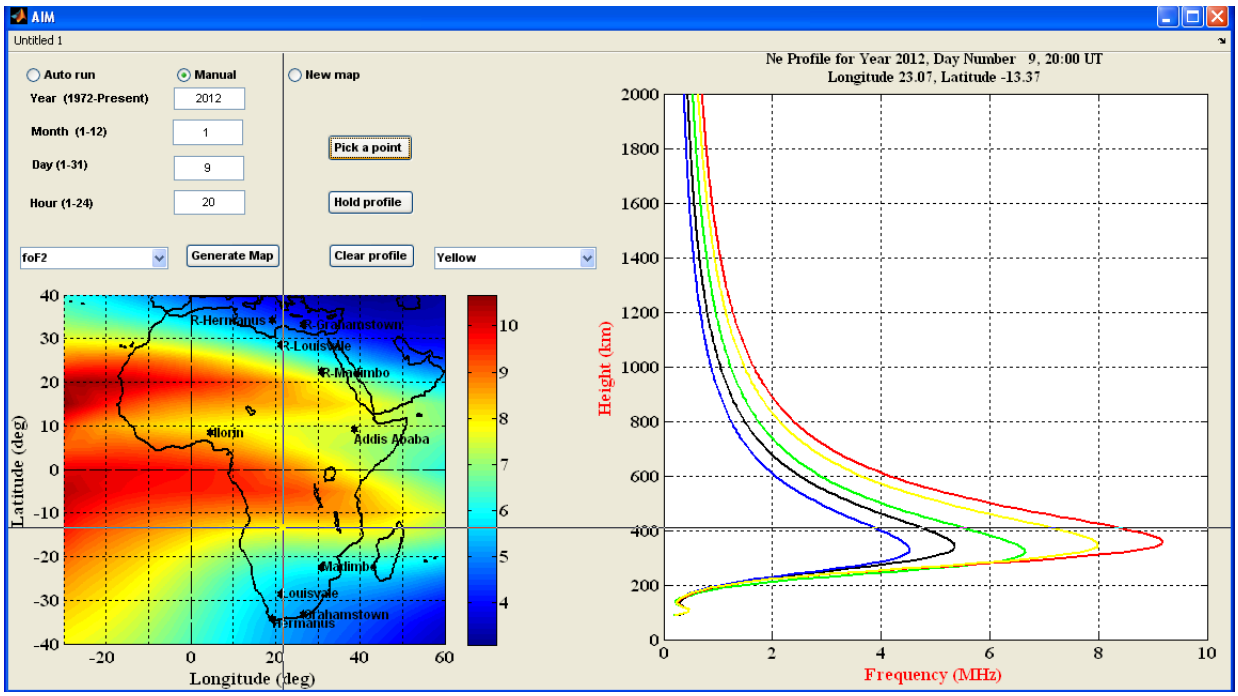

Figure 7.5: An example of an foF2 map and profiles generated for , 20:00 DOY 9 of 2012.

Offline: When the AIM is running offline, the SABIM model is used in the quadrilateral region bounded by original ionosondes (see chapter 4) and the IRI-2012 model elsewhere on the map to generate the required foF2 map.

7.4.3 TEC map

To generate a TEC map, the program attempts to access and download online GPS data. If the data for the specified time is available, the following steps are taken to calibrate the IRI-2012 model before it is used:

1. The GPS data are used to obtain the TEC (hereafter referred to as GPS-TEC) values of the geographic locations of the GPS receiver stations.

2. The locations (longitude and latitude) of two or three GPS receivers (with successful GPS-TEC processing) within in 10^o proximity of the locus are fed to the IRI-2012 model to generate TEC values (hereafter referred to as IRI-TEC) for those loci.

3. The IRI indices, Rz12 and IG12, used for generating the IRI-TEC values, are obtained.

4. The difference between the GPS-TEC and IRI-TEC at one of the selected GPS stations is determined.

5. If the difference is more than 3 TECU in magnitude the program continues to solve for new values of Rz12 and IG12, otherwise no further steps are taken.

6. Solving for the new indices depends on whether the difference is negative or positive. For a negative difference the indices are increased while for a positive difference they are decreased, as shown in equation 7.2.

$$\text{IRI-TEC} = IRI((\text{Rz12} \pm \gamma), (\text{IG12} \pm \xi)),\ \gamma = 0.1,\ \xi = 0.1 \quad (7.2)$$

7. For each iteration the new R12 and IG12 values are put back into the IRI-2012 model to generate a new IRI-TEC value. This value is compared to the GPS-TEC value and the above procedure from step 6 is repeated until the difference in magnitude is less than or equal to 3 TECU.

8. The above process from step 3 is repeated for all the selected GPS stations and the resulting R12 and IG12 averaged and considered as inputs to the IRI-2012 model.

9. The new calibrated IRI-2012 model is then used to generate the TEC map.

Figures 7.6a and 7.6b show examples of TEC maps that were generated at the same time of year using non-calibrated and calibrated IRI-2012 models respectively. In the non-calibrated case, the IRI-2012 shows an overestimation of the TEC values especially over the equatorial region with TEC values above 70 TECU. A great improvement is observed after calibration with more realistic TEC values ranging between 40 and 50 TECU. This improvement is very evident in figure 7.7 where

Table 7.1: RMSE and R2 values obtained using calibrated and non calibrated IRI-2012 models at different GPS stations in the African sector

Station code	Country	Geographic location	Calibrated IRI-2012		Non calibrated IRI-2012	
			RMSE (TECU)	R2	RMSE (TECU)	R2
ADIS	Ethiopia	9.3^o N, 38.7^o E	0.805	0.998	6.340	0.863
BKFP	Nigeria	12.5 ^{o} N, 4.2^o E	6.380	0.808	8.698	0.644
MFKG	South Africa	25.8^o S, 25.5^o E	5.099	0.730	6.449	0.568
MONG	Zambia	15.3^o S, 23.1^o E	3.726	0.916	7.803	0.631
MTND	Mozambique	16.1^o S, 33.6 ^{o} E	5.345	0.796	5.099	0.730
ZAMB	Zambia	15.2^o S, 28.2 ^{o} E	4.785	0.853	7.769	0.613
Average			4.356	0.850	7.026	0.675

the calibrated and non-calibrated IRI-2012 models have been used to generate diurnal TEC values at different GPS stations (listed in table 7.1) within the African sector, and the result compared to the derived TEC (1 hour resolution) from the GPS data at those locations. The calibrated IRI-2012 model was better at estimating the TEC values with an average RMSE = 4.4 TECU and R2 = 0.85, than the non-calibrated IRI-2012 model with RMSE = 7 TECU and R2 = 0.7.

Offline: The program uses only the IRI-2012 model to generate the required TEC map without any calibration.

7.4.4 M3000F2

When this parameter is selected, the program draws the map of Africa and waits for the user to choose any point (or location) on the map. Once a point is chosen, the program uses the latitude and longitude of the chosen point as inputs and attempts to download the ionosonde or GPS data within a 10^o radius of the chosen location. If the ionosonde data is available, it is given first priority, otherwise the

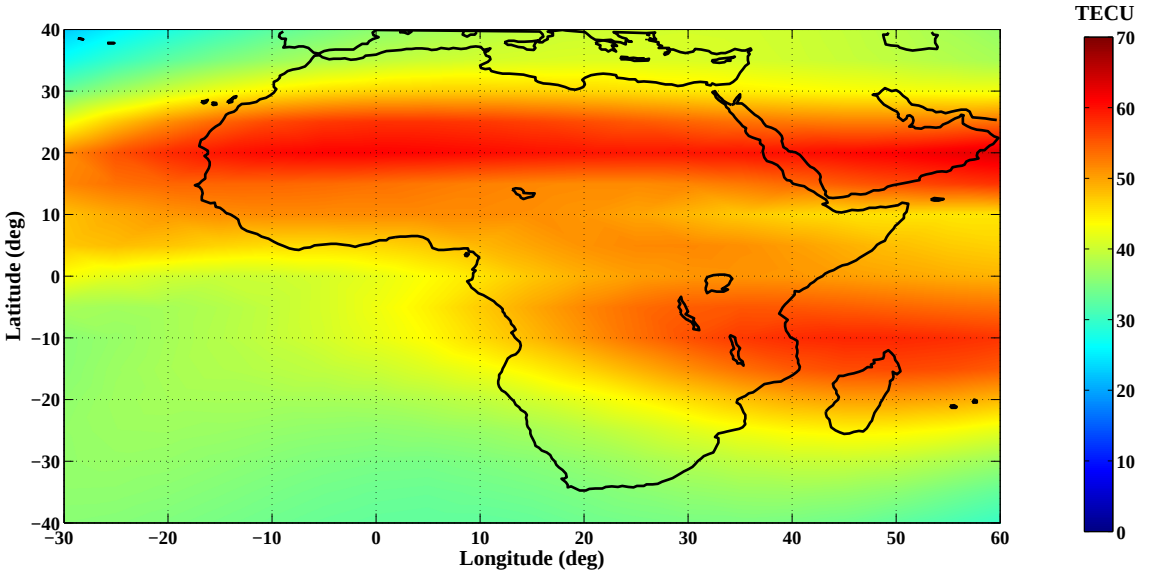

(a)

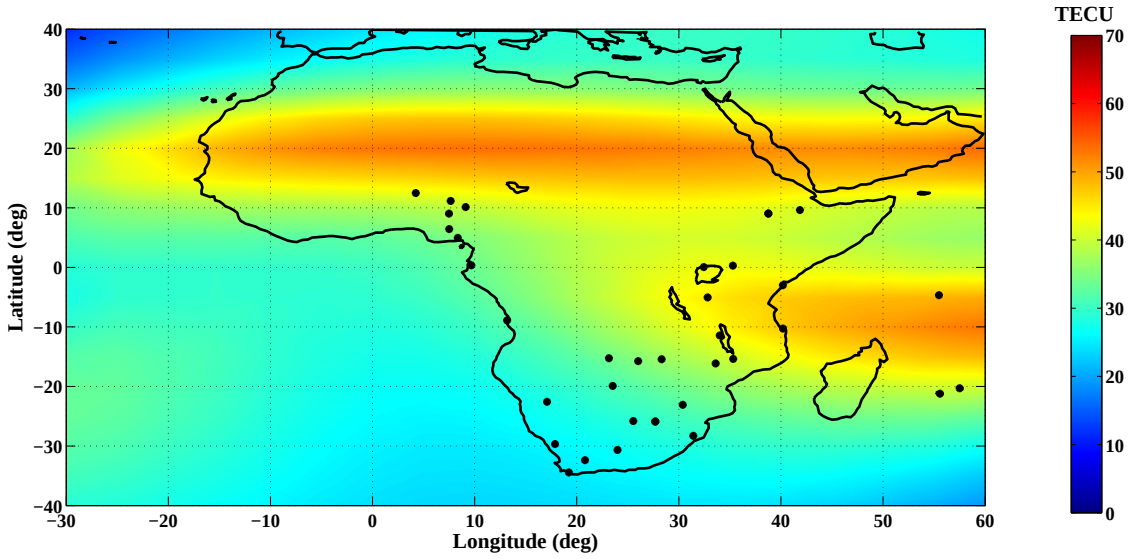

(b)

Figure 7.6: TEC maps generated by using (a) non-calibrated and (b) calibrated IRI-2012 models on DOY 1 in 2013.

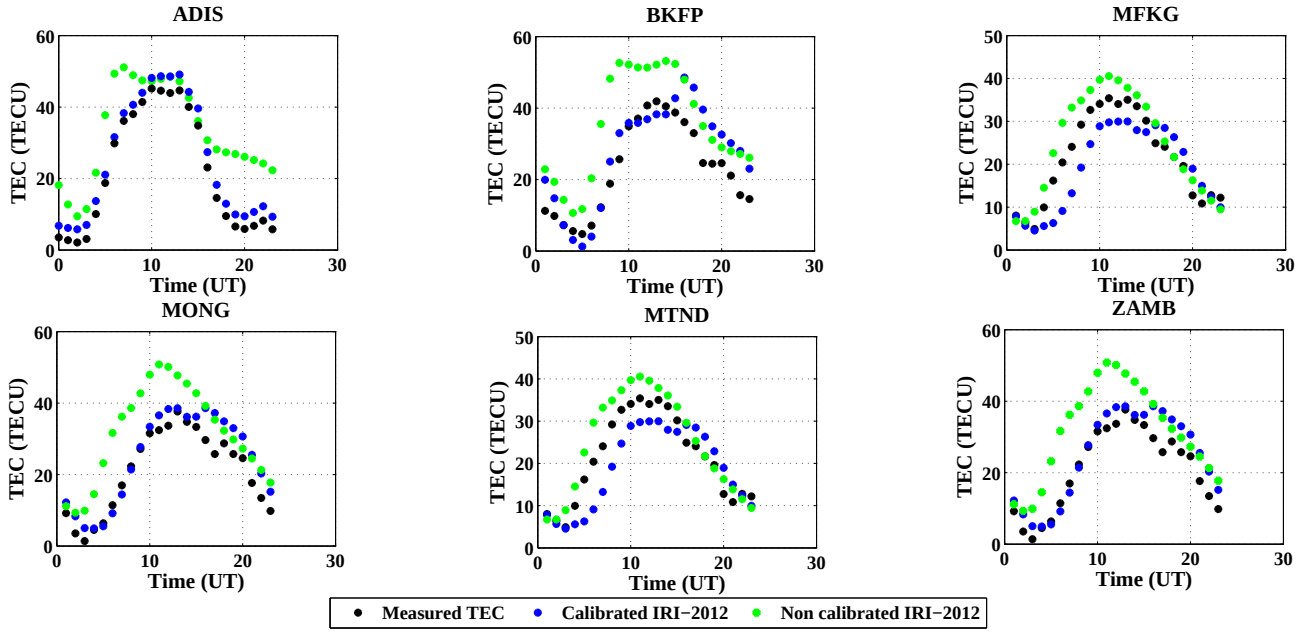

Figure 7.7: A plot of diurnal derived TEC values and results from calibrated and non-calibrated IRI-2012 models at GPS stations (MONG, MTND, ZAMB and MFKG) within the African sector on DOY 1 of 2013.

GPS data is used and the TEC2F2 model (see equation 7.1) is used to generate the foF2 value at that location. The obtained foF2 value, latitude, longitude and time are then passed to the IRI-2012 model as inputs. As an output, the program draws out a circular area on the map using the input longitude and latitude as the centre point. This area is 3000 km in radius measured along the great circle, assuming the Earth is a sphere and having a mean radius of 6371 km. In addition, the program displays in table format the calculated M3000F2 and the parameters used for the calculation, foF2 and hmF2. An example of an M3000F2 map is shown in figure 7.8.

In figure 7.9 diurnal M3000F2 values from AIM (on DOY 64 of 2010) are compared to ionosonde measurements from stations Hermanus, Grahamstown and Madimbo. The average RMSE was found to be 0.09.

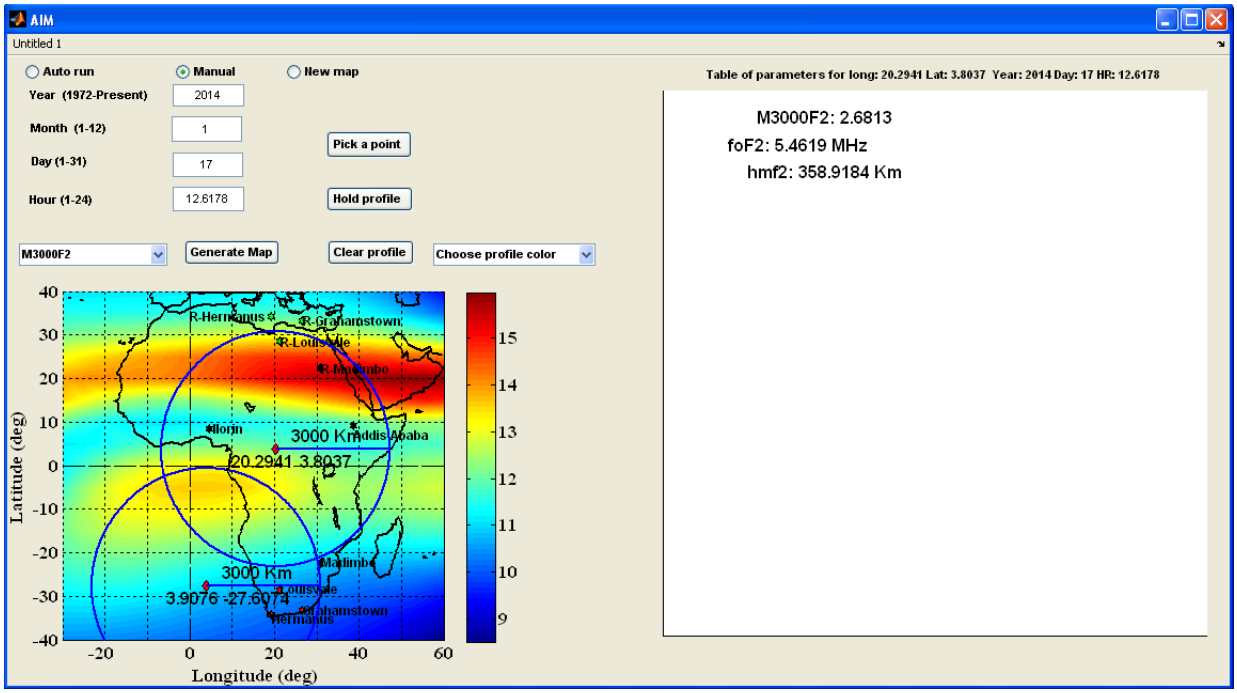

Figure 7.8: An example of an M3000F2 map.

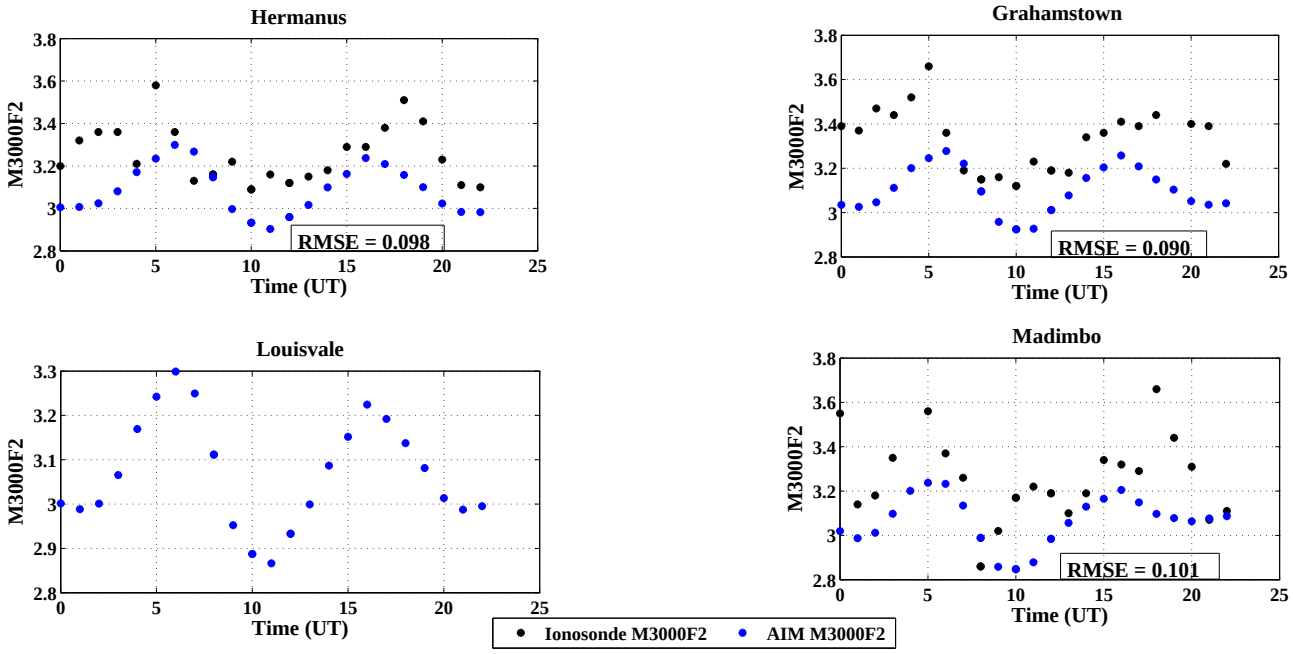

Figure 7.9: A comparison of diurnal M3000F2 values from AIM with ionosonde measurements from Hermanus, Grahamstown, Louisvale and Madimbo.

offline: When the map is running offline, the program uses a combination of SABIM and IRI-2012 model values to generate the required map.

7.5 Summary

This chapter discussed the operation of AIM and its interface. The procedure towards the final output of each parameter was briefly discussed. (See figure 7.10 for the AIM flow chart). The improvement in the estimation of the TEC values by means of the calibration of the IRI-2012 model using TEC values derived from GPS data, was shown. The next chapter focuses on the validation of results of AIM with the emphasis on the foF2 parameter.

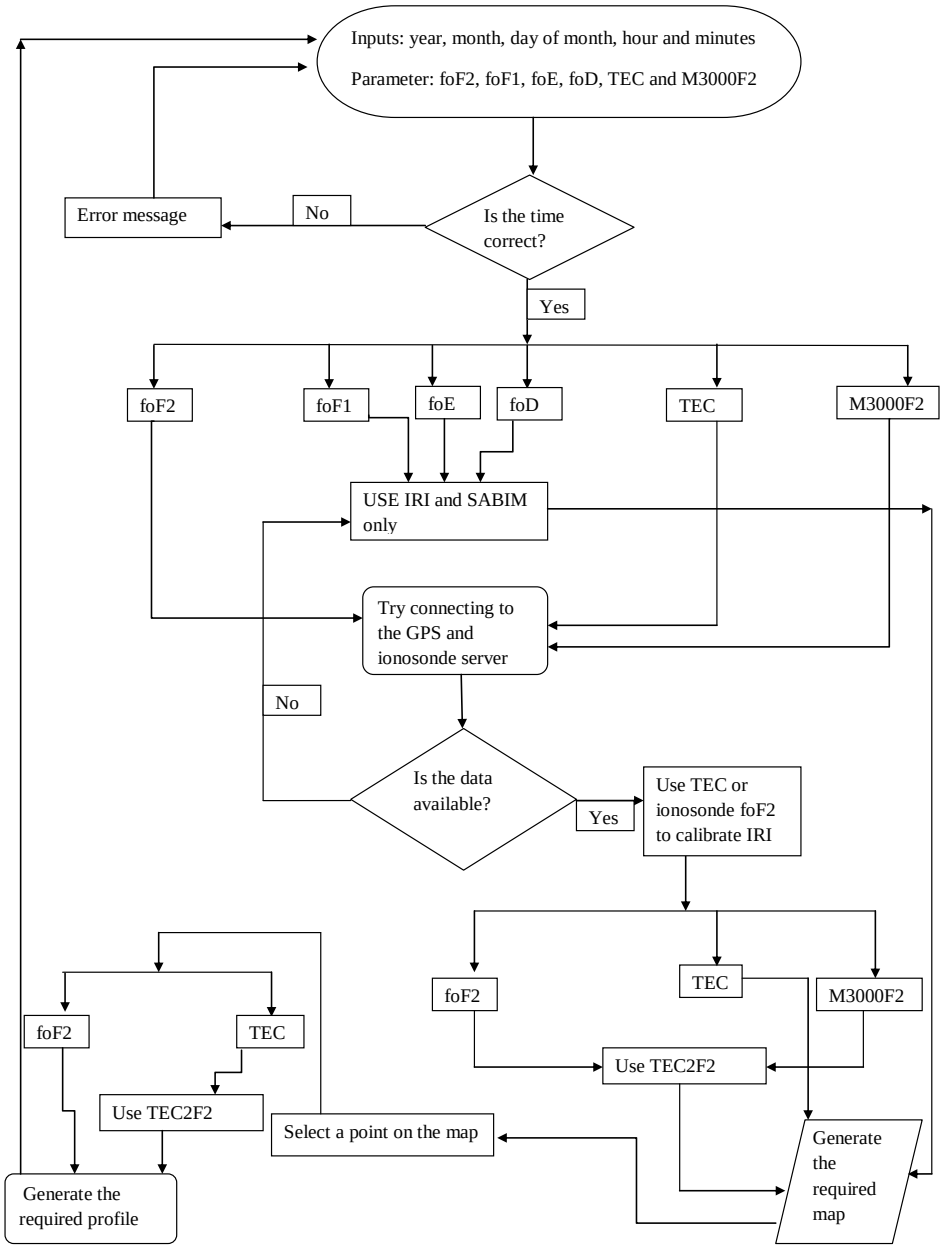

Figure 7.10: AIM's flow chart.

Chapter 8

AIM Validation

8.1 Introduction

This chapter validates the results of AIM with emphasis on the foF2 parameter. The results are comprehensively compared to the results of the initial attempt as presented in chapter 4 and to ionosonde measurements in order to point out the improvements. The analysis is carried out for various cases of diurnal, seasonal and solar activity. However, due to the paucity of ionospheric data over the African sector, the comparison to ionosonde measurements is limited to the South African ionosonde network.

8.2 Diurnal Validation

Figure 8.1 shows diurnal foF2 maps generated by AIM using a 2-hour resolution on DOY 64 of 2012. The IRI-2012 model was calibrated with ionosonde foF2 measurements from three stations; Hermanus, Graham-

stown and Louisvale. The maps show a general reduction in intensity compared to the initial diurnal results presented in chapter 4.

Figure 8.2 depicts the difference between the initial attempt and final AIM diurnal maps. The highest difference, above 2 MHz, is observed between 08:00 UT and 18:00 UT especially over the equatorial region. This is to be expected since the IRI model (without modification) which was initially used to model the equatorial region is known to overestimate the foF2 parameter in this particular region.

Furthermore, diurnal foF2 values at two ionosonde locations, Grahamstown and Hermanus, were sampled (at a 1-hour resolution) from the initial attempt and the final diurnal AIM maps and the results compared to the ionosonde measurements, as shown in figure 8.3. The combined use of error minimisation techniques (in the final AIM) produced an RMSE which is 66 % better (calculated using equation 8.1) than RMSE of the initial attempt results.

$$\% \text{ improvement} = \left(\frac{\text{Average (Intial attempt)} - \text{Average (final AIM)}}{\text{Average (Intial attempt)}} \times 100 \right) \tag{8.1}$$

8.3 Seasonal Validation

Figure 8.4 shows foF2 maps generated for different seasons of 2010 (on the same days of the year as those presented in chapter 4). The maps show the expected seasonal variation in foF2, however, the intensity

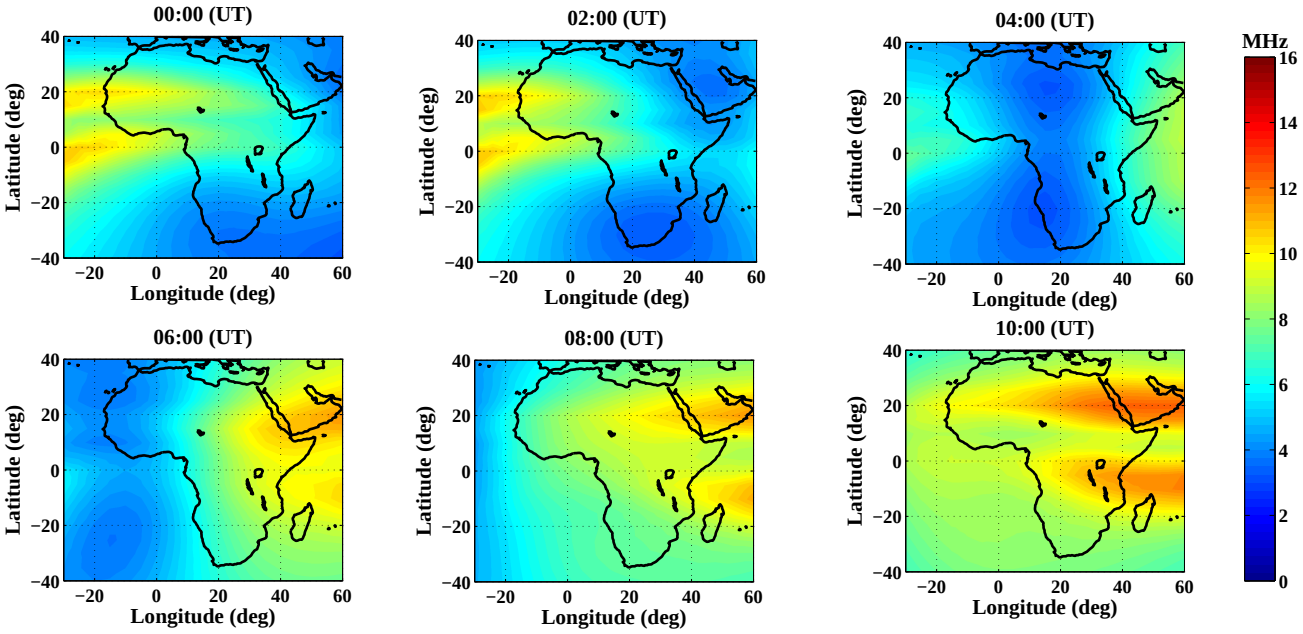

(a)

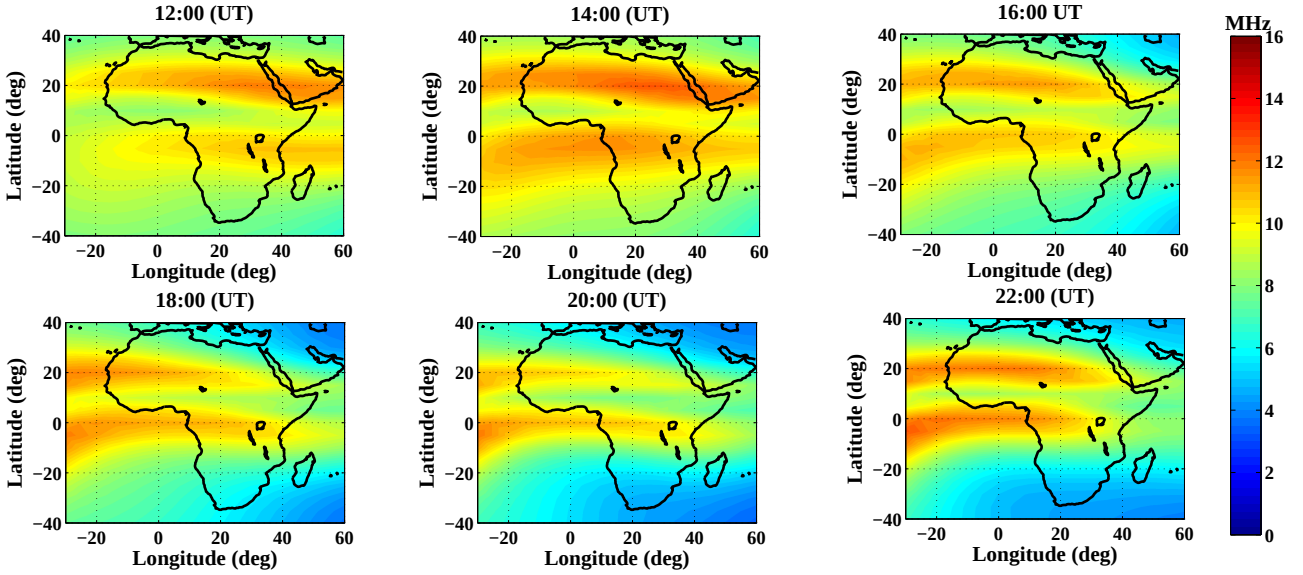

(b)

Figure 8.1: Diurnal foF2 maps generated by the final AIM using a 2-hour resolution on DOY 64 of 2012, for (a) 00:00 UT - 10:00 UT, and (b) 12:00 UT - 22:00 UT.

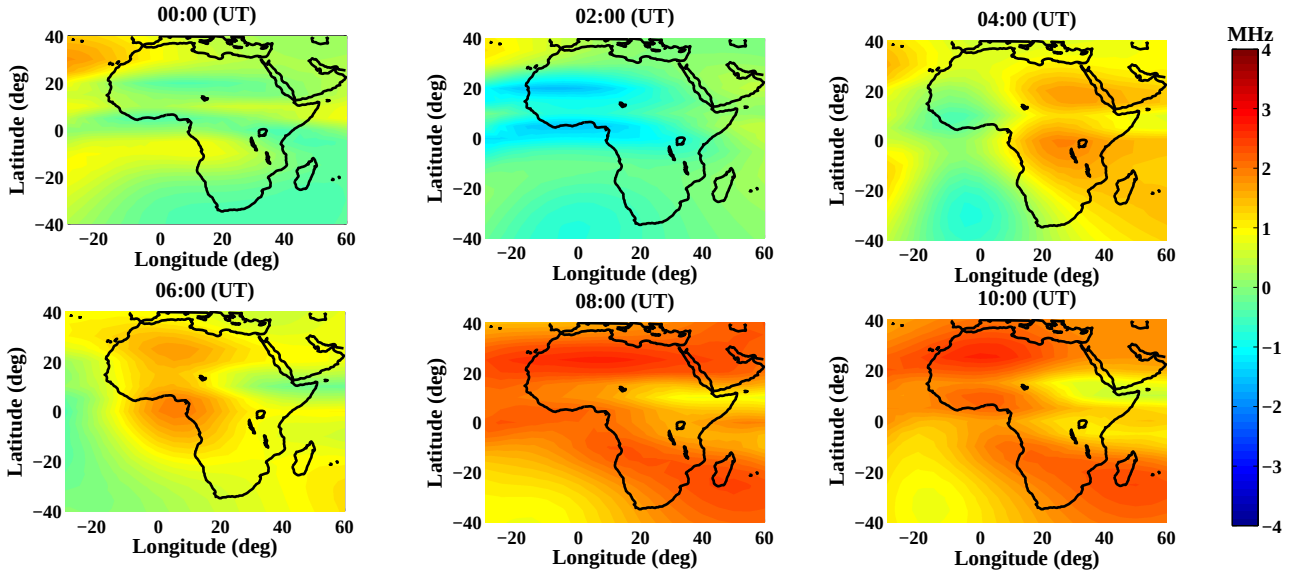

(a)

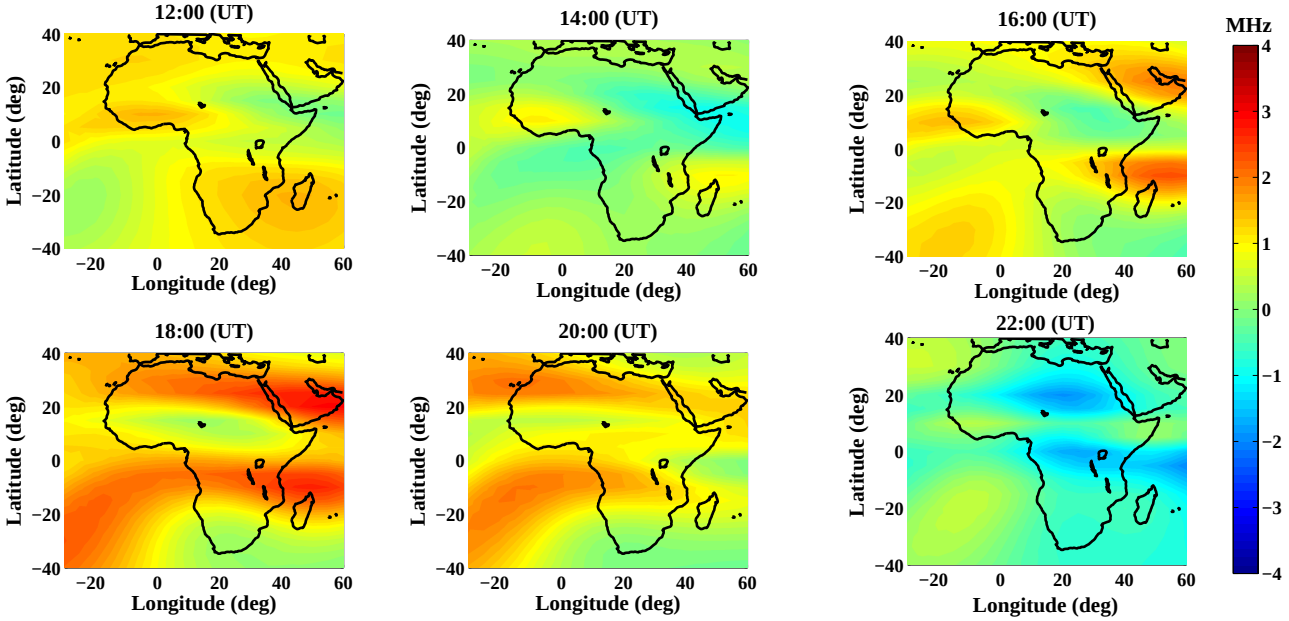

(b)

Figure 8.2: Difference between initial attempt and final AIM results, for (a) 00:00 UT - 10:00 UT, and (b) 12:00 UT - 22:00 UT.

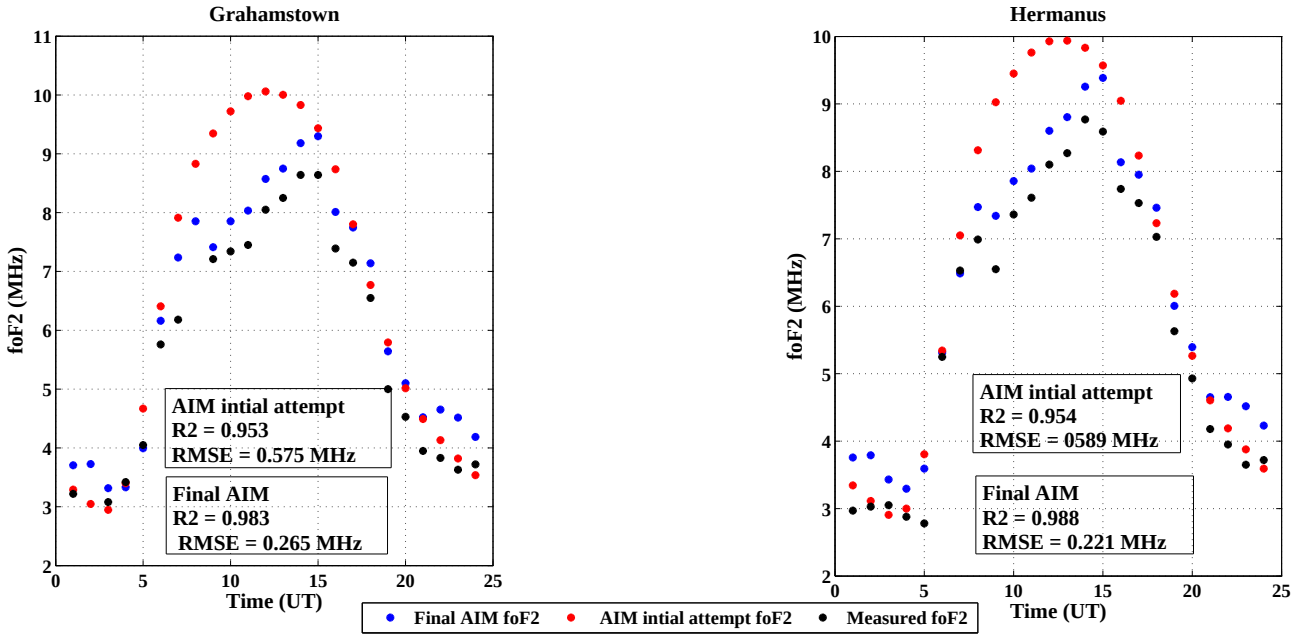

Figure 8.3: Diurnal foF2 values by the initial attempt and final AIM compared to ionosonde measurements from Grahamstown and Hermanus stations.

(mainly during summer and winter) is less than that of the results in chapter 4.

In figure 8.5, the 2010 10:00 UT foF2 values produced by the initial attempt and final AIM at four ionosonde locations, Hermanus, Grahamstown, Louisvale and Madimbo, are compared to the ionosonde measurements at those locations. The results by the final AIM compared to those of the initial attempt, show a better correlation with the measured foF2 values, particularly during the summer period and the equinoxes (in March and September) when the variability of foF2 is highest. This was confirmed by the calculated overall average of R2 = 0.8 for the final AIM compared to R2 = 0.5 for the initial attempt.

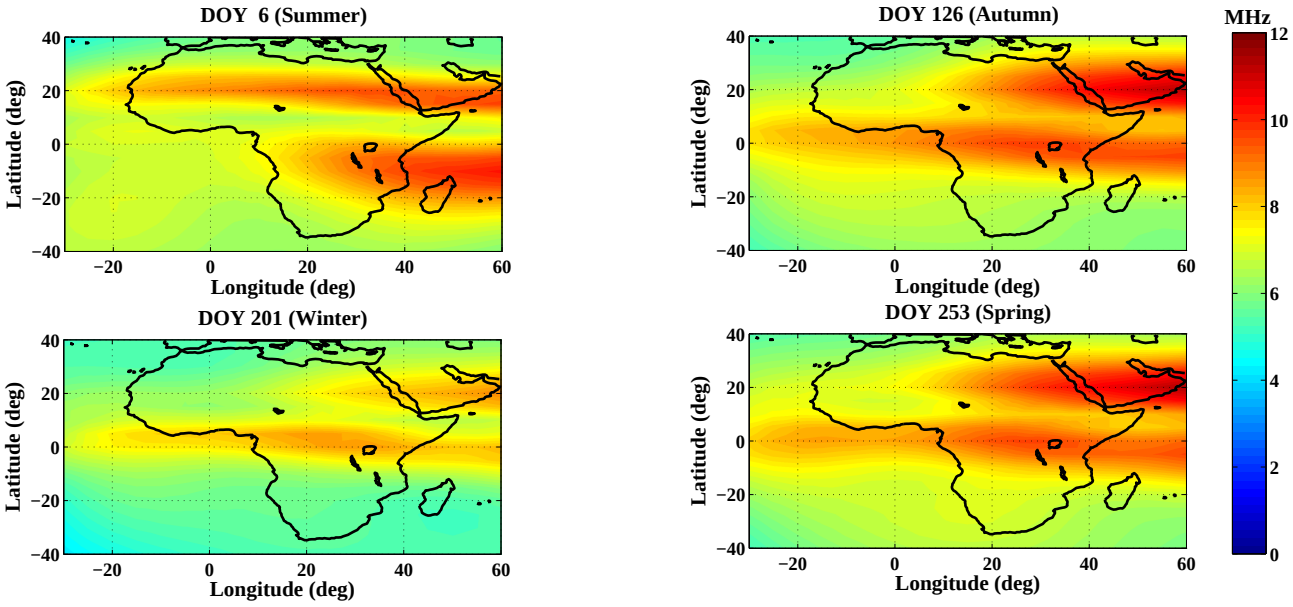

Figure 8.4: Seasonal variation of 10:00 UT foF2 values over the African region for 2010 by the final AIM.

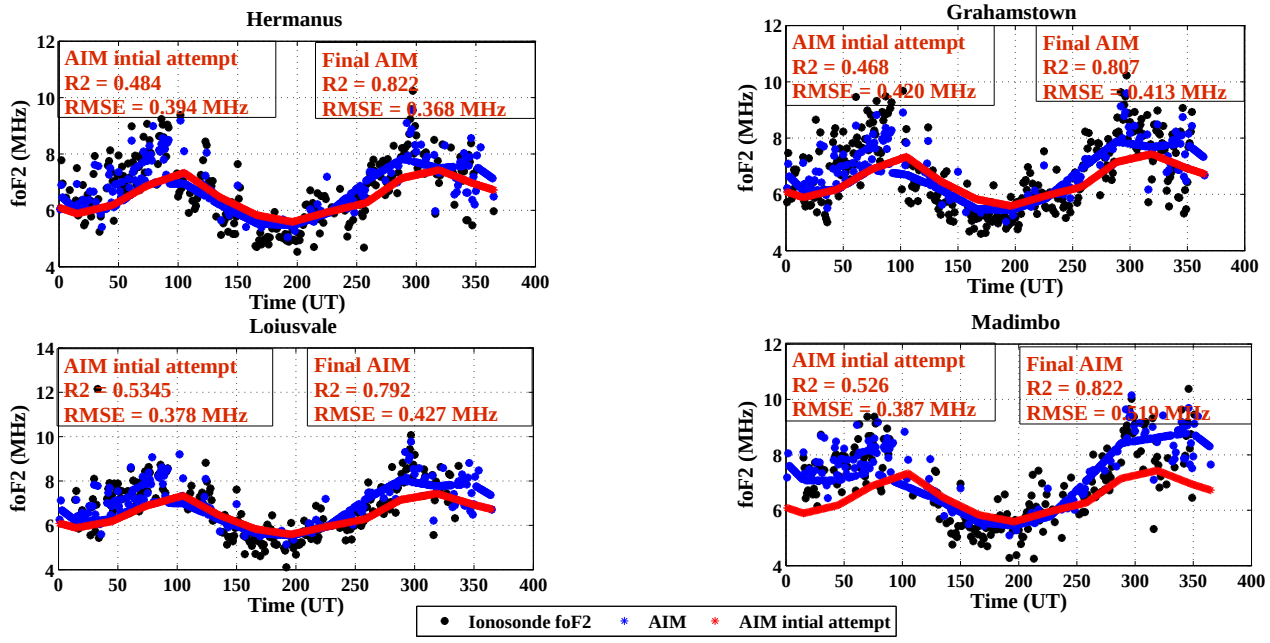

Figure 8.5: 10:00 UT foF2 values by AIM for 2010.

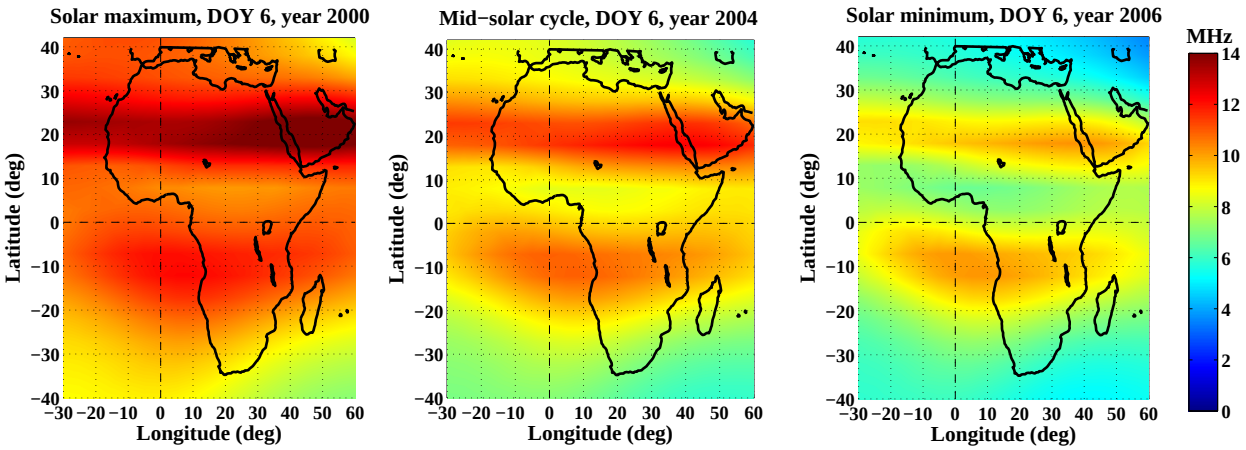

Figure 8.6: 10:00 UT foF2 maps generated by the final AIM during the different stages of the solar cycle on DOY 6, solar maximum (2000), mid-solar cycle (2004) and solar minimum (2006).

8.4 Solar Cycle Validation

Figure 8.6 shows foF2 maps generated for DOY 6 during solar maximum (2000), moderate solar cycle (2004) and solar minimum (2006). Compared to the initial results presented in chapter 4, the AIM program was better at estimating the foF2 parameter. This improvement is most defined in the equatorial region ($\pm$ 20° geographic latitude) during solar maximum. The map exhibits a well-defined equatorial anomaly region (due to the fountain effect) which is absent in the results of the initial attempt.

Furthermore, 10:00 UT foF2 values were obtained for both solar maximum and solar minimum periods from the initial attempt and the final AIM, and compared to the ionosonde foF2 measurements, as shown in figures 8.7a and 8.7b. The solar maximum comparison was done using

results from only one ionosonde station, Grahamstown, with sufficient data for analysis for the year 2000.

For solar maximum, the final AIM results are 50 % better (calculated using equation 8.1), both in the RMSE and R2 than the initial attempt results presented in chapter 4.

During solar minimum, when the two models (SABIM and IRI-2012) used in modelling the southern region perform best (refer to chapter 3), the increased error reduction (RMSE) was minimal (16 %). However, the correlation of the final AIM results with the ionosonde measurements improved by 75 % over the initial attempt result.

8.5 Summary

This chapter presented the validation of results by the final AIM program (using all the error minimisation techniques discussed in the previous chapters) with the emphasis on the foF2 parameter. The results were compared with the results of the initial attempt and with ionosonde measurements. The validation showed that the final AIM was better at estimating the foF2 parameter than the initial attempt, which relied largely on the IRI-2012 model. The next chapter offers concluding remarks and puts forward suggestions for future improvement of the AIM's accuracy.

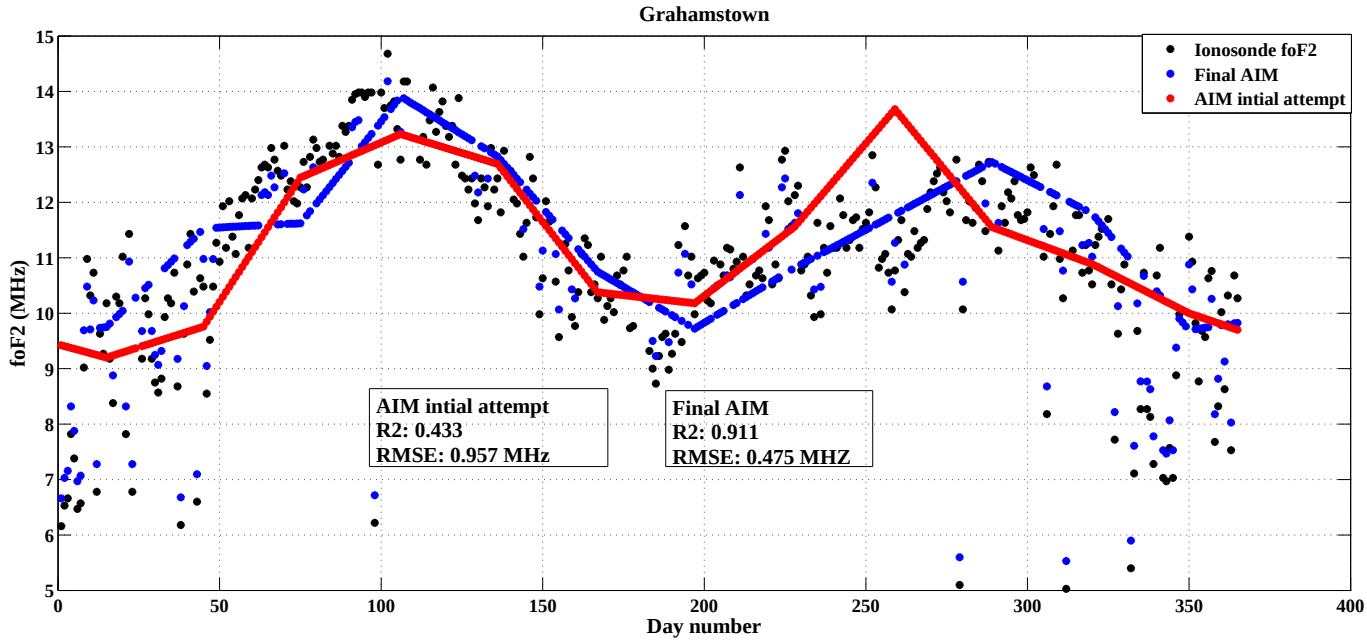

(a)

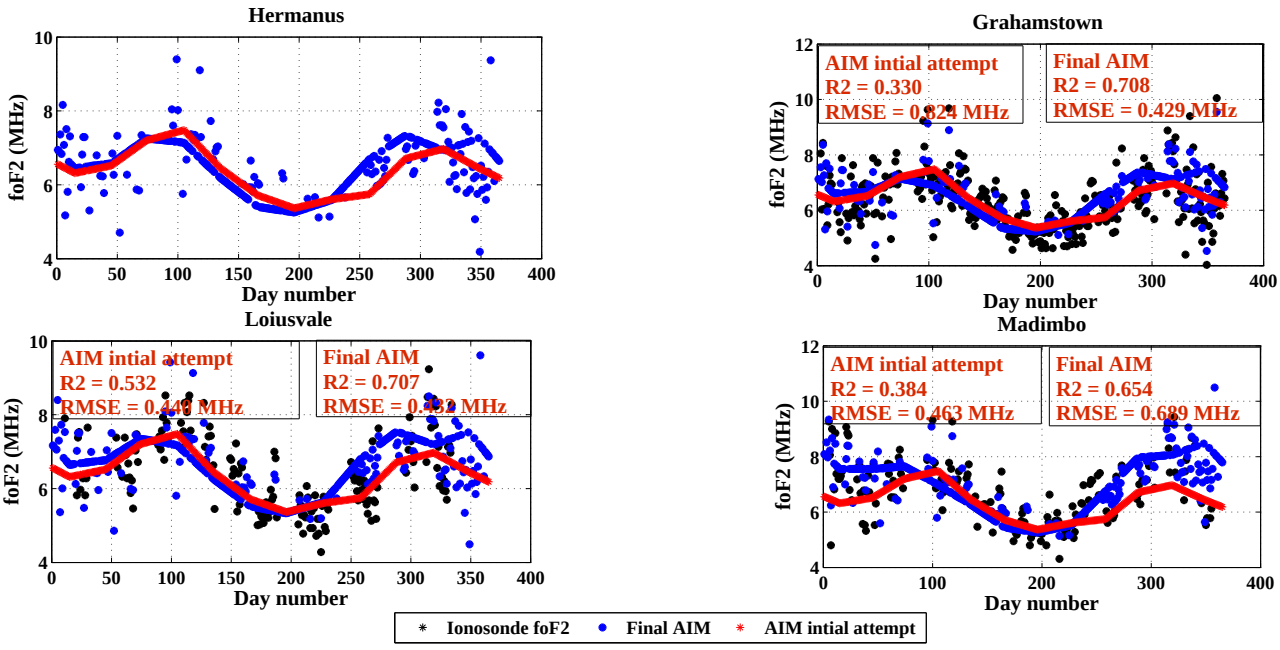

(b)

Figure 8.7: Variation of foF2 at 10:00 UT for (a) Grahamstown during solar maximum, and (b) all four ionosonde locations during solar minimum.

Chapter 9

Conclusion and Future work

This thesis set out to describe the development of the African Ionospheric Map (AIM) which makes use of the available ionospheric data sources for the African sector: African ionosonde network, IRI-2012, SABIM and satellite data. The AIM uses these data sources and error minimisation techniques to estimate ionospheric parameters values at any given location on the continent. The focus was on the accurate measurement of three parameters, namely foF2, TEC and M3000F2, which are important for radio communication. The analysis of the results showed that AIM gave a better estimation of the three parameters than the most recent internationally recognised and recommended ionosphere model (IRI-2012). Thus, the AIM is a more accurate solution than single independent data sources for applications requiring ionospheric mapping over the African continent.

Further, AIM was designed with a user-friendly interface and an output which is a graphical representation of the chosen parameter or a profile (frequency and height points).

In this study a new statistical method (TEC2F2) was developed to estimate foF2 from GPS-derived TEC. This is a pioneering method that allows for the utilisation of additional resources to close the gap in ionospheric mapping over Africa, particularly in an area like the equatorial region that is so dynamic yet under represented in ionospheric observation.

The main limitation of the AIM lies in obtaining accurate data (such as ionosonde measurements) when the program runs in real time. This is experienced mainly between 20 ^{o}S - 40 ^{o} N where there is a paucity of ionosonde data. In addition, the TEC2F2 model that is largely used in the equatorial region was designed using a dataset that only spanned the period from solar minimum 2006 to the approach of solar maximum 2012, thus not including the whole solar maximum. Therefore, the TEC2F2 is limited in its approximation of the foF2 parameter during solar maximum variations.

9.1 Future work

This section suggests improvements that could enhance the performance of the AIM in the future.

- Due to the paucity of ionospheric data over most regions in Africa, the validation process concentrated mainly on results from the South African region where most of the ionosondes on the continent are located. However, there is a need to validate AIM's performance over other African regions (especially the equatorial region)

once the ionosonde database expands to include more data from other regions of Africa.

- It was hoped that the application of AIM in ray tracing would be included in this thesis. Unfortunately, due to time constraints, this was not possible. Therefore, it is recommended that the AIM be tested for application in ray tracing and DF systems.

- Although the current map covers the most important ionospheric parameters in radio communication, there is a need to include more ionospheric parameters such as B0, B1, hmE, hmF1 and hmF2.

- Tsai and Tsai (2004) proposed an improvement on the classical approach of the Abel inversion that considers the effects of large-scale horizontal gradients and/or inhomogeneous ionospheric electron densities (N_e), by developing an iterative scheme to determine ‘‘compensated’’ total electron content (TEC) values through nearby radio occultation observations. Validation checks with independent ionospheric F2 layer peak N_e and height data from ionosonde systems show successful improvement and fundamental suitability of the iteration scheme for the inversion of compensated TEC values into N_e information (Tsai et al., 2009). This improvement in accuracy provides the possibility of using GPS radio occultation data in the AIM as a real-time input which will enhance the program's performance.

- Matlab was used as the programming language for AIM. However, licensing is expensive in terms of money and time. Furthermore, the standalone package delivered to the end-user needs additional

bulky libraries (Matlab Compiler Runtime (MCR)) for the accurate running of the program. Therefore, the AIM Matlab code needs to be replaced by a less expensive and more manageable language (for example, C++, Fortran or Java).

This thesis described the development of the AIM with the purpose of improving estimation of ionospheric observation values over the African continent. The AIM provides more accurate estimations than most international and regionally-based ionospheric models for the African region. In addition, the AIM is user-friendly, shows the temporal and spatial variation of the ionospheric parameters in real time as well historically, and details the expected ionospheric physics at any geographical location. Therefore, it is expected that the AIM will prove valuable to most communication industries and other sectors in dire need of accurate ionospheric observations over the African sector.

References

Adeniyi, J., Bilitza, D., Radicella, S., Willoughby, A., 2003. Equatorial F2-peak parameters in the IRI model. Advances in Space Research 31, 507–512.

Aragon-Angel, A., Hernandez Pajares, M., Juan, J., Sanz, J., 2009. Obtaining more accurate electron density profiles from bending angle with GPS occultation data: FORMOSAT-3/COSMIC constellation. Advances in Space Research 43, 1694–1701.

Bartels, J., 1957. General Remarks on Geomagnetic Observatories: Technique of Scaling Indices K and Q of Geomagnetic Activity. Pergamon Press, Oxford.

Bartels, J., Heck, N., Johnston, H., 1939. The three-hour-range index measuring geomagnetic activity. Terrestrial Magnetism and Atmospheric Electricity 44, 411–454.

Bilitza, D., 1986. International reference ionosphere: Recent developments. Radio Science 21, 343–346.

Bilitza, D., McKinnell, L.-A., Reinisch, B., Fuller-Rowell, T., 2011. The international reference ionosphere today and in the future. Journal of Geodesy 85, 909–920.

Bilitza, D., Obrou, O., Adeniyi, J., Oladipo, O., 2004. Variability of foF2 in the equatorial ionosphere. Advances in Space Research 34, 1901–1906.

Bilitza, D., Reinisch, B., 2008. International reference ionosphere 2007: Improvements and new parameters. Advances in Space Research 42, 599–609.

Born, M., Wolf, E., 1986. Principles of Optics. Pergamon Press, Oxford.

Bradley, P., Dudeney, J., 1973. A simple model of the vertical distribution of electron concentration in the ionosphere. Journal of Atmospheric and Solar-Terrestrial Physics 35, 2131–2146.

Burrell, A. G., Bonito, N. A., Carrano, C. S., 2009. Total electron content processing from GPS observations to facilitate ionospheric modeling. GPS Solutions 13, 83–95.

Carrano, C., Groves, K., 2009. Ionospheric Data Processing and Analysis. Workshop on Satellite Navigation Science and Technology for Africa, 23 March - 09 April. The Abdus Salam ICTP, Trieste.

CCIR, 1966. Atlas of ionospheric characteristics. Report 340-1, 340-6. Comité Consultatif International des Radiocommunications, Genève.

Cheng, Chio-Zong, F., Ying-Hwa, K., Anthes, R. A., Lance, W., 2006. Satellite constellation monitors global and space weather. EOS, Transactions American Geophysical Union 87, 166–166.

Ciraolo, L., Spalla, P., 1997. Comparison of ionospheric total electron content from the Navy Navigation Satellite System and the GPS. Radio Science 32, 1071–1080.

Coco, D. S., Coker, C., Dahlke, S. R., Clynch, J. R., 1991. Variability of GPS satellite differential group delay biases. IEEE Transactions on Aerospace and Electronic Systems 27, 931–938.

Corduneanu, C., 2008. Integral Equations and Applications. Cambridge University Press, Cambridge.

Davies, K., 1990. Ionospheric Radio. Peter Peregrinus, London.

Davies, K., Hartmann, G., 1997. Studying the ionosphere with the Global Positioning System. Radio Science 32, 1695–1703.

Doherty, P., Coster, Anthea, J., Murtagh, W., 2004. Space weather effects of October-November 2003. GPS Solutions 8, 267–271.

Eberly, D., 2000. Least squares fitting of data. Magic Software, Chapel Hill, NC.

García, Fernández, M., 2004. Contributions to the 3D ionospheric sounding with GPS data. Ph.D. thesis, Universitat Politècnica de Catalunya, Barcelona.

Guochang, X., 2003. GPS: Theory, Algorithms and Applications. Springer-Verlag, Berlin.

Habarulema, J. B., McKinnell, L.-A., Buresová, D., Zhang, Y., Seemala, G., Ngwira, C., Chum, J., Opperman, B., 2013. A comparative study of TEC response for the African equatorial and

mid-latitudes during storm conditions. Journal of Atmospheric and Solar-Terrestrial Physics 102, 105–114.

Hajj, G. A., Romans, L. J., 1998. Ionospheric electron density profiles obtained with the Global Positioning System: Results from the GPS/MET experiment. Radio Science 33, 175–190.

Hofmann-Wellenhof, B., Lichtenegger, H., Collins, J., 1994. Global Positioning System: Theory and practice. Springer-Verlag, Berlin.

Hofmann Wellenhof, B., Lichtenegger, H., Wasle, E., 2007. GNSS-Global Navigation Satellite Systems: GPS, GLONASS, Galileo, and more. Springer, Vienna.

Houminer, Z., Soicher, H., 1996. Improved short-term predictions of foF2 using GPS time delay measurements. Radio Science 31, 1099–1108.

Hunsucker, Robert, D., Hargreaves, John, K., 2002. The high-latitude ionosphere and its effects on radio propagation. Cambridge University Press, Cambridge.

Jakowski, N., Tsybulya, K., 2005. Comparison of ionospheric radio occultation CHAMP data with IRI -2001. Advances in Radio Science 2, 275–279.

Kelley, M., 2009. The Earth's Ionosphere: Plasma Physics and Electrodynamics, 2nd Edition. Academic Press, New York.

Kouris, S. S., Xenos, T. D., Polimeris, K. V., Stergiou, D., 2004. TEC and foF2 variations: preliminary results. Annals of Geophysics 47, 1325–1332.

Kuo, Y.-H., Sokolovskiy, S., Anthes, R., Vandenberghe, F., 2001. Assimilation of GPS radio occultation data for numerical weather prediction. Terrestrial, Atmospheric and Oceanic Science 11, 157–186.

Kursinski, E. R., Hajj, G. A., Leroy, S. S., Herman, B., 2000. The GPS radio occulation technique. Terrestrial, Atmospheric, and Oceanic Sciences 11, 53–114.

Lei, J., Syndergaard, S., Burns, A. G., Solomon, S. C., Wang, W., Zeng, Z., Roble, R. G., Wu, Q., Kuo, Y.-H., Holt, J. M., 2007. Comparison of COSMIC ionospheric measurements with ground-based observations and model predictions: Preliminary results. Journal of Geophysical Research 112, A07308.

Lühr, H., Xiong, C., 2010. IRI-2007 model overestimates electron density during the 23/24 solar minimum. Geophysical Research Letters 37, L23101.

Lin, C., Liu, J., Tsai, H., Chen, M., 2001. Ionospheric Total Electron Content Response to Geomagnetic Storms in the West-Pacific Equatorial Anomaly Region. AGU Spring Meeting, 29 May - 02 June 2001, Boston, Massachusetts. Abstracts 1, SA31A–11.

Liu, R., Smith, PA and King, J., 1983. A new solar index which leads to improved foF2 predictions using the CCIR atlas. Telecommunication Journal 50, 408–414.

McKinnell, L.-A., 2003. A neural network-based ionospheric model for the bottomside electron density profile over Grahamstown, South Africa. Ph.D. thesis, Rhodes University, Grahamstown.

McKinnell, L.-A., 2008a. An Electron Density Profile Model for the South African Ionosphere. Proceedings of the XXIXth URSI General Assembly, Chicago, 7-16 August 2008, 33–34.

McKinnell, L.-A., 2008b. The Progress of the South African Ionosonde Network. AIP Conference Proceedings 974, 47–51.

McKinnell, L.-A., Poole, A. W., 2004. Neural network-based ionospheric modelling over the South African region. South African Journal of Science 100, 519–523.

McNamara, L., 1991. The Ionosphere: Communications, Surveillance, and Direction Fnding. Krieger, Malabar, FL.

McNamara, L., Retterer, J., Baker, C., Bishop, G., Cooke, D., Roth, C., Welsh, J., 2010. Longitudinal structure in the CHAMP electron densities and their implications for global ionospheric modeling. Radio Science 45, RS2001.

Okoh, D., McKinnell, L.-A., Cilliers, P., 2010. Developing an ionospheric map for South Africa. Annals of Geophysics 28, 1431–1439.

Okoh, Daniel, I., 2009. Developing an ionospheric map for South Africa. Master's thesis, Rhodes University, Grahamstown.

Ouattara, F., 2013. IRI-2007 fof2 Predictions at Ouagadougou Station during Quiet Time Periods from 1985 to 1995. Archives of Physics Research 4, 12–18.

Perrone, L., De Franceschi, G., 1998. Solar, ionospheric and geomagnetic indices. Annals of Geophysics 41, 5–6.

Phinney, R., Anderson, D., 1968. On the radio occultation method for studying planetary atmospheres. Journal of Geophysical Research 73, 1819–1827.

Prölss, G., 2004. Physics of the Earth's Space Environment: An Introduction. Springer-Verlag, Berlin.

Pulinets, S., Boyarchuk, K., 2004. Ionospheric Precursors of Earthquakes. Springer-Verlag, Berlin.

Rangarajan, G., Barreto, L., 2012. Secular change in the location of the magnetic dip equator in the twentieth century. Geofísica Internacional 39, 323–336.

Ratcliffe, J., 1972. An Introduction to the Ionosphere and Magnetosphere. Cambridge University Press, Cambridge.

Reinisch, B. W., 1986. New techniques in ground-based ionospheric sounding and studies. Radio Science 21, 331–341.

Reinisch, B. W., 2009. Digisonde 4D system manual. University of Massachusetts Lowell Center for Atmospheric Research, Lowell, MA.

Reinisch, Bodo, W., Galkin, I. A., Khmyrov, G., March 2012. Ionosonde Data Exchange SAO.XML Data Model 5.0. University of Massachusetts Lowell Center for Atmospheric Research, Lowell, MA.

Rishbeth, H., Sedgemore-Schulthess, K., Ulich, T., 2000. Semi-annual and annual variations in the height of the ionospheric F2-peak. Annals of Geophysics 18, 285–299.

Rush, C., Fox, M., Bilitza, D., Davies, K., McNamara, L., Stewart, F., PoKempner, M., 1989. Ionospheric mapping - An update of foF2 coefficients. Telecommunication Journal 56, 179–189.

Sardón, E., Zarraoa, N., 1997. Estimation of total electron content using GPS data: How stable are the differential satellite and receiver instrumental biases ? Radio Science 32, 1899–1910.

Schreiner, W. S., Sokolovskiy, S. V., Rocken, C., Hunt, D. C., 1999. Analysis and validation of GPS/MET radio occultation data in the ionosphere. Radio Science 34, 949–966.

Schunk, R., Nagy, A., 2009. Ionospheres: Physics, Plasma Physics, and Chemistry, 2nd Edition. Cambridge University Press, Cambridge.

Seeber, G., 2003. Satellite Geodesy. Walter de Gruyter, Berlin.

Seemala, G. K., Valladares, C. E., 2011. Statistics of total electron content depletions observed over the South American continent for the year 2008. Radio Science 46, RS5019.

Sibanda, P., 2010. Challenges in topside ionospheric modelling over South Africa. Ph.D. thesis, Rhodes University, Grahamstown.

Spalla, P., Cairolo, L., 1994. TEC and foF2 comparison. Annals of Geophysics 37, 929–938.

Ssessanga, N., McKinnell, L.-A., Habarulema, J., B., In-press. Estimation of foF2 from GPS TEC over the South African region. Journal of Atmospheric and Solar-Terrestrial Physics, Manuscript number: ATP3695.

Tsai, H. F., Liu, J. Y., Tsai, W. H., Liu, C. H., Tseng, C. L., Wu, C. C., 2001. Seasonal variations of the ionospheric total electron content in Asian equatorial anomaly regions. Journal of Geophysical Research 106, 30363–30369.

Tsai, L.-C., Liu, C. H., Hsiao, T. Y., Huang, J. Y., 2009. A near real-time phenomenological model of ionospheric electron density based on GPS radio occultation data. Radio Science 44, RS5002.

Tsai, L.-C., Tsai, W., 2004. Improvement of GPS/MET ionospheric profiling and validation using the Chung-Li ionosonde measurements and the IRI model. Terrestrial, Atmospheric and Oceanic Sciences 15, 589–607.

Wilson, B. D., Mannucci, A. J., 1993. Instrumental biases in ionospheric measurements derived from GPS data. Proceedings of the 6th International Technical Meeting of the Satellite Division of the Institute of Navigation (ION GPS 1993), 1343–1351.

Yue, X., Schreiner, W. S., Lei, J., Sokolovskiy, S. V., Rocken, C., Hunt, D. C., Kuo, Y.-H., 2010. Error analysis of Abel retrieved

electron density profiles from radio occultation measurements. Annals of Geophysics 28, 217–222.

Yue, X., Schreiner, W. S., Rocken, C., Kuo, Ying-Hwa, K., 2011. Evaluation of the orbit altitude electron density estimation and its effect on the Abel inversion from radio occultation measurements. Radio Science 46, RS1013.